



POLITECNICO
MILANO 1863

SCUOLA DI INGEGNERIA INDUSTRIALE
E DELL'INFORMAZIONE

Reduced Fluid-structure interaction and non-Newtonian models of blood flows for simulating the aortic valve

TESI DI LAUREA MAGISTRALE IN
MATHEMATICAL ENGINEERING - INGEGNERIA MATEMATICA

Author: **Luca Caivano**

Student ID: 944779

Advisor: Prof. Luca Dedè

Co-advisors: Dr. Ivan Fumagalli, Michele Bucelli

Academic Year: 2021-2022

Abstract

In the context of cardiovascular computational fluid dynamics of blood flow in proximity of the aortic valve, this thesis has a twofold objective. First, we investigate a novel reduced order model for blood-valve Fluid-Structure Interaction problem (FSI), with the aim of understanding the role of its parameters and calibrating them towards a physiological scenario. Second, we complement the FSI model with a non-Newtonian model for blood rheology. To the best of our knowledge, the literature lacks studies concerning the usage of a non-Newtonian model in proximity of a physiological trileaflet valve: with this work we try to fill this gap. We implemented the non-Newtonian model, in a high-performance library for cardiac applications, and we validated it with a comparison with the literature. Regarding the FSI simulation conducted in proximity of a realistic aortic valve, we calibrate the parameters of the reduced model in order to obtain a configuration similar to what is physiologically observed in a healthy individual, and two configurations related to the most common pathological cases caused by malfunctioning of the valve. We proved that the healthy configuration is in accordance with most of the physiological parameters measured in the literature during the systole. The comparison between the Newtonian and non-Newtonian models in the two pathological cases confirms that the rheological model has only little influence on quantities such as valve dynamics and transvalvular pressure drop, in accordance with what can be found in the literature. Our results, however, show that considering Newtonian blood rheology leads to an underestimation of the wall shear stress. We thus conclude that the non-Newtonian rheology of blood must be taken into account whenever wall shear stress is in the focus of the clinical investigation.

Keywords: computational fluid dynamics, aortic valve, non-Newtonian fluids, fluid-structure interaction, reduced order models, bioengineering, cardiovascular system.

Abstract in lingua italiana

Nel contesto dello studio della fluidodinamica computazionale del sangue in prossimità della valvola aortica, questa tesi ha un duplice obiettivo. In primo luogo, abbiamo investigato un innovativo metodo ridotto per lo studio dei problemi di interazione fluido-struttura (FSI), con lo scopo di comprendere il ruolo dei diversi parametri del modello e calibrarli in modo da ottenere scenari fisiologici. In secondo luogo, abbiamo accoppiato il modello FSI con un modello non-Newtoniano per la reologia del sangue. Per quanto riguarda la nostra conoscenza, in letteratura mancano studi riguardanti l'utilizzo di un modello non-Newtoniano in prossimità di una valvola fisiologica composta da tre lembi: con questo lavoro abbiamo provato a colmare questa lacuna. Abbiamo implementato il modello non-Newtoniano in una libreria per applicazioni cardiache ad alte performance e lo abbiamo validato confrontandolo con la letteratura. Per quanto riguarda la simulazione FSI condotta in prossimità di una valvola aortica realistica, abbiamo calibrato i parametri del modello ridotto in modo da ottenere una configurazione simile a quella che viene fisiologicamente osservata in un individuo sano, e due configurazioni relative ai più comuni casi patologici causati da un malfunzionamento della valvola. Abbiamo dimostrato che la configurazione sana risulta essere in accordo con la maggior parte dei parametri fisiologici misurati in letteratura durante la sistole. Il confronto tra il modello Newtoniano e non-Newtoniano nei due casi patologici conferma che il modello reologico ha poca influenza su quantità come le dinamiche della valvola e il salto di pressione transvalvolare, in accordo con quello che viene osservato in letteratura. Tuttavia i nostri risultati mostrano che l'utilizzo del modello Newtoniano porta a sottostimare lo sforzo di taglio a parete. Concludiamo quindi che la reologia non-Newtoniana del sangue deve essere tenuta in considerazione se lo sforzo di taglio è nello scopo dell'investigazione clinica.

Parole chiave: fluidodinamica computazionale, valvola aortica, fluidi non-Newtoniani, interazione fluido-struttura, modelli ridotti, bioingegneria, sistema cardiaco.

Contents

Abstract	i
Abstract in lingua italiana	iii
Contents	v
1 Introduction	1
1.1 Heart anatomy and physiology	2
1.2 Anatomy and function of the aortic valve	5
1.3 Pathologies caused by malfunctions of the aortic valve	7
1.4 Blood rheology	8
1.5 Fluid-Structure Interaction problems	10
1.5.1 Fluid-Structure Interaction modeling of the aortic valve	10
1.6 Non-Newtonian models	12
1.6.1 Non-Newtonian models in proximity of the aortic valve	14
1.7 Goal and outline of the thesis	15
2 Mathematical models and methods for blood flow and valve dynamics	17
2.1 Models for Newtonian fluids	17
2.1.1 Navier-Stokes equations	17
2.1.2 Weak formulation of the Navier-Stokes equations	18
2.2 Non-Newtonian model for blood rheology	20
2.2.1 Generalized Newtonian models	20
2.2.2 Carreau model	21
2.2.3 Blood rheology in relation to the shear rate	22
2.3 Reduced method for Fluid-Structure Interaction problem for the valve . .	23
2.3.1 Resistive Immersed Implicit Surface method	23
2.3.2 Lumped parameter mechanical model including leaflets curvature .	25
2.3.3 Coupling between fluid and structure	27

2.4	Numerical methods	28
2.4.1	Time and space discretizations	29
3	Validation of the non-Newtonian model in a cylindrical domain	33
3.1	Steady case	34
3.2	Pulsatile case	36
4	A simulation study on the aortic valve	41
4.1	Setting for the simulations	41
4.1.1	Mesh generation	42
4.1.2	Boundary conditions and baseline parameters	46
4.2	Simulation of a healthy valve	48
4.3	Simulation of pathological cases	54
4.3.1	Comparison with healthy configuration	55
4.4	Comparison between Newtonian and non-Newtonian models in pathological cases	62
4.4.1	Valve's dynamic and pressure jump	63
4.4.2	Wall shear stress	65
5	Conclusions and further development	73
Bibliography		77
A	Appendix A	93
A.1	Sensitivity to parameters of the healthy configuration	93
List of Figures		95
List of Tables		99
List of Symbols		101
Acknowledgements		103
Ringraziamenti		105

1 | Introduction

Cardiovascular diseases are one of the major causes of death: 17.9 million people died because of this kind of diseases in 2019, representing the 32 % of global deaths [6]. Moreover, according to [98] this number is expected to grow to more than 23.6 million by 2030. In Europe this will correspond to nearly half of all deaths (47 %) [98].

As medicine progresses, computational fluid dynamics simulations of blood flow are becoming of increasing interest towards a better understanding of cardiovascular diseases. On top of that, the mathematical and numerical modeling of the cardiovascular system is attracting growing interest also in the mathematical community, because of its intrinsic complexity and its increasing impact worldwide [112].

Within the cardiovascular system, the aortic valve is one of the most investigated components [25, 29, 35, 48, 90, 102, 114, 131, 138]. The main reason for this is that millions of people are annually diagnosed with disorders of the aortic valve [143]. Because numerical models can capture structural details in the flow that cannot be measured experimentally, they can help assess the effect of the morphological configuration on the biomechanics of the valve. Since most of valvular diseases can be treated with surgical procedures [53, 125], computational studies might lead to optimal clinical interventions that can improve the quality of life of patients [35].

In this context, this thesis has a twofold objective. First, with the aim of obtaining different physiological scenarios, we investigated a novel reduced order model [56] for blood-valve Fluid-Structure Interaction problem (FSI). An important effort was performed in understanding the role of the model's parameters and in their calibration towards physiological scenarios. Second, we complemented the FSI model with a non-Newtonian model for blood rheology. Indeed, while the Newtonian rheology is by far the most adopted in literature for this type of simulation, blood is a fluid composed of many elements that exhibits complex rheological properties, and for this reason, the usage of a non-Newtonian model is more accurate for many types of applications. We compared the Newtonian and non-Newtonian modeling approaches, to understand whether the more sophisticated rheology can have a significant impact. In particular, we investigated the differences

observed in wall shear stress (WSS), a quantity that has often great importance in the medical field [79, 95, 103, 144]: for example, it has great influence in the formation of plaque in atherosclerosis [95] or in the wall elasticity [144]. The model was implemented in life^x [5], a high-performance library for the solution of multiphysics and multiscale problems, mainly for cardiac applications.

This chapter aims at giving a brief introduction to the anatomy and physiology of the circulatory system, with particular attention to the cardiac cycle, blood composition and aortic valve physiology and pathology. For more details, we refer to [45] for anatomy, [65] for physiology and [78] for pathology and medical treatments. Then, we will describe the state of the art for the FSI modeling of aortic valves, together with the state of the art of the non-Newtonian treatment for the rheology of the blood in cardiac simulations with particular attention to the simulations in the proximity of the aortic valve. Finally, the goal and the outline of the thesis will be provided.

1.1. Heart anatomy and physiology

The cardiovascular system is composed of the heart, which pumps blood throughout the body, and the blood vessels, which are a closed network of tubes through which blood is transported to the whole body [45].

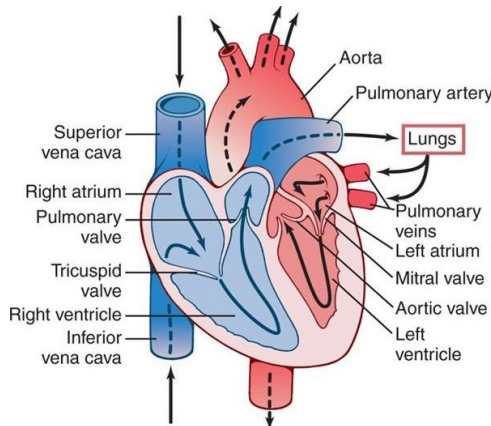


Figure 1.1: Structure of the heart and direction of blood flow through the heart chambers and heart valves; image taken from [65] Figure 9-1.

The heart, shown in Figure 1.1, is composed of two separate pumps: the right heart which pumps blood towards the lungs, and the left heart which pumps blood towards the peripheral organs. Each of these two parts is a pulsatile two-chamber pump composed of an atrium and a ventricle. The atrium is a weak primer pump for the ventricle: it has a

buffer function for the blood entering the heart, and it brings blood into the ventricle. The ventricles then apply the main pumping force that pushes the blood either through the pulmonary circulation for the right ventricle or through the peripheral circulation for the left one [65]. A continuous succession of cardiac contractions called cardiac rhythmicity is caused by subcellular processes that, triggered by bioelectrical signals propagating through the heart, induce the active contraction of the cardiac muscle [65]. The mean action potential in a ventricular muscle fiber is about 105 millivolts: the intracellular potential ranges from -85 millivolts to 20 millivolts, during each heart beat. After the initial spike, the tissue remains depolarized for about 0.2 s, exhibiting a plateau followed by abrupt repolarization. The presence of this plateau is the main cause of ventricular contraction [65].

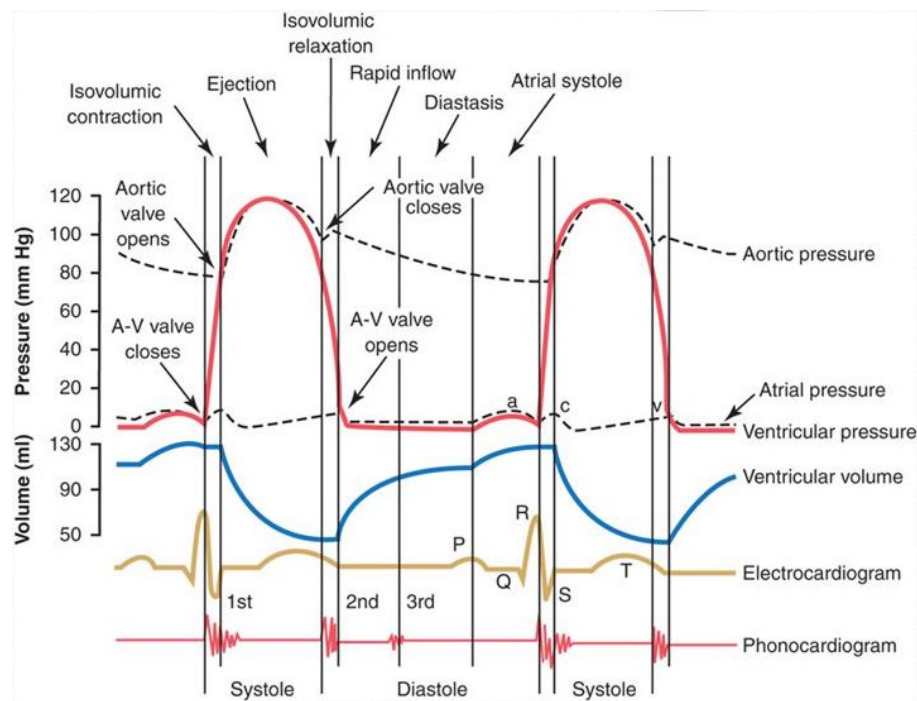
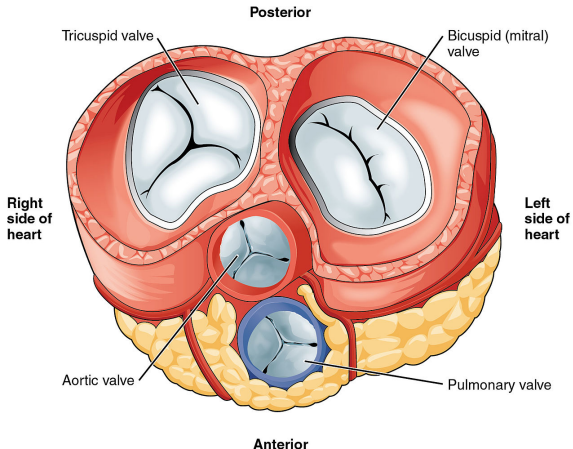


Figure 1.2: Cardiac cycle for left ventricular function, showing changes in left atrial pressure, left ventricular pressure, aortic pressure, ventricular volume, the electrocardiogram, and phonocardiogram; image taken from [65] Figure 9-6.

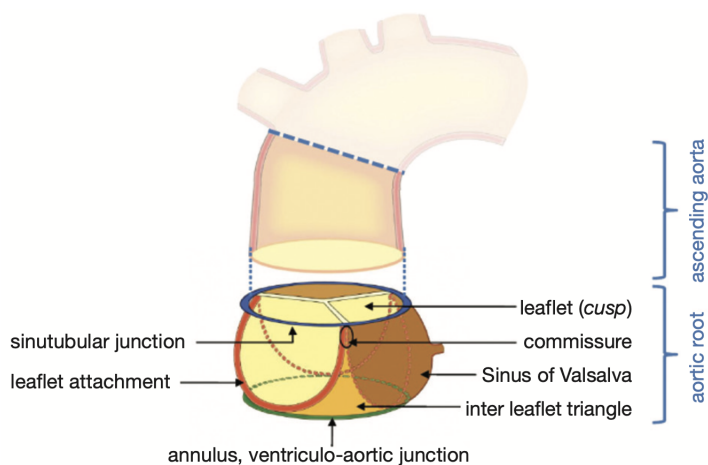
The cardiac cycle consists of a period of relaxation called diastole, when the heart fills with blood, followed by a period of contraction called systole [65]. The typical heart rate is on average 72 beats/min, which corresponds to a duration of the heart cycle of 0.833 s per beat [65]. The different events during the cardiac cycle for the left side of the heart are shown in Figure 1.2. The pressure changes in the aorta, left ventricle, and left atrium are shown in the top three curves, respectively. The fourth curve shows the changes in left

ventricular volume, the fifth the electrocardiogram [28], and the sixth a phonocardiogram [42] i.e., a recording of the sounds produced mainly by the heart valves as it pumps. Then, additional 0.02 to 0.03 s are required for the ventricular pressure to reach the values in the aorta (for the left ventricle) or the pulmonary artery (for the right ventricle), thus inducing the opening of the aortic or pulmonary valves. This happens when the left ventricular pressure rises slightly above 80 mmHg (and the right ventricular one above 8 mmHg). It is important to highlight that before the opening of the semilunar valves, contraction is occurring in the ventricles, but there is no emptying: this is the so-called isovolumic or isometric contraction [65]. Then, blood begins to flow out of the ventricles: in the first third of the period of ejection, about 70 % of the blood emptying occurs, while the remaining 30 % happens in the next two-thirds. At the end of systole, ventricular relaxation begins: this allows intraventricular pressures to decrease. The high pressures in the large arteries, which are now filled with blood, immediately push blood back toward the ventricles. This causes the aortic and pulmonary valves to close. For another 0.03 to 0.06 seconds, the intraventricular pressures decrease back to their low diastolic levels while the ventricular muscle continues to relax, even though the ventricular volume does not change. Then the atrioventricular (A-V) valves open to begin a new cycle of ventricular pumping [65].

1.2. Anatomy and function of the aortic valve



(a) Heart valves; image taken from [76].



(b) Aortic root components; image taken from [30]

Figure 1.3: The four heart valves and structure of the aortic root.

The aortic root connects the heart to the systemic circulation. This is an ensemble consisting of distinct entities: the *aortic valve leaflets*, the *leaflet attachments*, the *sinuses of Valsalva*, the *interleaflet triangles*, the *sinotubular junction* and the *ventriculo-aortic junction* [30], as shown in Figure 1.3. The three aortic valve leaflets form the aortic valve and provide its sealing mechanism. The leaflets compose the hemodynamic junction and constitute the physical boundary between the left ventricle and the aorta. All the upstream parts of the hemodynamic junction are subjected to ventricular hemodynamics, while the more downstream ones are subject to arterial pressures [30]. Anatomically, the trileaflet shape represents the physiological configuration for low resistance valve opening.

Indeed, for other types of configuration, such as congenital bicuspid aortic valve, some kind of valve dysfunction or degree of stenosis always develops [121]. The leaflet attachments are inserted in the wall of the aortic root, where they form a crown-shaped, thick fibrous structure [30]. The three bulges of the aortic wall are named the sinuses of Valsalva. Two of the sinuses host the origin of the coronary arteries. They can be found in the area between the attachments of the leaflets and the sinotubular junction [30]. The precise function of the sinuses of Valsalva is not entirely clear, as of today. Some references claim that the vortices created in the sinuses could lead to stress reduction on the aortic leaflets and support coronary flow [30, 117, 130]. Under each commissure lies one of the three interleaflet triangles. Histologically they consist of a thin aortic wall, while hemodynamically they are extensions of the ventricular outflow: they reach the level of the sinotubular junction in the area of the commissures [30]. The distal part of the sinuses toward the ascending aorta and the commissures form a structure called the sinotubular junction, separating the aortic root from the ascending aorta [30]. Finally, the term ventriculo-aortic junction is used to describe the virtual, circular ring defined by the nadirs of the semi-lunar leaflet attachments: this is the area of the smallest diameter in the blood path between the left ventricle and the aorta [30].

The function of the aortic valve is to prevent backflow from the aorta into the ventricle during diastole. This valve closes and opens passively: it closes when a backward pressure gradient pushes blood backward, and it opens when a forward pressure gradient occurs [65]. The high pressures in the arteries at the end of systole cause the aortic valve to snap to the closed position. Moreover, because of a relatively small opening, the velocity of blood ejection through the aortic is relatively high with respect to the ones of other heart valves. Because of the rapidity of its movement, the aortic valve is subject to high mechanical stress. For this reason, the leaflets are made of an especially strong but very pliable fibrous tissue base [65]. As already mentioned in Section 1.1, after the left ventricle contracts, the ventricular pressure increases rapidly until the aortic valve opens. After the valve opens, the pressure in the ventricle rises more slowly, as shown in Figure 1.2, because blood is immediately ejected from the ventricle into the aorta and then into the other distribution arteries [65]. The entrance of blood into the arteries causes the walls of these arteries to stretch, and the pressure increases to about 120 mmHg. At the end of systole, after the left ventricle stops ejecting blood and the aortic valve closes, the pressure in the arteries remains high thanks to the elastic walls of the arteries, even during diastole. After the aortic valve closes, there is a short period of reverse flow, immediately before the closure of the valve. This causes the so-called *incisura* in the aortic pressure curve [65]. Then, the pressure in the aorta decreases slowly throughout diastole: this happens

because the blood stored in the distended elastic arteries flows continually through the peripheral vessels and to the veins. The pressure falls down to about 80 mmHg (diastolic pressure), corresponding to two-thirds of the maximal pressure of 120 mmHg (systolic pressure) [65].

1.3. Pathologies caused by malfunctions of the aortic valve

Aortic valve pathologies can be classified into *stenosis*, which is the narrowing of the orifice that limits the anterograde flow through the valve, and *regurgitation*, which consists of retrograde flow through the aortic valve. While these pathologies may develop over many years, symptoms may not appear until the condition is severe, and at this point, the mortality of aortic valvular diseases is very high [139]. These diseases may be congenital or acquired, or a combination of the two. The three most common causes of aortic stenosis are age-related calcific degeneration, congenitally bicuspid (or unicuspid) aortic valve, and post-inflammatory valvular disease (such as rheumatic disease). Age-related calcific stenosis is due to the fact that a congenitally normal tricuspid aortic valve undergoes a calcific degenerative process. According to a prospective population-based study [139], the incidence of aortic stenosis is 0.2% during the fifth decade of life, 1.3% during the sixth, 3.9% during the seventh, and 9.8% during the eighth.

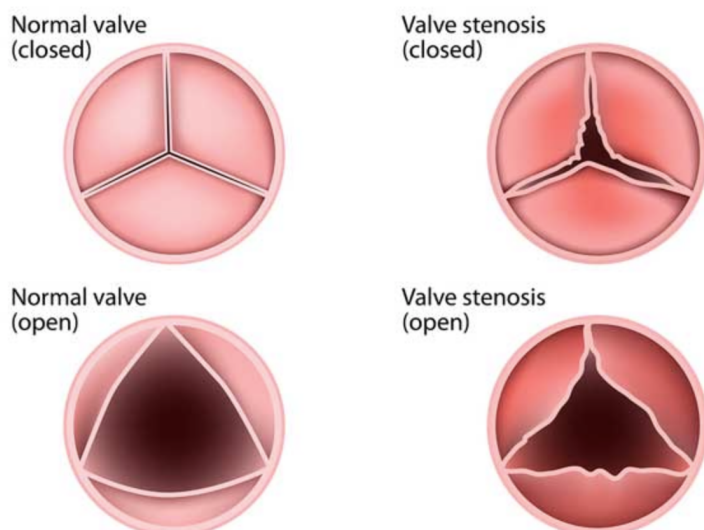


Figure 1.4: Open and closed configuration of healthy and stenotic valve; image taken from [108].

The aortic valve opens and closes about 100 000 times each day. In an 80-year-old person, the valve has opened roughly 2.9 billion times, chronically exposing the valve to significant shear forces that result in progressive degeneration. In this type of stenosis, there is progressive deposition of calcium phosphate affecting all three cusps. In practice, there is dense nodularity of the outflow surface that heaps up and may fill the sinuses of Valsalva. The cusps become anchored to the valve annulus and this impairs cusp mobility. Since the cusps are separate, commissural fusion is absent or minimal. Hence, significant regurgitation is uncommon when this type of stenosis is present [52]. It should be mentioned that in congenitally bicuspid aortic valves these syndromes are much more frequent [52].

Aortic regurgitation is the leaking of the aortic valve of the heart that causes blood to flow from the aorta into the left ventricle during ventricular diastole. As a consequence, the cardiac muscle is forced to work harder than normal. Aortic regurgitation may be the result of abnormalities either of the aortic valve or of the aortic root. Dilatation of the aortic valve annulus, cusp prolapse, retraction of the cusps by scar, and cusp perforation are the main causes of regurgitation [52]. Finally, it should be mentioned that rheumatic-type post-inflammatory aortic valve disease may result in mixed aortic stenosis and regurgitation [52].

1.4. Blood rheology

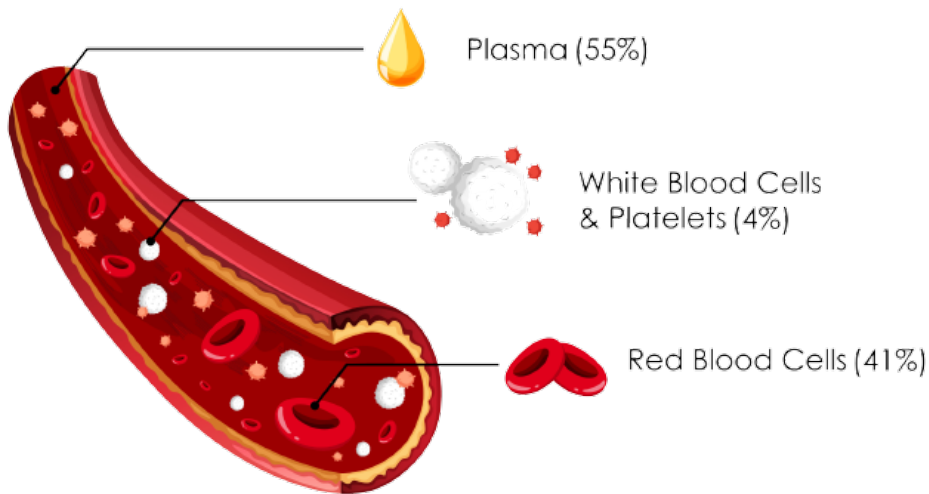


Figure 1.5: Composition of blood; image taken from [3].

Blood is a complex fluid composed of many elements, such as red blood cells (or erythrocytes), white blood cells and platelets, suspended in an aqueous solution of organic molecules, proteins, and salts called plasma [120], as shown in Figure 1.5. Due to this

multicomponent nature, blood exhibits complex rheological properties. Blood plasma, which consists mostly of water, is a Newtonian fluid, that is, a fluid which satisfies Newton's law of viscosity: the shear stress is proportional to the rate of shear and the viscosity of the fluid is the constant of proportionality.

This is why the assumption of Newtonian flow is generally accepted for computational fluid dynamics models of blood flow in large-sized arteries, such as the aorta, where the shear rate is usually high [64]. Blood, however, has more complex mechanical properties.

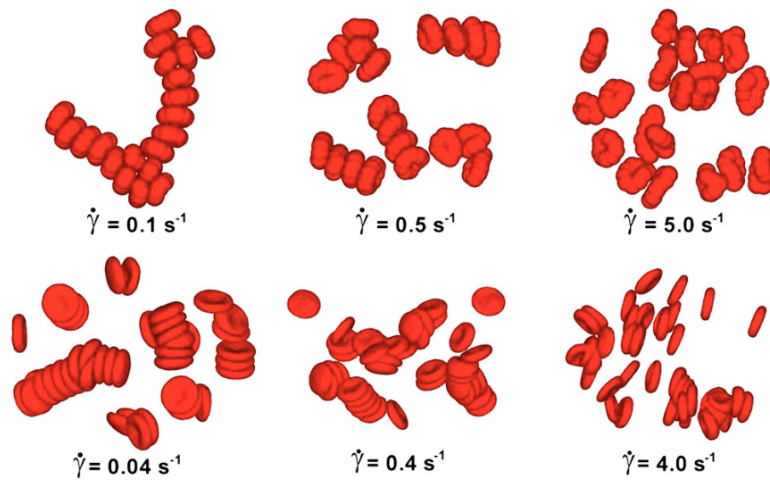


Figure 1.6: Visualization of aggregation. The left column corresponds to low shear rates, the center column to moderate shear rates, and the right column to high shear rates; image taken from [50].

Indeed, at low shear rates, the erythrocytes tend to aggregate as shown in Figure 1.6. These aggregates are known as rouleaux and are formed under the influence of bridging macromolecules, especially fibrinogen. These trains of rouleaux will increase the viscosity of blood. Decreasing the shear rate even further, the rouleaux will form three-dimensional structures, inducing an additional increase of viscosity. On the contrary, if the shear rate is increased, the rouleaux will break up and the erythrocytes will align with the flow. If the shear rate is further increased, it will be high enough to deform the erythrocytes, thus decreasing the viscosity [132]. This process involving aggregation of red blood cells was validated experimentally and mathematically by [50]. For these reasons, blood generally has, larger viscosity than plasma, and when the volume percentage of RBC (the hematocrit) rises, the viscosity of the suspension increases, and the non-Newtonian behavior of blood becomes more relevant: this happens especially at very low shear rates. In conclusion, blood features a shear-thinning behavior, that is, its viscosity decreases with

increasing shear rates, reaching a nearly constant value of approximately $0.00345 \text{ Pa} \cdot \text{s}$ for shear rates larger than 200 s^{-1} [34].

1.5. Fluid-Structure Interaction problems

From a mathematical point of view, studying what happens in proximity of the aortic valve, concerning the hemodynamics of blood and the dynamic of the valve itself, is interesting because of the inherent complexity of the problem: not only the blood flow has to be modeled, but also the interaction with the mechanical structure of the valve has to be taken into account.

1.5.1. Fluid-Structure Interaction modeling of the aortic valve

The problems in which the interaction between a fluid and a mechanical structure is studied are known in literature as FSI: increasing interest is growing in the last years in the study of these methods, particularly in the cardiac context [17, 22, 75]. In the context of cardiovascular simulations, these models can be used to study the interaction between the blood and the wall of the vessels [17, 75] or the behavior of a cardiac chamber [22, 33, 93, 100], but they become of fundamental importance in the modeling of the coupling of valve dynamics and blood flow. Computational fluid dynamics method for FSI simulations of cardiac valves can be mainly grouped into four different categories [49]: the approaches based on the so-called Arbitrary Lagrangian Eulerian (ALE) formulation [123], those based on the immersed boundary (IB) methods [63, 106, 107, 122], those based on fictitious domain (FD) formulations [37, 38, 97, 133], and those based on hybrid formulations [20, 21, 59, 60, 82].

The ALE approach is based on the arbitrary movement of a frame of reference which, additionally to the common material domain and spatial domain, is introduced as a third reference. The arbitrary movement of this reference frame must be accompanied by a suitable mesh moving algorithm [123]. This approach, however, is known to be problematic when dealing with large deformations, which may require frequent remeshing and become computationally very expensive. Moreover, valve opening and closing lead to topological changes in the domain, which are hard to account for in the ALE framework [49]. Other mesh-conforming methods are XFEM [12, 23, 54, 61, 62, 91, 92, 147] and CUTFEM [67, 118]: both these methods also update the computational mesh over time. In IB methods, the Navier–Stokes equations are solved on a fixed background grid. The fluid–structure interfaces are represented by independent surface meshes and their effects on the flow are accounted for by introducing fictitious body forces in the governing equa-

tions [122]. Often the appropriate forces are explicitly added to the fluid equation and distributed over all nodes of the fluid mesh through a smoothed Dirac delta function [106, 107]. Another version of this method, when the mesh is adaptively refined in the proximity of the IB, can be found in [63]. A similar idea is followed in FD methods, but in this case the coupling between the fluid and solid meshes is performed through Lagrange multipliers (or local body forces) at the boundary of the solid [133]. This method applied to the case of heart valves can be found in [37, 38, 97]. Finally, among hybrid formulations, the curvilinear immersed boundary (CURVIB) method [59] should be mentioned: in this method, the IB forces are integrated over structured curvilinear boundary fitted grids. Application of this method can be found in [20, 21, 60, 82]. Another hybrid method is the ALE/IB immersogeometric method: this combines a variational IB method with the traditional ALE technique [70, 77].

The common characteristic of all mentioned methods is that they require a full 3D representation of the valve geometry and of its mechanics solver, thus entailing a significantly increased computational cost with respect to imposed-displacement hemodynamics [56]. Besides computational issues, when considering patient-specific simulations starting from clinical data, even if the constitutive law of the valves is assumed to be known, it would be extremely difficult to parametrize it for that specific patient [14]. A method that can deal with both these issues in the representation of the valve was proposed in [14], adapting a method originally proposed for the study of porous interfaces immersed in a fluid in [51]. This method is named Resistive Immersed Surface (RIS) method: in this approach, the valve is replaced by a set of immersed surfaces that act like resistances in the fluid [14]. In [49] the RIS method is extended by representing the valve surfaces implicitly through a level set formulation for the leaflets, leading to the Resistive Immersed Implicit Surface (RIIS) method, which does not need the mesh to be conforming to the immersed surface. This method was recently modified by introducing a reaction term to correctly capture the pressure transients during isovolumetric phases, producing the so-called Augmented-RIIS method [146].

Concerning the dynamics of the surface, two different approaches could be employed: the kinematic movement of the valve can be prescribed or governed by a mechanical equation. If the movement is prescribed the whole simulation could be less accurate since this approach does not take into account the dynamic of the fluid. The use of a mechanical equation, on the contrary, requires a coupling between the two physics of the problem. This equation should be a 3D equation, but this rises by a lot the computational time of the simulation. For this reason, a 0D equation could be used [49, 56]. In particular, to reproduce the dynamics of the valve, different lumped-parameters models can be chosen

for the 0D model: in [49] a model proposed in [80] is used, while other examples of lumped-parameters models often used in cardiovascular applications can be found in [19, 113]. Usually, in this type of model the valve hemodynamics are controlled by the pressure jump across the leaflets and the flow rate passing through them. However, with this type of model the calibration of the parameters of the model could be difficult, since these parameters rarely have a precise physical meaning. Other methods rely on momentum balance of the leaflets. This approach was first adopted by [43] neglecting the inertia and stiffness of the leaflets and in [119] where the opening coefficient of the valve is controlled by a linear ordinary differential equation. More recently, a novel lumped-parameter structure model for the aortic valve was introduced by [56]: this model is derived from the balance forces at the leaflets relating the elasticity of the leaflets to their curvature. This approach directly accounts for the valve geometry: it relates it with the flow-induced forces to which the leaflets are subject. In this thesis, this last model was chosen for the 0D modeling of the valve [56], coupled with the Resistive Immersed Implicit Surface (RIIS) method proposed in [49]. This choice was performed because of the capability of the model to improve the computational performance of the simulations with respect to other popular approaches used in the literature, which require a full 3D representation of the valve geometry and of its mechanics solver, while retaining a physical meaning for the parameters of the 0D equations.

1.6. Non-Newtonian models

Another important characteristic to consider when performing cardiovascular simulations is the rheology of blood. As mentioned in Section 1.4, blood has a multicomponent nature that leads to a complex rheology.

The assumption of Newtonian flow is generally accepted for blood flow in large-sized arteries, such as the aorta, where the shear rate is usually high [46, 58, 64, 104, 105, 112]. However, at low shear rates, the erythrocytes tend to aggregate and, consequently, the viscosity of the blood increases [50, 132]. On the contrary, if the shear rate increases, it will eventually be high enough to deform the erythrocytes, thus decreasing the viscosity [132]. This is why, particularly in small vessels, where the dimension of the red blood cells tends to become more relevant, blood has been modeled like a non-Newtonian fluid in different works [10, 13, 31, 32, 34, 64, 74, 84–86, 88, 96, 99, 109, 110, 128, 134, 136, 137]. Different types of models can be used for the treatment of non-Newtonian viscosity. The most used ones are the so-called “generalized Newtonian models”, for which a relation between the viscosity and the scalar strain rate is introduced. This dependency is introduced through

a constitutive equation and, depending on the specific relation used, different types of models can develop. This category of models contains Power Law [87], a model analyzed for example in [34, 74, 110] and used in [31, 99]; Casson [134], analyzed in [34, 74, 110] and used in [31, 109, 134] and the model used in this thesis: Carreau [34], with its variant, Carreau-Yasuda [34], that are the two most used in literature for simulation of blood flow with non-Newtonian treatment [32, 64, 84–86, 96, 128]. For a comparison of all these models, the reader can refer to [74] where six non-Newtonian models were compared for the simulation of pulsatile blood flow in a stenosed artery. Finally, more complex models should be mentioned, such as the viscoelastic model: this type of model is used, for example, in [7, 142]. In many of these works, the question that the authors try to answer is for what kind of simulations and for what quantities of interest the use of a non-Newtonian model produces some differences with respect to a standard Newtonian model.

In [84], the subjects of the investigation were the distributions of luminal surface concentration and oxygen flux along the wall of the human aorta. The authors found the shear-thinning nature of blood has little effect in the mass transport, but its effect is apparent in the areas where luminal surface LDL cholesterol concentration is high, and oxygen flux is low. In [96], simulations on the carotid bifurcation showed a difference of less than 10 % between the Newtonian and non-Newtonian rheology, in terms of bulk flow metrics. However, the rheological model affected more significantly the WSS-based indicators. In [64], Newtonian and non-Newtonian (Carreau-Yasuda) models were compared in stenotic carotid arteries and in stenotic coronary arteries. In the carotid case, the results show that velocity, vorticity, and wall shear stress distributions are only moderately influenced by the non-Newtonian rheology. In the coronary case, on the other hand, the rheological model seems to be important, in particular with respect to residence time of stenosis. In [136], numerical results computed for non-Newtonian blood flow in three aorto-coronary bypasses show that the blood flow does not significantly differ from the Newtonian one. In [32], results lead to the conclusion that the non-Newtonian properties of the blood alter the flow pattern and WSS, so that non-Newtonian rheology is an important factor to be considered in simulating hemodynamic effects of blood flow in arterial bypass grafts. Finally, [13] should be mentioned, in which a novel hybrid Newtonian and non-Newtonian rheology model was proposed, where the shear-thinning behavior is activated only in regions with high residence time of red blood cells, based on experimental data. The authors suggest that conventional approaches to non-Newtonian blood modeling should be revisited, to account for more complex rheological behavior in large artery flows.

1.6.1. Non-Newtonian models in proximity of the aortic valve

In most of the studies conducted in the proximity of the aortic valve [25, 29, 35, 48, 49, 56, 90, 102, 114, 131, 138] the blood is considered Newtonian. However, as observed by the result obtained in [44], the Newtonian assumption cannot adequately simulate the flow dynamics within the left ventricle over the cardiac cycle, and this can be attributed to the pulsatile and recirculating nature of the flow, that yields a low blood shear rate in some regions: this is the case also in proximity of the aortic valve. Despite this observation, only few works can be found where the simulation of the aortic valve dynamics uses a non-Newtonian model [8, 11, 39, 89, 94, 149]. In particular, [8, 39, 149] are focused on the study of different non-Newtonian models on a bileaflet mechanical heart. In [8], an ALE approach is used for the fluid-structure interaction problem and the Carreau-Yasuda model is employed as rheological model: the average wall shear stress on the fully closed leaflets was found to be 58 % higher compared to Newtonian modeling, thus concluding that blood must be modeled as non-Newtonian fluid to achieve accurate predictions. Also in [39], the Carreau-Yasuda model is compared with the Newtonian one: it is concluded that some features such as valve dynamics, transvalvular pressure drop and large-scale flow structure are similar to the Newtonian case, while significant differences were observed in the mechanical damage to the red blood cells, due to a different shear stress. Instead, in [149], Carreau is used to model the rheology of the blood: their results do not show significant influence caused by the rheological model. However, they conclude that this could be caused by the turbulence model adopted: indeed, as they state, significant differences could be found in the comparison between the experimental results and numerical ones. In [94], it is observed that the Newtonian assumption can be used for modeling blood flow of a healthy aortic valve, but a non-Newtonian rheology should be used in the case of calcified aortic valves, to prevent an underestimation of the wall shear stress in certain core leaflet regions. In [89], a Power-Law non-Newtonian model is used for the simulation of a closed aortic valve, to study the effect of regurgitation, although no comparison with the Newtonian approach is carried out. In [11] an artificial heart pump was studied with both Casson and Carreau models and also in this case the results highlight the need to treat the blood as a non-Newtonian fluid. Indeed, the inclusion of the non-Newtonian model appeared to provide a favorable impact on prediction with respect to comparison with experimental data, in particular concerning turbulent kinetic energy and recirculation regions in the chamber and beyond the valves. Overall, all works discussed above consider the inclusion of non-Newtonian rheology to be important. However, to the best of our knowledge, non-Newtonian models have never been used in conjunction with reduced FSI models to study a trileaflet physiological aortic valve.

1.7. Goal and outline of the thesis

The goal of the present thesis is twofold. First, it aims at filling the gap in the literature concerning the use of a non-Newtonian model in proximity of a physiological trileaflet valve. Second, differently from what can be found in the literature, it employs a reduced model with momentum balance of the leaflets as 0D equation for the treatment of the fluid-structure interaction problem, a method that could drastically improve the computational performance of the simulation while retaining a physical meaning for the parameters of the 0D equations. In order to effectively use this model to represent physiological and pathological cases, an important work in the understanding of the model and in the tuning of the different parameters was performed.

The remaining part of the present work is structured as follows:

- In Chapter 2, the mathematical model and the numerical methods used to perform the simulation are introduced. In particular, we present the Navier-Stokes equations, the non-Newtonian model, the Resistive Immersed Implicit Surface model used to model the fluid-structure interaction problem, the 0D equation used to mimic the dynamic of the valve and the complete numerical scheme.
- In Chapter 3, we perform the validation of the non-Newtonian model implemented in a cylindrical domain, comparing the results obtained with ones that can be found in the literature.
- In Chapter 4, we show the most important numerical results. In particular, we present the setting for the simulations, the results obtained in a healthy valve, the ones obtained in the two most common pathological cases and, finally, the comparison obtained using the two different types of rheology (Newtonian and non-Newtonian).
- In Chapter 5, we present a critical analysis of the results obtained in this thesis together with an analysis of the limitations of this work and possible further development.

2 | Mathematical models and methods for blood flow and valve dynamics

In this chapter, the mathematical models used in this thesis to simulate the blood flow and the valve dynamics are presented. In particular, the classical Navier-Stokes equations are introduced: these are the equations that are used for computational fluid dynamics of a Newtonian fluid. Then the non-Newtonian model used to deal with the complex rheology of the blood is described. After this, the Resistive Immersed Implicit Surface (RIIS) used to simulate the interaction between the fluid and the valve; and the 0D model of the dynamics of the valve is introduced. Finally, the numerical approximation for the complete model (RIIS 3D-0D model for a non-Newtonian fluid) is presented.

2.1. Models for Newtonian fluids

We model blood flow as an incompressible fluid, by means of the Navier-Stokes equations. In this section, these equations are introduced for the Newtonian case, with some mentions to the more general case.

2.1.1. Navier-Stokes equations

Navier-Stokes equations for incompressible homogeneous fluids constitute the main mathematical model to describe the motion of viscous flows. This system consists in a set of partial differential equations that mathematically express conservation of momentum and conservation of mass for Newtonian or even more general fluids [27]. The Navier-Stokes equations for an incompressible homogeneous isothermal fluid in convective form read as follows:

$$\begin{cases} \rho \frac{\partial \mathbf{u}}{\partial t} + \rho(\mathbf{u} \cdot \nabla) \mathbf{u} - \nabla \cdot \boldsymbol{\sigma} = \mathbf{f} & \text{in } \Omega \times (0, T), \\ \nabla \cdot \mathbf{u} = 0 & \text{in } \Omega \times (0, T), \\ \mathbf{u} = \mathbf{g} & \text{on } \Gamma_D \times (0, T), \\ \boldsymbol{\sigma} \mathbf{n} = \mathbf{h} & \text{on } \Gamma_N \times (0, T), \\ \mathbf{u}(\mathbf{x}, 0) = \mathbf{u}_0(\mathbf{x}) & \text{in } \Omega \times \{0\}. \end{cases} \quad (2.1)$$

The system is solved in the spatial domain $\Omega \subset \mathbb{R}^3$ for all the time instants in the interval $(0, T)$ where $T \in \mathbb{R}^+$ and the boundary $\partial\Omega$, with outward normal vector \mathbf{n} , is partitioned into a Dirichlet boundary Γ_D and a Neumann boundary Γ_N such that $\Gamma_D \cup \Gamma_N = \partial\Omega$ and $\Gamma_D \cap \Gamma_N = \emptyset$. The unknowns of the systems are the fluid velocity field $\mathbf{u} : \Omega \times [0, T] \rightarrow \mathbb{R}^3$ and the pressure $p : \Omega \times [0, T] \rightarrow \mathbb{R}$. ρ is the density of the fluid and $\boldsymbol{\sigma}$ is the stress tensor, and it is a function of p, \mathbf{u} and the dynamic viscosity μ . Under the assumption of Newtonian fluid, the stress tensor can be written in the form $\boldsymbol{\sigma} = -p\mathbf{I} + 2\mu\varepsilon(\mathbf{u})$, where \mathbf{I} is the identity tensor and $\varepsilon(\mathbf{u}) = \frac{1}{2}(\nabla\mathbf{u} + (\nabla\mathbf{u})^T)$ is the strain rate tensor. In this case System (2.1) becomes:

$$\begin{cases} \rho \frac{\partial \mathbf{u}}{\partial t} + \rho(\mathbf{u} \cdot \nabla) \mathbf{u} - \nabla \cdot (2\mu\varepsilon(\mathbf{u})) + \nabla p = \mathbf{f} & \text{in } \Omega \times (0, T), \\ \nabla \cdot \mathbf{u} = 0 & \text{in } \Omega \times (0, T), \\ \mathbf{u} = \mathbf{g} & \text{on } \Gamma_D \times (0, T), \\ -p\mathbf{n} + 2\mu\varepsilon(\mathbf{u})\mathbf{n} = \mathbf{h} & \text{on } \Gamma_N \times (0, T), \\ \mathbf{u}(\mathbf{x}, 0) = \mathbf{u}_0(\mathbf{x}) & \text{in } \Omega \times \{0\}. \end{cases} \quad (2.2)$$

2.1.2. Weak formulation of the Navier-Stokes equations

We define the following functional spaces:

$$V = \left\{ \mathbf{v} \in [H^1(\Omega)]^3 : \mathbf{v}|_{\partial\Omega_D} = \mathbf{g} \right\}, V_0 = \left\{ \mathbf{v} \in [H^1(\Omega)]^3 : \mathbf{v}|_{\partial\Omega_D} = \mathbf{0} \right\},$$

$$Q = \begin{cases} L^2(\Omega) & \text{if } \Gamma_N \neq \emptyset \\ L_0^2(\Omega) & \text{if } \Gamma_N = \emptyset. \end{cases}$$

We make the following assumptions on the data:

$$\begin{aligned} \mathbf{f} &\in L^2(\mathbb{R}^+, [L^2(\Omega)]^3), & \mathbf{g} &\in L^2(\mathbb{R}^+, [H^{\frac{1}{2}}(\Gamma_D)]^3), \\ \mathbf{h} &\in L^2(\mathbb{R}^+, [H^{-\frac{1}{2}}(\Gamma_N)]^3), & \mathbf{u}_0 &\in [H^1(\Omega)]^3. \end{aligned}$$

For further information on these function spaces and relative assumptions, we refer to [116]. Under these assumptions, a weak formulation of Equation (2.2) can be obtained by multiplying the momentum conservation equation by a test function $\mathbf{v} \in \mathbf{V}$ and integrating in Ω :

$$\begin{aligned} \int_{\Omega} \rho \frac{\partial \mathbf{u}}{\partial t} \cdot \mathbf{v} d\Omega - \int_{\Omega} \nabla \cdot (2\mu\varepsilon(\mathbf{u})) \cdot \mathbf{v} d\Omega \\ + \int_{\Omega} \rho[(\mathbf{u} \cdot \nabla)\mathbf{u}] \cdot \mathbf{v} d\Omega + \int_{\Omega} \nabla p \cdot \mathbf{v} d\Omega = \int_{\Omega} \mathbf{f} \cdot \mathbf{v} d\Omega \quad \forall \mathbf{v} \in \mathbf{V}. \end{aligned} \quad (2.3)$$

Similarly, by multiplying the mass conservation equation by a test function $q \in Q$ and integrating over Ω , we obtain:

$$\int_{\Omega} q \nabla \cdot \mathbf{u} d\Omega = 0 \quad \forall q \in Q. \quad (2.4)$$

After integrating by parts the second and the fourth term of Equation (2.3), using the Neumann boundary condition in Equation (2.2), we obtain the weak formulation, which can be stated as follows:

Find $\mathbf{u} \in L^2(\mathbb{R}^+; [H^1(\Omega)]^3) \cap C^0(\mathbb{R}^+; [L^2(\Omega)]^3)$, $p \in L^2(\mathbb{R}^+; Q)$ such that:

$$\left\{ \begin{array}{l} \int_{\Omega} \rho \frac{\partial \mathbf{u}}{\partial t} \cdot \mathbf{v} d\Omega + \mathcal{D}(\mathbf{u}, \mathbf{v}; \mu) + \int_{\Omega} \rho[(\mathbf{u} \cdot \nabla)\mathbf{u}] \cdot \mathbf{v} d\Omega, \\ \quad - \int_{\Omega} p \nabla \cdot \mathbf{v} d\Omega = \int_{\Omega} \mathbf{f} \cdot \mathbf{v} d\Omega + \int_{\Gamma_N} \mathbf{h} \cdot \mathbf{v} d\gamma \quad \forall \mathbf{v} \in \mathbf{V}, \\ \int_{\Omega} q \nabla \cdot \mathbf{u} d\Omega = 0 \quad \forall q \in Q, \\ \mathbf{u} = \mathbf{g} \quad \text{on } \Gamma_D \times (0, T), \\ \mathbf{u}(\mathbf{x}, 0) = \mathbf{u}_0(\mathbf{x}) \quad \text{in } \Omega \times \{0\}, \end{array} \right. \quad (2.5)$$

where $\mathcal{D}(\mathbf{u}, \mathbf{v})$ is the diffusion term: its form gives rise to three different formulations of the weak problem:

$$\mathcal{D}(\mathbf{u}, \mathbf{v}) = \begin{cases} \int_{\Omega} \mu \nabla \mathbf{u} \cdot \nabla \mathbf{v} d\Omega & \text{Grad-Grad formulation} \\ \int_{\Omega} 2\mu\varepsilon(\mathbf{u}) \cdot \nabla \mathbf{v} d\Omega & \text{SymGrad-Grad formulation} \\ \int_{\Omega} 2\mu\varepsilon(\mathbf{u}) \cdot \varepsilon(\mathbf{v}) d\Omega & \text{SymGrad-SymGrad formulation.} \end{cases} \quad (2.6)$$

The latter two expressions are consistent with Equation (2.2). In this thesis, we adopt the SymGrad-Grad formulation. The details for the procedure to obtain the weak formulation

are available in many references, for instance in [116], while for more details on the derivation of the Navier-Stokes system one can refer to [27]. Finally, defining with (\cdot, \cdot) the scalar product in $L^2(\Omega)$ and the following forms and linear functional:

$\tilde{a} : V \times V \rightarrow \mathbb{R}$, $b : V \times Q \rightarrow \mathbb{R}$, $c : V \times V \times V \rightarrow \mathbb{R}$, $F : V \rightarrow \mathbb{R}$ such that:

$$\begin{aligned} a(\mathbf{u}, \mathbf{v}) &:= \mathcal{D}(\mathbf{u}, \mathbf{v}), \\ b(\mathbf{v}, p) &:= - \int_{\Omega} p \nabla \cdot \mathbf{d} d\Omega, \\ c(\mathbf{w}, \mathbf{u}, \mathbf{v}) &:= \int_{\Omega} \rho((\mathbf{w} \cdot \nabla) \mathbf{u}) \cdot \mathbf{v} d\Omega, \\ F(\mathbf{v}) &:= \int_{\Omega} \mathbf{f} \cdot \mathbf{v} d\Omega + \int_{\partial\Omega_N} \mathbf{h} \cdot \mathbf{v} d\gamma. \end{aligned} \tag{2.7}$$

we obtain the more compact formulation:

given $\mathbf{u}(t = 0) = \mathbf{u}_0$, for each $t > 0$, find $\mathbf{u} \in L^2(\mathbb{R}^+; V) \cap C^0(\mathbb{R}^+; [L^2(\Omega)]^3)$ and $p \in L^2(\mathbb{R}^+; Q)$ such that, for all $v \in V_0$ and $q \in Q$:

$$\left\{ \begin{array}{l} \left(\rho \frac{\partial \mathbf{u}}{\partial t}, \mathbf{v} \right) + a(\mathbf{u}, \mathbf{v}) \\ + c(\mathbf{u}, \mathbf{u}, \mathbf{v}) + b(\mathbf{v}, p) = F(\mathbf{v}) \\ - b(\mathbf{u}, q) = 0. \end{array} \right. \tag{2.8}$$

2.2. Non-Newtonian model for blood rheology

In this section, we introduce the non-Newtonian model that we use to account for the shear-thinning rheology of blood.

2.2.1. Generalized Newtonian models

In a CFD simulation, in order to take into account the non-Newtonian nature of blood, one needs a constitutive equation that describes the relation between the viscosity and the shear rate. If, as it usually happens for blood flow simulations, the viscosity is assumed to be dependent only on the shear rate, one may use as constitutive equation one of the equations developed for the so-called “generalized Newtonian fluids”, for which a relation between the viscosity and the scalar strain rate $\dot{\gamma}$, defined as $\dot{\gamma} = \sqrt{2 \operatorname{tr}(\boldsymbol{\varepsilon}(\mathbf{u})^2)}$, is introduced. This dependency must be such that the constitutive equation is frame invariant:: this is achieved if and only if the set of variables is a subset of the invariants of the tensor $\boldsymbol{\varepsilon}(\mathbf{u})$ [132].

The generalized Newtonian constitutive equation reads as $\boldsymbol{\sigma} = -p\mathbf{I} + 2\mu(II_{\varepsilon})\varepsilon(\mathbf{u})$, where II_{ε} represents the second invariant of the strain rate tensor. Recalling that for incompressible flows $\text{tr}(\varepsilon(\mathbf{u})) = \nabla \cdot \mathbf{u} = 0$, we have $II_{\varepsilon} = -\frac{1}{2}(\text{tr}(\varepsilon(\mathbf{u})^2))$, therefore, the constitutive equation for generalized Newtonian fluids can be written as:

$$\boldsymbol{\sigma} = -p\mathbf{I} + 2\mu(\dot{\gamma})\varepsilon(\mathbf{u}) \quad (2.9)$$

where the function $\mu(\dot{\gamma})$ must be specified.

2.2.2. Carreau model

One of the most used models for $\mu(\dot{\gamma})$ in the context of blood simulations is the Carreau model, in which the equation for the viscosity is given by

$$\mu(\dot{\gamma}) = \mu_{\infty} + (\mu_0 - \mu_{\infty}) [1 + (\lambda\dot{\gamma})^2]^{\frac{n-1}{2}}, \quad (2.10)$$

and shown in Figure 2.1, where

$$\begin{array}{cccc} \mu_{\infty} [\text{Pa} \cdot \text{s}] & \mu_0 [\text{Pa} \cdot \text{s}] & n [\cdot] & \lambda [\text{s}] \\ 3.45 \times 10^{-3} & 5.6 \times 10^{-2} & 0.3568 & 3.313 \end{array}$$

Table 2.1: Carreau's model parameters.

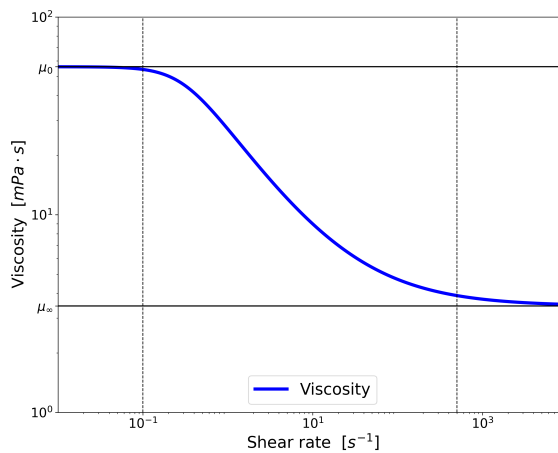


Figure 2.1: Relation between shear rate and dynamic viscosity according to Carreau model, given by Equation (2.10).

These values for the parameters are well established in the literature, and they were first obtained in [34] by numerical fitting of experimental data. It should be noticed that μ_{∞}

corresponds to the constant viscosity usually imposed in the Newtonian case, so the model falls back onto the usual Newtonian model as the shear stress goes to $+\infty$. This model was proven to fit well experimental data, as can be seen for example in [16, 34, 128]. It should be noticed that the introduction of this constitutive equation leads to an additional non-linear term in the Navier-Stokes equations, since now the viscosity depends on the solution \mathbf{u} : this will be better discussed in Section 2.4. From now on we will explicitly state the dependency of the problem on the viscosity in the definition of bilinear forms that include it. So, regarding the definition of the bilinear forms provided in Equation (2.7) we will now have: $\tilde{a} : V \times V \times \mathbb{R} \rightarrow \mathbb{R}$:

$$\tilde{a}(\mathbf{u}, \mathbf{v}, \mu) := \mathcal{D}(\mathbf{u}, \mathbf{v}, \mu) \quad (2.11)$$

with the corresponding weak formulation of the problem:

given $\mathbf{u}(t = 0) = \mathbf{u}_0$, for each $t > 0$, find $\mathbf{u} \in L^2(\mathbb{R}^+; V) \cap C^0\left(\mathbb{R}^+; [L^2(\Omega)]^3\right)$ and $p \in L^2(\mathbb{R}^+; Q)$ such that, for all $\mathbf{v} \in V_0$ and $q \in Q$:

$$\begin{cases} \left(\rho \frac{\partial \mathbf{u}}{\partial t}, \mathbf{v} \right) + \tilde{a}(\mathbf{u}, \mathbf{v}, \mu) \\ + c(\mathbf{u}, \mathbf{u}, \mathbf{v}) + b(\mathbf{v}, p) = F(\mathbf{v}) \\ - b(\mathbf{u}, q) = 0. \end{cases} \quad (2.12)$$

2.2.3. Blood rheology in relation to the shear rate

To give a more concrete idea about the Carreau model, usually cardiovascular handbooks consider blood viscosity values between 3.5×10^{-3} and 5.5×10^{-3} Pa · s to be normal [47]. However, blood viscosity cannot be summarized by a single value. As mentioned in Section 1.4 due to the shear thinning property of blood, the viscosity of this fluid changes depending on the hemodynamic conditions. For example, in correspondence of a very low shear rate, the viscosity can even reach a physiological value of 6×10^{-2} Pa · s [72]. According to Equation (2.10) the value of the viscosity is driven by the shear rate, which is a function of the symmetric velocity gradient. In particular, looking at Figure 2.1 we can roughly identify 3 regions:

- a high viscosity plateau, corresponding to a value of the shear rate $< 10^{-1}$ s $^{-1}$, for which the value of the viscosity is approximately constant and equal to $\mu_0 = 5.6 \times 10^{-2}$ Pa · s,
- a transition region for a value of the shear rate between 10^{-1} s $^{-1}$ and 5×10^2 s $^{-1}$. In this region, the viscosity is very sensitive to the shear rate.

- a low viscosity plateau, for a shear rate $> 5 \times 10^2 \text{ s}^{-1}$. In this region, the viscosity can be considered constant and equal to $\mu_\infty = 3.45 \times 10^{-3} \text{ Pa} \cdot \text{s}$, i.e., the value employed in Newtonian models.

Since the shear rate grows with the magnitude of the symmetric velocity gradient, we can draw some hypotheses on the expected distribution of the viscosity corresponding to a blood flow in a cylindrical domain. For example, in the case of a parabolic velocity profile over a circular section, since the velocity gradient is null in the center, and it increases moving towards the boundary, we should expect a high value for the viscosity in the region near the center of the section.

2.3. Reduced method for Fluid-Structure Interaction problem for the valve

In this section, we present the reduced order model used to solve the fluid-structure interaction problem, together with the 0D model used for the representation of the dynamic of the valve and how these two models are coupled. In particular, in Section 2.3.1 we introduce the RIIS model [49], while in Section 2.3.2 we present a lumped parameter momentum balance 0D equation for the valve and in Section 2.3.3 we follow the procedure used in [56] in order to couple the RIIS model and the 0D equation for the valve. All these methods are generalized for the case of non-Newtonian rheology.

2.3.1. Resistive Immersed Implicit Surface method

As explained in Section 1.5.1, to model the fluid-structure interaction problem we adopt the Resistive Immersed Implicit Surface (RIIS) method [49] coupled with a lumped parameter momentum balance 0D equation for the valve [56]. We introduce the RIIS model in this section. We recall that this method was obtained in [49], starting from the Resistive Immersed Surface (RIS) model presented in [14, 51].

Then the RIIS method consists in implicitly describing the immersed surface Γ [101]. This is done following the approach used in [56]: when the geometry of the moving immersed surface Γ_t is implicitly described at each time t by a single level-set function $\varphi_t : \Omega \rightarrow \mathbb{R}$, as

$$\Gamma_t = \{\mathbf{x} \in \Omega : \varphi_t(\mathbf{x}) = 0\}. \quad (2.13)$$

In practice, we define φ_t as the signed distance function from the immersed surface Γ_t itself [101]. First, a smooth Dirac function to approximate the “Dirac distribution” δ_{Γ_t} is

defined, rigorously, the codimension-1 Hausdorff measure [69] with support on the surface Γ_t , as follows:

$$\delta_{t,\varepsilon}(\mathbf{x}) = \begin{cases} \frac{1 + \cos(\pi\varphi_t(\mathbf{x})/\varepsilon)}{2\varepsilon} & \text{if } |\varphi_t(\mathbf{x})| \leq \varepsilon, \\ 0 & \text{if } |\varphi_t(\mathbf{x})| > \varepsilon, \end{cases} \quad (2.14)$$

In this way, there holds $\int_{-\infty}^{+\infty} \delta_{t,\varepsilon}(\varphi) d\varphi \equiv \int_{-\varepsilon}^{+\varepsilon} \delta_{t,\varepsilon}(\varphi) d\varphi = 1$ is obtained. Then, given a fixed domain $\Omega \subset \mathbb{R}^3$ and an immersed surface Γ , following the idea of the RIS method [14, 51] the RIIS model consists in enriching the Navier-Stokes equations, as presented in Section 2.1.1, with a penalization term in the momentum conservation equation with support the immersed surface Γ . The RIIS formulation for an incompressible homogeneous fluid reads:

Find the velocity \mathbf{u} and the pressure p such that:

$$\begin{cases} \rho \frac{\partial \mathbf{u}}{\partial t} - \nabla \cdot \sigma + \rho(\mathbf{u} \cdot \nabla) \mathbf{u} \\ \quad + \nabla p + \delta_{t,\varepsilon} \mathbf{R}_{\Gamma,\varepsilon} (\mathbf{u} - \mathbf{u}_\Gamma) = \mathbf{f} & \text{in } \Omega \times (0, T), \\ \nabla \cdot \mathbf{u} = 0 & \text{in } \Omega \times (0, T), \\ \mathbf{u} = \mathbf{g} & \text{on } \Gamma_D \times (0, T), \\ \sigma \mathbf{n} = \mathbf{h} & \text{on } \Gamma_N \times (0, T), \\ \mathbf{u}(\mathbf{x}, 0) = \mathbf{u}_0(\mathbf{x}) & \text{in } \Omega \times \{0\}. \end{cases} \quad (2.15)$$

$\mathbf{R}_{\Gamma,\varepsilon}$ was introduced in [51] to model fixed porous interfaces (for which $\mathbf{u}_\Gamma = \mathbf{0}$), e.g., medical stent devices, while in [14] the same method is used to model impermeable fixed surfaces (e.g., a fully open and fully closed aortic valve), for which $\mathbf{R}_\Gamma = R_\Gamma \mathbf{I}$ with the real-valued function R_Γ chosen sufficiently large to weakly enforce the fluid velocity \mathbf{u} to be small or nearly zero in proximity of the surface Γ . In [49], the latter case is generalized for a moving immersed surface (i.e., $\mathbf{u}_\Gamma \neq \mathbf{0}$). If suitable scalings with respect to the discretization parameters are introduced, this method can be interpreted as a penalty-based imposition of the no-slip condition on the immersed surface Γ . For this reason, in [49], $\mathbf{R}_{\Gamma,\varepsilon} = (R/\varepsilon) \mathbf{I}$ was chosen. In such way, $R/\varepsilon \rightarrow \infty$ for $\varepsilon \rightarrow 0$ so that $\mathbf{u}|_\Gamma \rightarrow \mathbf{u}_\Gamma$. It should be mentioned that the smoothing parameter ε is the same length scale of Equation (2.15) used to weakly enforce the velocity \mathbf{u} to adhere to \mathbf{u}_Γ on Γ through the resistive approach, and it corresponds to half thickness of the moving domain. Moreover, a smooth approximation of the Dirac function $\delta_{t,\varepsilon}$ defined in Equation (2.14) with a support across multiple mesh elements helps to have an effective resistive term, which guarantees no (or at least acceptable) flow penetration through the leaflets, as

stated in [49]. Since $\delta_{t,\varepsilon}$ has a 2ε width support, [49] suggests setting the value of ε at least 1.5 times the average size of the mesh in the valvular region. We work in the same functional setting of Section 2.1.2-2.2.1. We introduce two additional bilinear forms: $a_{\Gamma_t} : V \times V \rightarrow \mathbb{R}$, $a : V \times V \times \mathbb{R} \rightarrow \mathbb{R}$:

$$\begin{aligned} a_{\Gamma_t}(\mathbf{u}, \mathbf{v}) &:= \frac{R}{\varepsilon} \int_{\Omega} \delta_{t,\varepsilon}(\mathbf{u} - \mathbf{u}_{\Gamma}) \cdot \mathbf{v} d\Omega, \\ a(\mathbf{u}, \mathbf{v}, \mu) &:= \tilde{a}(\mathbf{u}, \mathbf{v}, \mu) + a_{\Gamma_t}(\mathbf{u}, \mathbf{v}). \end{aligned} \quad (2.16)$$

Then, for all $v \in V$; the method can be easily generalized to the case of N immersed surfaces Γ_i by introducing the bilinear form

$a_{\Gamma_t,N}(\mathbf{u}, \mathbf{v}) = \sum_{i=1}^N R_{\Gamma_{t,i}}/\varepsilon_i \int_{\Omega} \delta_{t,i,\varepsilon}(\mathbf{u} - \mathbf{u}_{\Gamma_i}) \cdot \mathbf{v} d\Omega$, for some $\{\varepsilon_i\}_{i=1}^N$. Finally, the weak formulation of Equation (2.15) reads as follows:

Find $\mathbf{u} \in L^2(\mathbb{R}^+; V) \cap C^0(\mathbb{R}^+; [L^2(\Omega)]^3)$ and $p \in L^2(\mathbb{R}^+; Q)$ such that, for all $v \in V_0$ and $q \in Q$:

$$\left\{ \begin{array}{l} \left(\rho \frac{\partial \mathbf{u}}{\partial t}, \mathbf{v} \right) + a(\mathbf{u}, \mathbf{v}, \mu) \\ + c(\mathbf{u}, \mathbf{u}, \mathbf{v}) + b(\mathbf{v}, p) = F(\mathbf{v}) \\ - b(\mathbf{u}, q) = 0. \end{array} \right. \quad (2.17)$$

2.3.2. Lumped parameter mechanical model including leaflets curvature

The RIIS model just presented is used to describe the blood flow through the aortic valve. In particular, the domain Ω is identified with the anatomic region composed of the aortic root, and the ascending aorta. In order to describe the configuration and the velocity of the valve, represented by φ_t and \mathbf{u}_{Γ} , a structural model is required for the deformation of the surface Γ_t . In this subsection, we present a reduced, lumped-parameters model that can realistically describe the main features of cardiac valve dynamics, presented in [56]. We remark that this approach is similar to the one used in [119], but in [56] additional geometrical information are included in the model.

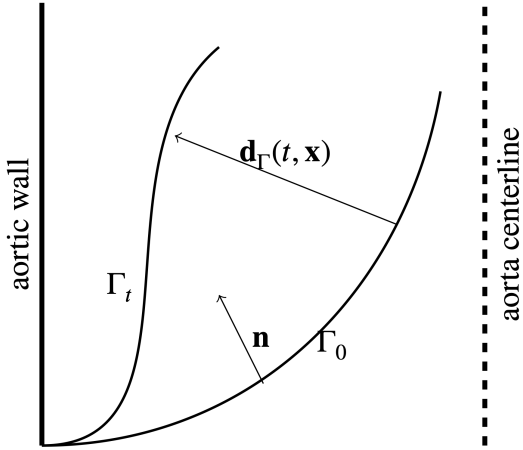


Figure 2.2: Schematic representation of \mathbf{d}_Γ and different configurations of the section of the leaflet; image taken from [56] Figure 1.

Denoting by $\mathbf{d}_\Gamma : [0, T] \times \hat{\Gamma} \rightarrow \mathbb{R}^3$ the displacement of the leaflet with respect to its reference configuration $\Gamma_0 = \hat{\Gamma}$, the current configuration Γ_t can be represented as

$$\Gamma_t = \left\{ \mathbf{x} \in \mathbb{R}^3 : \mathbf{x} = \mathbf{T}_t(\hat{\mathbf{x}}) = \hat{\mathbf{x}} + \mathbf{d}_\Gamma(t, \hat{\mathbf{x}}) \text{ for some } \hat{\mathbf{x}} \in \hat{\Gamma} \right\}, \quad (2.18)$$

as shown in Figure 2.2. We assume that, for each time t , every point $\mathbf{x} \in \Gamma_t$ of the leaflet is subject to an external force $\mathbf{f}(t, \mathbf{x})$ due to the surrounding fluid and to an elastic force related to the leaflet curvature $H(\mathbf{x})$. Both of these terms depend on the current configuration of Γ_t described by $\mathbf{d}_\Gamma(\mathbf{x})$. Moreover, we consider the valve motion to possibly be affected by some damping effect [56]. We assume that the elastic force in the valve depends on the leaflets curvature and acts only normally to the surface, in analogy to what happens in free-surface tension problem [24, 57]. We also assume the elastic force to vanish on $\hat{\Gamma}$, since it is generally observed that the resting state of the aortic valve is its closed configuration [56]. Subject to these assumptions, a local force balance can be formulated as follows:

$$\rho_\Gamma \ddot{\mathbf{x}} + \beta \rho_\Gamma \dot{\mathbf{x}} = \mathbf{f}(t, \mathbf{x}) - \gamma(H(\mathbf{x}) - \hat{H}(\hat{\mathbf{x}})) \mathbf{n}_\Gamma(\mathbf{x}), \quad (2.19)$$

where ρ_Γ is the surface density of the valve, β is a damping coefficient, γ is an elasticity coefficient, and \mathbf{n}_Γ is the normal to the surface Γ_t . The function $\hat{H}(\hat{\mathbf{x}})$ denotes the total curvature of the surface $\hat{\Gamma}$ in the position $\hat{\mathbf{x}} = \mathbf{T}_t^{-1}(\mathbf{x})$ corresponding to \mathbf{x} , that is the curvature of the resting configuration [56]. In order to reduce Equation (2.19) to a 0D

model, we assume that \mathbf{d}_Γ can be written as

$$\mathbf{d}_\Gamma(t, \hat{\mathbf{x}}) = c(t)\mathbf{g}(\hat{\mathbf{x}}). \quad (2.20)$$

The function $\mathbf{g} : \hat{\Gamma} \rightarrow \mathbb{R}^3$, representing the spatial dependence of the displacement, is assumed to be known, while the opening coefficient $c : [0, T] \rightarrow \mathbb{R}$ has to be modeled. With these assumptions, the local balance given by Equation (2.19) can be rewritten as follows [56]:

$$(\ddot{c}(t) + \beta\dot{c}(t))\rho_\Gamma \mathbf{g}(\mathbf{T}_t^{-1}(\mathbf{x})) = \mathbf{f}(t, \mathbf{x}) - \gamma \left(H(\mathbf{x}) - \hat{H}(\mathbf{T}_t^{-1}(\mathbf{x})) \right) \mathbf{n}_\Gamma(\mathbf{x}). \quad (2.21)$$

Finally, taking the component along $\mathbf{n}_\Gamma(\mathbf{x})$ and integrating over Γ_t , the following ordinary differential equation for c is obtained:

$$\begin{aligned} \ddot{c} + \beta\dot{c} + \eta(c, \mathbf{f}) &= 0, \quad \text{where} \\ \eta(c(t), \mathbf{f}(t)) &= \frac{\gamma \int_{\Gamma_t} \left(H(\mathbf{x}) - \hat{H}(\mathbf{T}_t^{-1}(\mathbf{x})) \right) d\mathbf{x} - \int_{\Gamma_t} \mathbf{f}(t, \mathbf{x}) \cdot \mathbf{n}_\Gamma(\mathbf{x}) d\mathbf{x}}{\int_{\Gamma_t} \rho_\Gamma \mathbf{g}(\mathbf{T}_t^{-1}(\mathbf{x})) \cdot \mathbf{n}_\Gamma(\mathbf{x}) d\mathbf{x}}. \end{aligned} \quad (2.22)$$

We point out that the dependence of η on c is implicit, via its dependence on the curvature H . Indeed, as will be better shown in Section 2.3.3, H is defined as $H = -\operatorname{div}_\Gamma \mathbf{n}_\Gamma$ and the normal vector \mathbf{n}_Γ can be computed in terms of the derivatives of the function $\mathbf{T}_t(\hat{\mathbf{x}}) = \hat{\mathbf{x}} + c(t)\mathbf{g}(\hat{\mathbf{x}})$ [56].

2.3.3. Coupling between fluid and structure

In this subsection, we perform the coupling of the 3D fluid model described in Section 2.3.1 and the 0D valve model presented in Section 2.3.2 in order to obtain a reduced FSI model: the fluid-to-valve stress \mathbf{f} that appears in Equation (2.22) is computed from the fluid model, while the 0D model provides the valve position and velocity as done in [56]. First, we introduce some notations related to the representation of the immersed surface Γ_t . Since φ_t is a signed distance function, the domain Ω can be partitioned into two open sets:

$$\Omega_t^+ = \{\mathbf{x} \in \Omega : \varphi_t(\mathbf{x}) > 0\}, \quad \Omega_t^- = \{\mathbf{x} \in \Omega : \varphi_t(\mathbf{x}) < 0\}. \quad (2.23)$$

For any function f defined over Ω , we define $f^\pm = f|_{\Omega^\pm}$. From the definition of, φ_t it is possible to define $\tilde{\mathbf{n}}_\Gamma$ and \tilde{H} . They are, respectively, the extensions to the whole domain

Ω of the surface normal \mathbf{n}_Γ and its curvature H ,

$$\begin{aligned}\tilde{\mathbf{n}}_\Gamma &= \frac{\nabla \varphi_t}{|\nabla \varphi_t|}, \\ \tilde{H} &= -\operatorname{div} \tilde{\mathbf{n}}_\Gamma = -\frac{\Delta \varphi_t}{|\nabla \varphi_t|} + \frac{\nabla^2 \varphi_t : (\nabla \varphi_t \otimes \nabla \varphi_t)}{|\nabla \varphi_t|^3}\end{aligned}\quad (2.24)$$

with $\nabla^2 \varphi_t$ denoting the Hessian matrix of φ_t . The quantities $\tilde{\mathbf{n}}_\Gamma$ and \tilde{H} represent the extensions of the normal vector and curvature, indeed $\tilde{\mathbf{n}}_\Gamma|_\Gamma = \mathbf{n}_\Gamma$, $\tilde{H}|_\Gamma = H$. For details on these functional theory extensions, the reader can refer to [40]. We remark that $\tilde{\mathbf{n}}_\Gamma$ does not change direction across Γ_t . Based on Equation (2.20), we define the surface velocity \mathbf{u}_Γ as:

$$\mathbf{u}_\Gamma(t, \mathbf{x}) = \dot{c}(t) \tilde{\mathbf{g}}(\mathbf{x}), \quad (2.25)$$

where $\tilde{\mathbf{g}} : \Omega \rightarrow \mathbb{R}^3$ is the closest-point extension of $\mathbf{g} : \hat{\Gamma} \rightarrow \mathbb{R}^3$. Regarding the forces exerted by the fluid on the valve, referring e.g. to [27], they are related to the stress jump across Γ_t :

$$\mathbf{f} = [\sigma \mathbf{n}_\Gamma]|_{\Gamma_t} = \sigma^+|_{\Gamma_t} \mathbf{n}_\Gamma - \sigma^-|_{\Gamma_t} \mathbf{n}_\Gamma. \quad (2.26)$$

Using the smooth Dirac delta $\delta_{\Gamma,\varepsilon}$ introduced in Equation (2.14) and the definitions provided by Equation (2.26), the integral term related to \mathbf{f} that appears in Equation (2.22) can be approximated as:

$$\int_{\Gamma_t} \mathbf{f} \cdot \mathbf{n}_\Gamma \simeq \int_{\Omega} (\sigma \tilde{\mathbf{n}}_\Gamma \cdot \tilde{\mathbf{n}}_\Gamma \delta_{\Gamma,\varepsilon}^+ - \sigma \tilde{\mathbf{n}}_\Gamma \cdot \tilde{\mathbf{n}}_\Gamma \delta_{\Gamma,\varepsilon}^-). \quad (2.27)$$

Proceeding in the same way, the other integrals appearing in Equation (2.22) can be approximated as:

$$\begin{aligned}\int_{\Gamma_t} \rho_\Gamma (\mathbf{g} \circ \mathbf{T}_t^{-1}) \cdot \mathbf{n}_\Gamma &\simeq \int_{\Omega} \rho_\Gamma (\mathbf{g} \circ \mathbf{T}_t^{-1}) \cdot \tilde{\mathbf{n}}_\Gamma \delta_{\Gamma,\varepsilon}, \\ -\gamma \int_{\Gamma_t} (H - \hat{H} \circ \mathbf{T}_t^{-1}) &\simeq -\gamma \int_{\Omega} (\tilde{H} - \hat{\tilde{H}}) \delta_{\Gamma,\varepsilon},\end{aligned}\quad (2.28)$$

with $\hat{\tilde{H}}$ denoting the RIIS representation of the pulled-back curvature $\hat{H} \circ \mathbf{T}_t^{-1}$.

2.4. Numerical methods

In this section, we present the space and time discretization of the coupled 3D-0D FSI model, in the non-Newtonian case. The Newtonian case is a particular case of the formu-

lation that is presented, in which the viscosity is a constant parameter. This procedure is described following [49, 56] for the space-time discretization, with the original introduction of the non-linearity introduced by the non-Newtonian model.

2.4.1. Time and space discretizations

We define a set of times $\{t_k\}_{k=0}^N$ such that $0 = t_0 < t_1 < \dots < t_N = T$ and $t_{k+1} - t_k = \Delta t \forall k \geq 0$, and, for a generic function of space and time $v(\mathbf{x}, \mathbf{t})$, we introduce $v^n(\mathbf{x}) := v(\mathbf{x}, t_n) \forall n \in \{0, 1, \dots, N\}$. Regarding the space discretization, we introduce a tetrahedral mesh \mathcal{T}_h of Ω , and denote by \mathbb{Q}^r the space of polynomials of degree r with respect to every coordinate in space. We introduce the corresponding finite element space:

$$X_h^r = \{v_h \in C^0(\bar{\Omega}) : v_h|_K \in \mathbb{Q}^r(K), \forall K \in \mathcal{T}_h\} . \quad (2.29)$$

Following this procedure, the definition of the discrete spaces for pressure and velocity is $V_h^r = \{\mathbf{v}_h \in [X_h^r]^3 : \mathbf{v}_h = \mathbf{0} \text{ on } \Gamma_D\}$ and $Q_h^r = X_h^r$. For more information on this procedure, the reader can refer to [111]. Regarding the numerical approximation of the Navier-Stokes-RIIS problem of Equation (2.15), a semi-implicit BDF-FE scheme of order s is used as in [49]. The same polynomial degree r for both V_h^r and Q_h^r is used: this in order to limit the computational time induced by the space discretization. However, if we consider the same polynomial degree for the discretized spaces of velocity and pressure the *inf-sup condition* is not satisfied [111]. This issue is overcome in [49, 56] by extending SUPG-PSPG stabilization method [129] to the RIIS problem. This procedure allows obtaining an inf-sup stable formulation and controlling numerical instabilities associated with the highly advective flow regime in the valve [49]. Moreover, as proposed in [55] for the time discretization based on the BDF scheme, the SUPG-PSPG parameters are set following the variational multiscale (VMS) concept introduced in [15]. Finally, for what concerns the non-linearity introduced in the viscosity term by the non-Newtonian model, a semi-implicit treatment is adopted as in [64]. The complete numerical method for the RIIS problem is the following:

Given $\mathbf{u}_h^n, n = 0, \dots, s-1$, for each $n = s, \dots, N$, find \mathbf{u}_h^n, p_h^n such that

$$\begin{aligned} & \left(\rho \frac{\alpha_s \mathbf{u}_h^n - \mathbf{u}_h^{n,BDFs}}{\Delta t}, \mathbf{v}_h \right) + a^n \left(\mathbf{u}_h^n, \mathbf{v}_h, \mu \left(\mathbf{u}_h^{n,BDFs} \right) \right) \\ & + c \left(\mathbf{u}_h^{n,s}, \mathbf{u}_h^n, \mathbf{v}_h \right) + b \left(\mathbf{v}_h, p_h^n \right) - b \left(\mathbf{u}_h^n, q_h \right) \\ & + \sum_{K \in \mathcal{T}_h} \left(\tau_M^{n,s} \mathbf{r}_M^n \left(\mathbf{u}_h^n, p_h^n, \mu \left(\mathbf{u}_h^{n,BDFs} \right) \right), \rho \mathbf{u}_h^{n,s} \cdot \nabla \mathbf{v}_h + \nabla q_h \right)_K \\ & + \sum_{K \in \mathcal{T}_h} \left(\tau_C^{n,s} r_C^n \left(\mathbf{u}_h^n \right), \nabla \cdot \mathbf{v}_h \right)_K = F \left(\mathbf{v}_h \right) \end{aligned} \quad (2.30)$$

for all $\mathbf{v}_h \in V_h$ and $q_h \in Q_h$, where $(\cdot, \cdot)_K$ is the L^2 inner product over a mesh element K and

$$\begin{aligned} a^n(\mathbf{u}, \mathbf{v}, \mu) &= \mathcal{D}(\mathbf{u}, \mathbf{v}, \mu) + \left(\frac{R}{\varepsilon} \mathbf{u} \delta_\varepsilon^n, \mathbf{v} \right) \\ b(\mathbf{v}, q) &= -(\operatorname{div} \mathbf{v}, q) \\ c(\mathbf{w}, \mathbf{u}, \mathbf{v}) &= (\mathbf{w} \cdot \nabla \mathbf{u}, \mathbf{v}) \\ F(\mathbf{v}) &= \int_{\Omega} \mathbf{f} \cdot \mathbf{v} d\Omega + \int_{\partial \Omega_N} \mathbf{h} \cdot \mathbf{v} d\gamma - \left(\frac{R}{\varepsilon} \mathbf{u}_{\Gamma,h} \delta_\varepsilon^n, \mathbf{v} \right). \end{aligned} \quad (2.31)$$

The BDF parameter α_s and the velocities $\mathbf{u}_h^{n,BDFs}, \mathbf{u}_h^{n,s}$ depend on the order s of the BDF scheme [55], while $\mathbf{r}_M^n, r_C^n, \tau_M^{n,s}, \tau_C^{n,s}$ are the functionals associated with the SUPG-PSPG stabilization, defined as:

$$\begin{aligned} \mathbf{r}_M^n \left(\mathbf{u}_h^n, p_h^n, \mu \left(\mathbf{u}_h^{n,BDFs} \right) \right) &= \rho \frac{\alpha_s \mathbf{u}_h^n - \mathbf{u}_h^{n,BDFs}}{\Delta t} - \mu \left(\mathbf{u}_h^{n,BDFs} \right) \Delta \mathbf{u}_h^n \\ &+ \rho \mathbf{u}_h^{n,s} \cdot \nabla \mathbf{u}_h^n + \nabla p_h^n + \frac{R}{\varepsilon} \delta_\varepsilon^n (\mathbf{u}_h^n - \mathbf{u}_\Gamma^n) \\ r_C^n(\mathbf{u}_h^n) &= \nabla \cdot \mathbf{u}_h^n \\ \tau_C^{n,s} &= (\tau_M^{n,s} \mathfrak{g} \cdot \mathfrak{g})^{-1} \\ \tau_M^{n,s} &= \frac{1}{\sqrt{\frac{\rho^2 \alpha_s^2}{\Delta t^2} + \rho^2 \mathbf{u}_h^{n,s} \cdot \mathfrak{G} \mathbf{u}_h^{n,s} + C_r \mu^2 \mathfrak{G} : \mathfrak{G} + \frac{R^2}{\varepsilon^2} (\delta_\varepsilon^n)^2}}. \end{aligned} \quad (2.32)$$

The quantities \mathfrak{G} and \mathfrak{g} are metric tensor and vector, and they depend on the element map $\mathbf{M}_K : \hat{K} \rightarrow K$, for $K \in \mathcal{T}_h$, which maps the reference element \hat{K} to the current one K [129]. It should be noticed that the difference between Equation (2.30) and the numerical approximation provided by [56] is the dependency on the variable $\mu \left(\mathbf{u}_h^{n,BDFs} \right)$ introduced by the non-Newtonian model. This last term is calculated through the Carreau formula shown in Equation (2.10). In particular, the shear rate needed in the Carreau formula is computed starting from $\mathbf{u}_h^{n,BDFs}$. Concerning the variables that characterize the geometry

of the valve, a FE description is used. The discrete signed distance function is $\varphi_h^n \in X_h^{r'}$, with a polynomial degree $r' \geq 2$ that can differ from r [56]. Accordingly, the extended normal and curvature field can be written in terms of the basis functions $\{\psi_\ell\}_{\ell=1}^{N'_h}$ of $X_h^{r'}$, starting from the latter the leaflet's extended normal and curvature can be defined, as in [56], as:

$$\begin{aligned}\tilde{\mathbf{n}}_{\Gamma,h}^n &= \frac{\sum_{\ell=1}^{N'_h} \varphi_\ell^n \nabla \psi_\ell}{\left| \sum_{\ell=1}^{N'_h} \varphi_\ell^n \nabla \psi_\ell \right|}, \\ \tilde{H}_{\Gamma,h}^n &= -\operatorname{div} \tilde{\mathbf{n}}_{\Gamma,h}^n \\ &= -\frac{\sum_{\ell=1}^{N'_h} \varphi_\ell^n \Delta \psi_\ell}{\left| \sum_{\ell=1}^{N'_h} \varphi_\ell^n \nabla \psi_\ell \right|} + \frac{\sum_{\ell,m,k=1}^{N'_h} \varphi_\ell^n \varphi_m^n \varphi_k^n \nabla^2 \psi_\ell : (\nabla \psi_m \otimes \nabla \psi_k)}{\left| \sum_{\ell=1}^{N'_h} \varphi_\ell^n \nabla \psi_\ell \right|^3}\end{aligned}\quad (2.33)$$

It should be remarked that these last two quantities can be used directly as in expressions appearing in Equations (2.33), without any projections onto a finite element space, since they appear in the 0D models only as integrands of Equations (2.27)-(2.28). Instead, to represent the valve's kinematics, the discrete leaflets' velocity is computed from a first-order approximation of Equation (2.20) in such way:

$$\mathbf{u}_{\Gamma,h}^n = \frac{c^n - c^{n-1}}{\Delta t} \tilde{\mathbf{g}}_h^n \quad \forall n \in \{s, \dots, N\}. \quad (2.34)$$

For the solution of the Ordinary Differential Equation expressed in Equation (2.21), we adopt an explicit Runge-Kutta method of the fourth order [127]. The fluid and structure models are loosely coupled at each time-step [56]:

Algorithm 2.1 Numerical solution scheme for the non-Newtonian 3D-0D-FSI model

- 1: Given $\mathbf{u}_h^n, p_h^n, c^n$ for $n = 0, \dots, s - 1$, and compute the functions $\varphi^n, \tilde{\mathbf{n}}_\Gamma^n, \tilde{\mathbf{H}}^n$ that corresponds to the surface Γ^n and $\mu(\mathbf{u}_h^{n,BDFs})$, for $n = 0, \dots, s - 1$,
 - 2: **for** $n \leftarrow s$ **do**
 - 3: Compute the integrals appearing in Equation (2.22), in terms of $\mathbf{u}_h^{n-1}, p_h^{n-1}, \Gamma^{n-1}, \varphi^{n-1}$.
 - 4: Find c^n by solving the 0D Equation (2.22) with a step of RK4.
 - 5: Move the valve to its next configuration Γ^n described by $\mathbf{d}_\Gamma^n = c^n \mathbf{g}$ and compute $\mathbf{u}_\Gamma^n = \frac{c^n - c^{n-1}}{\Delta t} \tilde{\mathbf{g}}$.
 - 6: Compute the next distance function φ^n with respect to Γ^n and assemble fields related to the normal and the curvature $\tilde{\mathbf{n}}_\Gamma^n$ and $\tilde{\mathbf{H}}^n$.
 - 7: Find $(\mathbf{u}_h^n, p_h^n) \in V_h^r \times Q_h^r$ by solving the linear problem represented in Equation (2.30)
 - 8: **end for**
-

Starting from the numerical approximation of Equation (2.30), the algebraic formulation of the problem can be obtained in a standard way: for more details on this procedure, the reader can refer to [41, 111]. It should be mentioned that, as it is commonly needed in fluid dynamics problems, a suitable preconditioner must be employed in order to obtain a solution efficiently. For the simulations performed for this thesis, the SIMPLE preconditioner was employed [41].

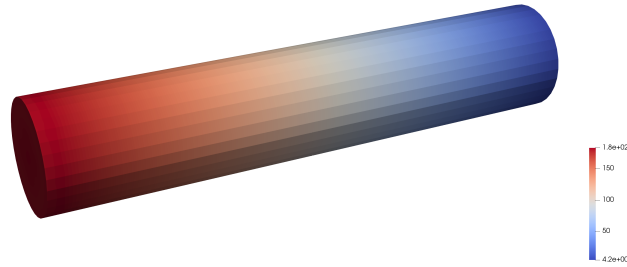
3 | Validation of the non-Newtonian model in a cylindrical domain

In this chapter, the firsts numerical results, obtained using the model presented in Section 2.1 and Section 2.2, are presented. All the simulations that can be found in this thesis were performed using `lifex` [5]: a high-performance library for the solution of multi-physics and multiscale problems, mainly for cardiac applications [9]. This library is written in C++ using the most modern programming techniques available in the C++17 standard, and it is based on the deal.II finite element core [4]. As part of the thesis work, the non-Newtonian model was implemented on top of the previously existing Navier-Stokes solver. In this chapter, the validation of the standalone non-Newtonian model (considering only the computational fluid dynamics part of the problem, without taking into account the FSI model) is presented. In particular, to validate the model implementation, some results obtained using Newtonian and non-Newtonian rheology of blood are compared with the ones obtained in [128], where the same problem is solved in the same domain but using a different method. The model was tested on a simple geometry: a cylindrical domain, which can be considered as a first approximation of a vessel. Results obtained using a Newtonian rheology with the ones obtained by using the Carreau model for the non-Newtonian viscosity are compared. Then, in order to properly validate the model implementation, the results are compared with [128], where the same problem is solved in a cylindrical domain but using a semi-analytical approach based on Poiseuille theory [27] for the stationary case and Womersley theory for the pulsatile case [141]. The differences produced by the two rheological models are investigated, obtaining results in accordance with the ones reported in [128].

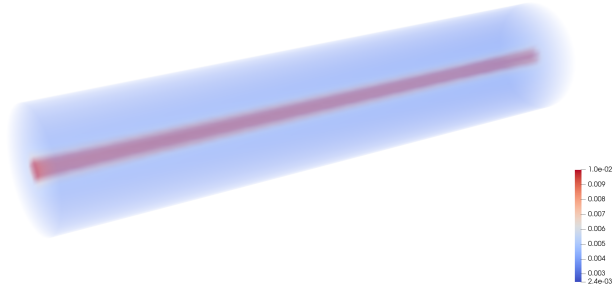
The simulations shown in this chapter were executed on 2 cores running *MacBook Air (M1, 2020), 2 cores, 16GB of RAM.*

3.1. Steady case

To assess the effectiveness of the Carreau model, the results obtained imposing a steady-state flow were first compared. In particular, two cylindrical domains with two different radii equal to $R_1 = 0.0031\text{ m}$ and $R_2 = 0.0045\text{ m}$ respectively, were considered, and in both cases the length of the cylinder was set equal to 10 times the radius as in [128]. The density of blood was set equal to $\rho = 1060\text{ kg/m}^3$ and the viscosity for the Newtonian model equal to $\mu_{\text{newtonian}} = 0.00345\text{ Pa}\cdot\text{s}$. The space discretization was performed by means of hexahedral finite elements of order 1 with SUPG-PSPG stabilization, while the time derivatives are approximated through a BDF1 scheme. A Dirichlet boundary condition on the inlet section and a Neumann homogeneous boundary condition on the outlet section were imposed, resulting in a constant pressure drop equal to 6000 Pa/m (Figure 3.1 (a)).



(a) Pressure distribution in the cylinder.



(b) Viscosity distribution in the cylinder.

Figure 3.1: Pressure and viscosity distribution in the domain for the steady case.

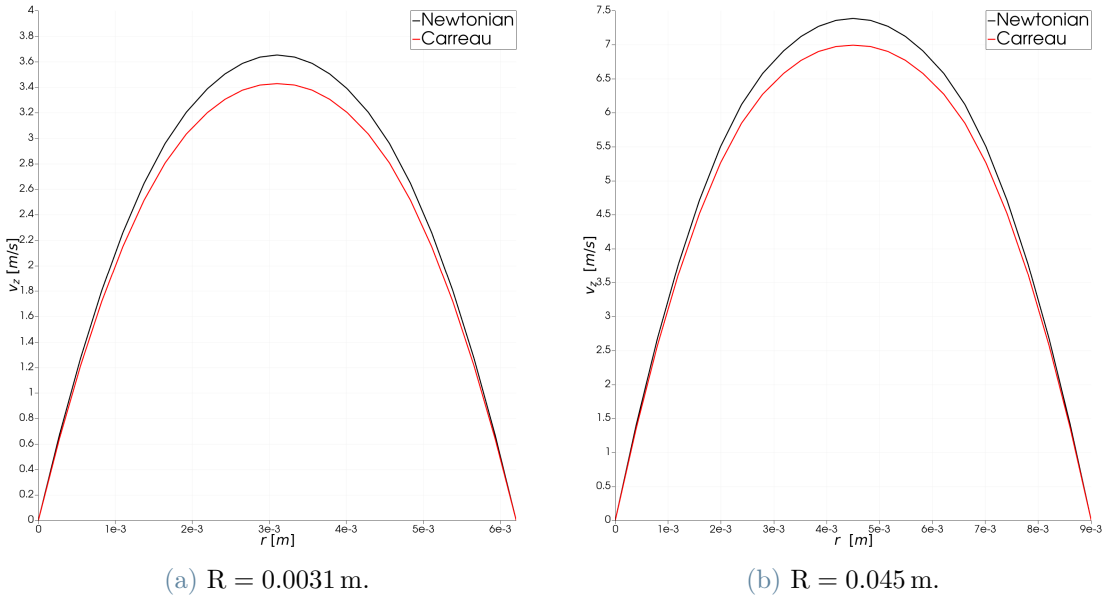


Figure 3.2: Velocity profiles for the steady case in a cylinder domain.

In Figure 3.2 the velocity profiles associated with the Newtonian and non-Newtonian models in both cylinders are shown. The 2D representation of the velocity profiles exploits the radial symmetry. As could be expected, the resulting flow is parabolic (Poiseuille flow, as theoretically predicted in [27]) and it can be observed that the non-Newtonian flow, which in general yields to higher viscosity than the Newtonian one, is characterized by a lower flow rate. The details of the experiments such as flux and wall shear stress ($\text{WSS} = \mu \frac{\partial u_r}{\partial r}|_{r=R}$) are reported in Tables 3.1-3.2, where “Ratio flux” is computed as $(\text{Newtonian flux} - \text{Carreau flux}) / (\text{Newtonian flux})$. The differences in the absolute values of the fluxes with respect to the reference results can be caused by many reasons, including the different approaches adopted to obtain the results, however it is important to notice that the difference between Newtonian and non-Newtonian flows, together with the values of the WSS, are in complete accordance with the reference results. Finally, Figure 3.2 (b) shows the value of the viscosity in the volume of the domain: the maximum is reached in the center, where the velocity gradient is at its minimum value, and the minimum is reached near the boundary, where the velocity gradient is at its maximum value. Thus, the result is coherent with what was mentioned in Section 2.2.1.

	Reference	life ^x
Newtonian flux (m ³ /s)	$6.30 \cdot 10^{-5}$	$5.72 \cdot 10^{-5}$
Carreau flux (m ³ /s)	$5.98 \cdot 10^{-5}$	$5.43 \cdot 10^{-5}$
Ratio flux	5.08%	5.03%
Newtonian WSS (Pa)	9.3	9.31
Carreau WSS (Pa)	9.3	9.26

Table 3.1: Comparison with the reference results [128] for R = 0.0031 m.

	Reference	life ^x
Newtonian flux (m ³ /s)	$2.80 \cdot 10^{-5}$	$2.49 \cdot 10^{-5}$
Carreau flux (m ³ /s)	$2.69 \cdot 10^{-5}$	$2.38 \cdot 10^{-5}$
Ratio flux	4.04%	4.30%
Newtonian WSS (Pa)	13.5	13.91
Carreau WSS (Pa)	13.5	13.87

Table 3.2: Comparison with the reference results [128] for R = 0.0045 m.

3.2. Pulsatile case

The second validation was performed, solving a similar problem as in Section 3.1, but imposing a pulsatile pressure gradient. In particular, the amplitude of the oscillatory pressure gradient was taken to be equal to $A = 6000$ Pa/m (corresponding to 45 mmHg) while the angular frequency was taken as $n = 2\pi f$ with $f = 1.2$ Hz (corresponding to the average pulse frequency of 72 beats per minute).

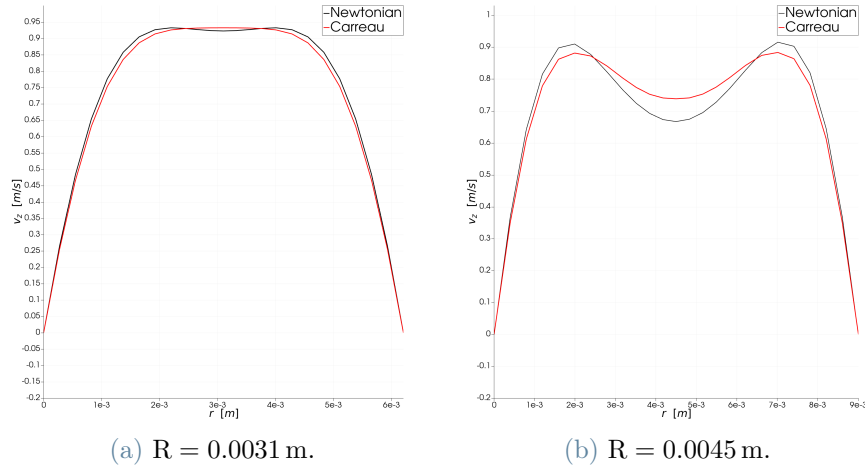


Figure 3.3: Velocity profiles corresponding to the maximum flow rate for the pulsatile case in a cylinder domain.

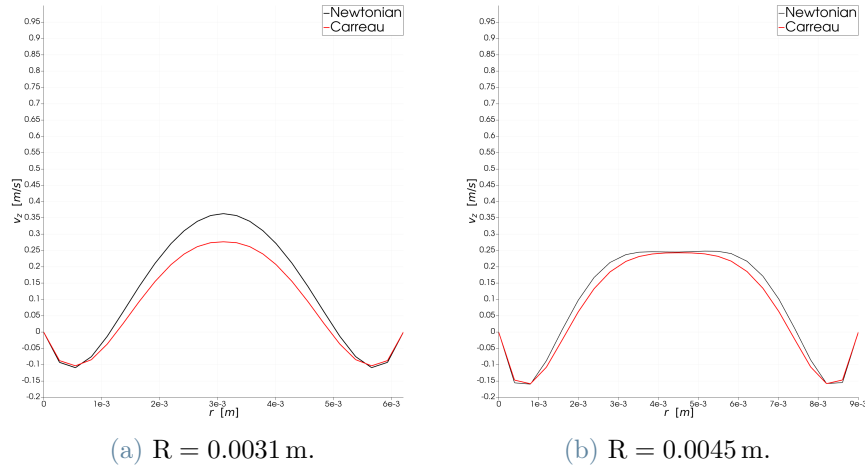


Figure 3.4: Velocity profiles corresponding to the minimum flow rate for the pulsatile case in a cylinder domain.

Figure 3.3 shows the velocity profiles obtained as solutions of the Newtonian and non-Newtonian models, at the time of the maximum value of the flow rate. We can observe the typical shape of the Womersley profile [18, 141] in the cylinder with radius $R = 0.0045 \text{ m}$, while for the smaller radius $R = 0.0031 \text{ m}$ we can see a sort of transition to a parabolic profile. The two models mainly differ in the central region of the cylinder, and the difference becomes more evident as the radius decreases. It is also interesting to compare the velocity profiles associated to the minimum values of the flow rate (in the positive time cycle, i.e., the lowest positive value of the flow rate). These are reported in Figure 3.4. In

3| Validation of the non-Newtonian model in a cylindrical domain

in this picture we can notice that the non-Newtonian velocity profiles are slightly flattened with respect to the Newtonian profiles. Similar velocity profiles have been obtained in [73] for the 2D blood flow in the carotid artery using the Carreau-Yasuda model. These profiles, together with the ones shown in Figure 3.2 are in accordance with Figure 1-2-3 of [128].

	Reference	life ^x
Newtonian max flux (m^3/s)	$1.77 \cdot 10^{-5}$	$1.86 \cdot 10^{-5}$
Carreau max flux (m^3/s)	$1.73 \cdot 10^{-5}$	$1.81 \cdot 10^{-5}$

Table 3.3: Comparison of the max flow rate with the reference results [128] for $R = 0.0031 \text{ m}$.

	Reference	life ^x
Newtonian max flux (m^3/s)	$4.10 \cdot 10^{-5}$	$4.23 \cdot 10^{-5}$
Carreau max flux (m^3/s)	$4.06 \cdot 10^{-5}$	$4.14 \cdot 10^{-5}$

Table 3.4: Comparison of the max flow rate with the reference results [128] for $R = 0.0045 \text{ m}$.

Tables 3.3 and 3.4 summarize the comparison of the results obtained using the life^x solver against the ones reported in [128].

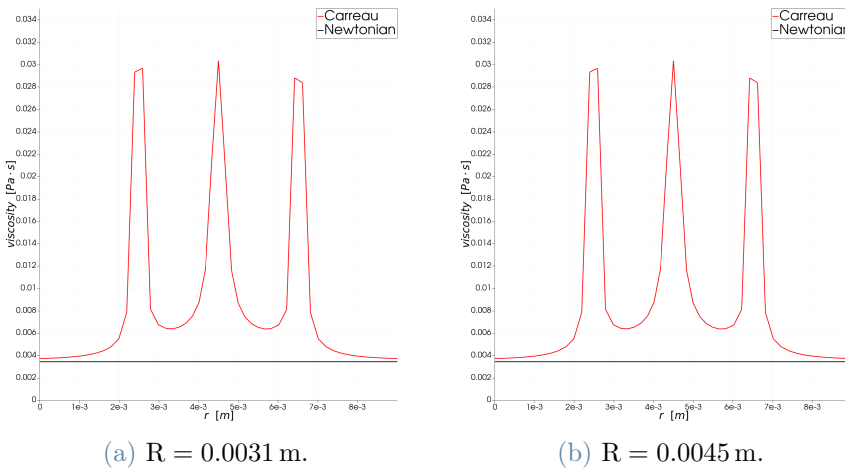


Figure 3.5: Comparison between the Newtonian and the non-Newtonian viscosity at the maximum flow rate.

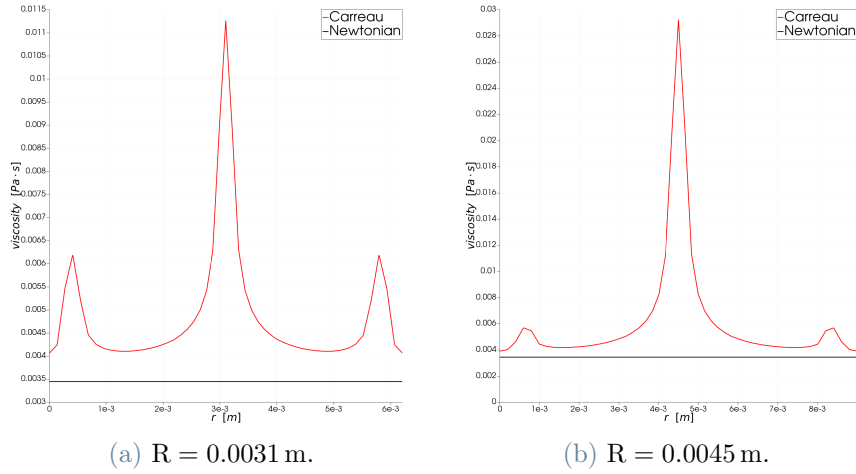


Figure 3.6: Comparison between the Newtonian and the non-Newtonian viscosity at the minimum flow rate.

The viscosity distribution in both cylinders for the maximum and minimum flow rates are shown in Figure 3.5 and Figure 3.6 respectively. The peaks in the central region correspond to the lower velocity gradients, while the satellite peaks in Figure 3.5 (b) and Figure 3.6 (b) are connected with the local minima of the velocity gradient presented in Figure 3.3 (b) and Figure 3.4 (a).

The fact that the results shown in this section are in accordance both with [128] and what can be theoretically expected in a cylinder (see Section 2.2.3) indicates that the results that will be presented in Section 4.4 (the subject of major interest of the thesis) can be trusted, especially for what concerns the differences that will be observed between Newtonian and non-Newtonian models.

4 | A simulation study on the aortic valve

In this chapter, we present numerical results in the proximity of the aortic valve obtained using the models explained in Chapter 2. All simulations were performed using life^x.

The results were obtained using the RIIS formulation coupled with the lumped parameter momentum balance 0D equation for the valve on a realistic domain in the proximity of the valve. We first introduce the setting of the simulation, comprehensive of the explanation of the domain, mesh generation, boundary conditions and baseline parameters that are used for all simulations. Then, we describe a simulation for a healthy valve, with particular attention to the dynamics of the valve, and the general behavior of the flow in the opening and closing phase, highlighting how the results obtained are in accordance with what is physiologically observed in a healthy valve and what can be improved to reproduce these observations even better. After this, we analyze two pathological cases, relative to a stenotic and regurgitating conditions, and compare them with the healthy configuration showing the main differences. Finally, we present a comparison between the results obtained using the Newtonian and non-Newtonian rheology in the two pathological configurations, highlighting similarities and differences that can be observed in the results.

The simulations shown in this chapter were all executed on 56 cores running *Intel Xeon Gold 6238@2.10 GHz*, using the computational resources available at MOX, Dipartimento di Matematica, Politecnico di Milano.

4.1. Setting for the simulations

In this section, we present the domain and mesh for our simulations, as well as the boundary conditions and parameters used in this chapter.

4.1.1. Mesh generation

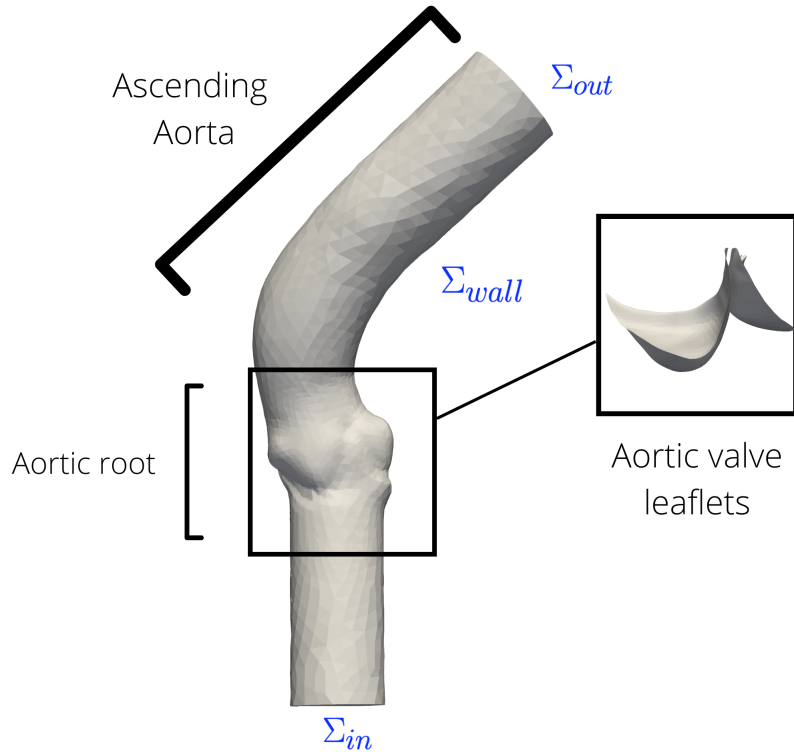


Figure 4.1: Aortic root domain with flow extension and closed valve leaflets.

Both the geometry of the domain Ω and of the closed valve leaflets $\hat{\Gamma}$ are taken from the Zygote Heart Model [2, 148], an accurate model of the physiological heart derived from CT-scan acquisitions. The aortic root and the closed configuration of the valve are shown in Figure 4.1 together with the aortic root's flow extension and the ascending aorta. The flow extension is the part of the domain that goes from the aortic root to Σ_{in} and is used to replace the left ventricle. This was done in order to simplify the geometry of the problem, and to facilitate the imposition of the boundary condition at the inlet, as in [56].

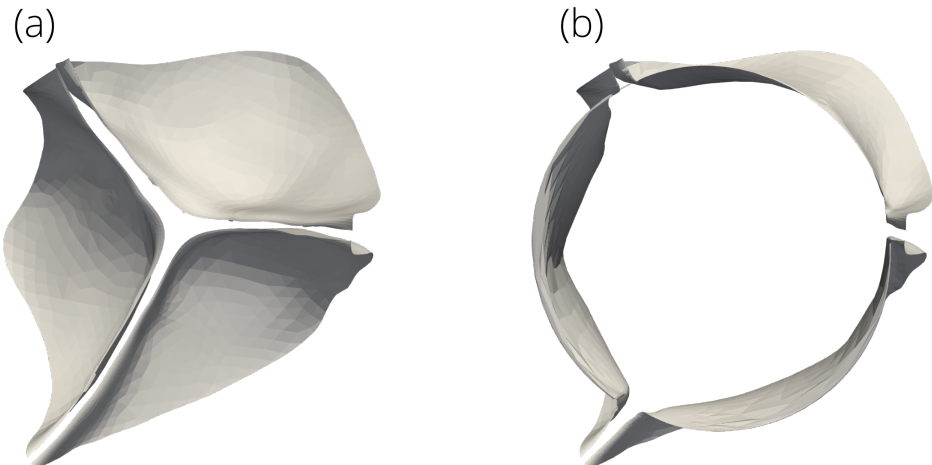


Figure 4.2: Closed (a) and open (b) configuration of the valve.

In the same way as [56] a proper opening field \mathbf{g} has been introduced on the leaflets, so that the surface $\Gamma_{\text{open}} = \{\mathbf{x} = \hat{\mathbf{x}} + \mathbf{g}(\hat{\mathbf{x}}), \hat{\mathbf{x}} \in \hat{\Gamma}\}$, corresponding to an opening coefficient $c = 1$, represents the physiological open valve configuration with an orifice area of 3.02 cm^2 (closed and open configuration are shown in Figure 4.2). This value is in the physiological range for healthy adults ($3.9 \pm 1.2 \text{ cm}^2$) [68].

The mesh that was used for the simulations was obtained, starting from the domain taken from Zygote [2, 148], through VMTK [1]: a collection of libraries and tools for 3D reconstruction, geometric analysis, mesh generation and surface data analysis for image-based modeling of cardiac domains. The mesh was generated tailored towards the application to the Navier-Stokes-RIIS model. As will be made clear in Section 4.1.2, the immersed surfaces are captured accurately provided the mesh is sufficiently fine in their region. Therefore, the mesh size is spatially dependent, with a higher resolution in the neighborhood of the valve. Moreover, a sufficiently fine mesh in the area corresponding to the aortic root should be used in order to better capture the complex behavior of the flow around that area. Contrarily, a coarser mesh is sufficient in the area located far from the aortic root, since we are mostly interested in the flow around the valve leaflets. To obtain a mesh with these characteristics for the size of the elements in different areas of the domain, different steps were performed:

- We computed a distance function from the position of the valve.
- We performed the generation of the new refined mesh using the formula:

$$h(x) = \max \{h_{\min}, \min \{\alpha f^\beta, h_{\max}\}\},$$
where h indicates the edge length we want to obtain, f is obtained using the distance function defined above, h_{\min} and h_{\max} denote the desired minimum and maximum mesh edge length, respectively, and α

and β are additional parameters. To obtain the mesh used in the simulations, we set $h_{min} = 0.0007$, $h_{max} = 0.004$, $\alpha = 3$ and $\beta = 4$.

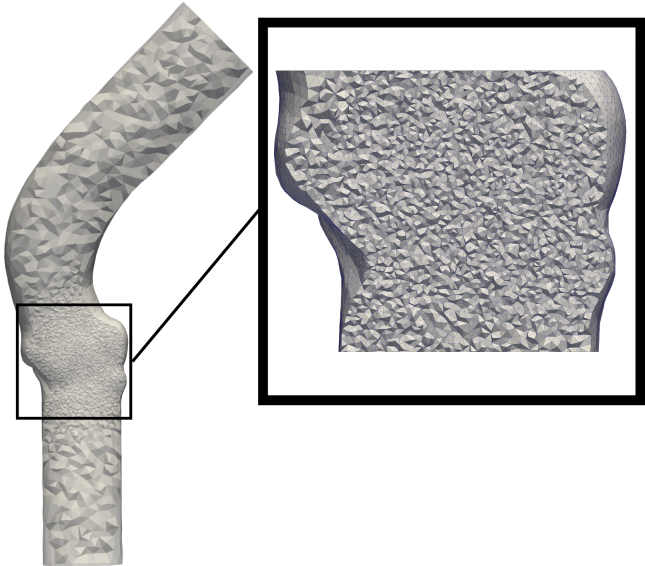


Figure 4.3: 3D tetrahedral mesh of the aortic root with zoom on the area close to the aortic valve.

A clip of the 3D mesh obtained can be seen in Figure 4.3: as we can see, the mesh is much more refined in the area close to the aortic valve. The mesh is tetrahedral and has about one million elements, including artificial flow extensions at both inlet and outlet. The element's size h ranges from 5.5 mm in the flow extensions to 0.34 mm in the aortic root.

Blood velocity and pressure are both discretized with \mathbb{P}^1 finite elements. Further information on the mesh elements' size and degrees of freedom (DOFs) in terms of space and pressure can be found in Table 4.1.

Number of cells	962 549	
DOFs	velocity	468 378
$\mathbb{P}1 - \mathbb{P}1$	pressure	156 126
	total	624 504
h_{\max}	$5.50 \cdot 10^{-3}$ m	
h_{\min}	$3.38 \cdot 10^{-4}$ m	
h_{mean}	$7.98 \cdot 10^{-4}$ m	

Table 4.1: Mesh size and number of degrees of freedom.



Figure 4.4: Control volumes location with respect to the leaflets.

Finally, Figure 4.4 shows the location of the two control volumes above and below the valve that are used to compute some postprocessing results that will be shown in the next sections. [49] highlighted that the numerical results computed in these two volumes are not significantly affected by their specific location, with the condition that their distance from the valve lays between 5 and 25 mm, and this is the case of our configuration.

4.1.2. Boundary conditions and baseline parameters

As boundary conditions, we impose time-dependent normal stress at both inlet and outlet, while we prescribe a no-slip condition on the wall. The resulting problem is:

$$\begin{cases} \rho \frac{\partial \mathbf{u}}{\partial t} - \nabla \cdot \sigma + \rho(\mathbf{u} \cdot \nabla) \mathbf{u} \\ + \nabla p + \delta_{t,\varepsilon} \frac{R}{\varepsilon} (\mathbf{u} - \mathbf{u}_\Gamma) = \mathbf{f} & \text{in } \Omega \times (t_0, T), \\ \nabla \cdot \mathbf{u} = 0 & \text{in } \Omega \times (t_0, T), \\ \mathbf{u} = \mathbf{0} & \text{on } \Sigma_{\text{wall}} \times (t_0, T), \\ \sigma \mathbf{n} = p_{\text{in}} \mathbf{n} & \text{on } \Sigma_{\text{in}} \times (t_0, T), \\ \sigma \mathbf{n} = p_{\text{out}} \mathbf{n} & \text{on } \Sigma_{\text{out}} \times (t_0, T), \\ \mathbf{u}(\mathbf{x}, 0) = \mathbf{u}_0(\mathbf{x}) & \text{in } \Omega \times \{t_0\} \end{cases} \quad (4.1)$$

where Σ_{in} and Σ_{out} represent respectively the inflow and outflow boundaries, while the boundary Σ_{wall} represents the aortic wall; these boundaries are shown in Figure 4.1.

$p_{\text{in}}(t)$ and $p_{\text{out}}(t)$ are the pressures obtained from the lumped circulation model presented in [113] after proper calibration in order to be consistent with physiological pressures as reported in Wiggers diagrams [140], using the same approach as [56].

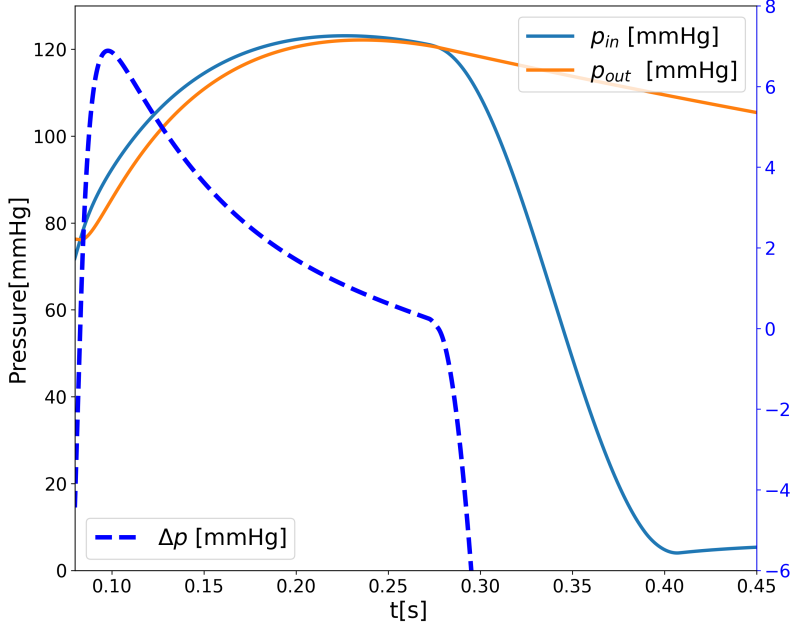


Figure 4.5: Physiological pressure boundary conditions.

These curves, together with the pressure difference between inlet and outlet, are shown

in Figure 4.5. The other values for the parameters that will be used for all simulations are reported in Table 4.2.

Parameter	Value	Description
ρ [Kg/m ³]	1060	Density of blood
μ_{new} [Pa · s]	$3.5 \cdot 10^{-3}$	Newtonian viscosity of blood
ε [m]	$5 \cdot 10^{-4}$	Half-thickness of the valve
R [Pa · s]	1000	Resistance parameter in the RIIS method
β [s ⁻¹]	0.2	Damping parameter
ρ_Γ [:]	0.1	Scaling factor for density in the 0D valve model
\hat{H} [m ⁻¹]	0.04	Initial curvature offset
t_0 [s]	0.08	Initial time of the simulation
T [s]	0.45	Final time of the simulation
Δt [s]	$1 \cdot 10^{-4}$	Time step

Table 4.2: Baseline parameters for the aortic valve simulations.

The density of the blood ρ was set to the value of $1060 \frac{\text{Kg}}{\text{m}^3}$ as reported in [36] for blood at temperature of 37.5°C. The value of the constant viscosity μ_{new} for the Newtonian case was set to $3.5 \cdot 10^{-3}$ Pa · s, as shown in Table 4.2, in accordance with other references such as [49, 56]. Concerning the RIIS parameters, we begin by setting $\varepsilon = 0.5$ mm, corresponding to a valve thickness of 1.0 mm. Then, as suggested in [49], we choose a mesh size in the valvular region $h = 0.34$ mm (see Table 4.1), to satisfy $h \leq 1.5\varepsilon$. In addition, with this setting of the parameter, the physiological thickness of an aortic valve is recovered: for example, it is shown in [115] that this physiological value ranges between 0.5 and 1.4 mm for people over 60 years old. In addition, both the resistance R , used in the RIIS model to enforce the fluid to follow the valve velocity and the damping parameter β were set in accordance with [56]. Finally, we set ρ_Γ to 0.1: this parameter can be tuned to different values in order to account for the inertia of the leaflets. The chosen value was found to yield a better match with physiology.

We simulated a whole systole using a time step $\Delta t = 1 \cdot 10^{-4}$ s. For the time discretization, we use a BDF scheme of order $s = 1$, corresponding to a semi-implicit Euler scheme.

4.2. Simulation of a healthy valve

We consider the case of a healthy valve, calibrating the model to reproduce the physiological behavior observed in healthy individuals, without stenosis and regurgitation. The simulation was obtained setting the remaining parameter of the 0D model, the elasticity coefficient, $\gamma = 0.2 \text{ N/m}$ and using the Newtonian model. The complete setting of the parameters to obtain this configuration is reported in Table 4.3.

$\rho \left[\frac{\text{Kg}}{\text{m}^3} \right]$	$\mu_{new} [\text{Pa} \cdot \text{s}]$	$\varepsilon [\text{m}]$	$R [\text{Pa} \cdot \text{s}]$	$\beta [\text{s}^{-1}]$	$\rho_\Gamma [\cdot]$	$\tilde{H} [\text{m}^{-1}]$	$\gamma \left[\frac{\text{N}}{\text{m}} \right]$
1060	$3.5 \cdot 10^{-3}$	$5 \cdot 10^{-4}$	1000	0.2	0.1	0.04	0.2

Table 4.3: Parameters for the healthy configuration.

This configuration is significantly sensitive with respect to little changes in various parameters, as better discussed in Appendix A. In practice, it was not possible to reproduce a comparable setting using the non-Newtonian model, since the changes in viscosity, albeit relatively small, lead to very significant changes in the valve dynamics.

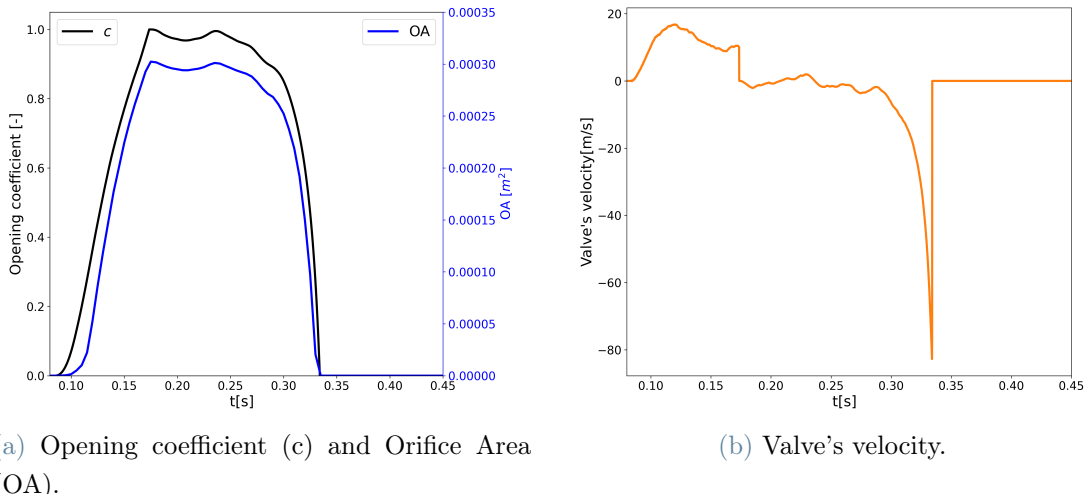


Figure 4.6: Opening coefficient and Orifice Area (a) and valve's velocity (b) in healthy configuration.

Figure 4.6 shows the dynamics of the valve. In particular, as we can observe from Figure 4.6 (a), the evolution of the orifice area (similar to the one of the opening coefficient) is in accordance with the evolution of a physiological valve. Indeed, we can see that the behavior of the orifice area during the systole can be divided into three stages, in accordance with [66, 83, 126]: an opening phase, a slow closure with very small changes of the

orifice area, and a rapid closure. In particular the duration of the opening phase (considering the valve as completely open if it reaches the 95 % of his maximum orifice area) in our configuration is of 83 ms in accordance with [66], which indicates as physiological an opening time of 76 ± 30 ms. As we can see from Figure 4.6 (a), the closing phase can be divided into two steps: a slower one of about 45 ms when the orifice area doesn't change much (approximately from 95 to 70 %), and a faster one of about 20 ms (from 70 to 0 %). In total the whole closing process requires about 65 ms, very close to the physiological one provided by [66] of 42 ± 16 ms. While the valve is open, we can observe oscillations akin to leaflet fluttering both in the opening coefficient and orifice area (see Figure 4.6 (b)).

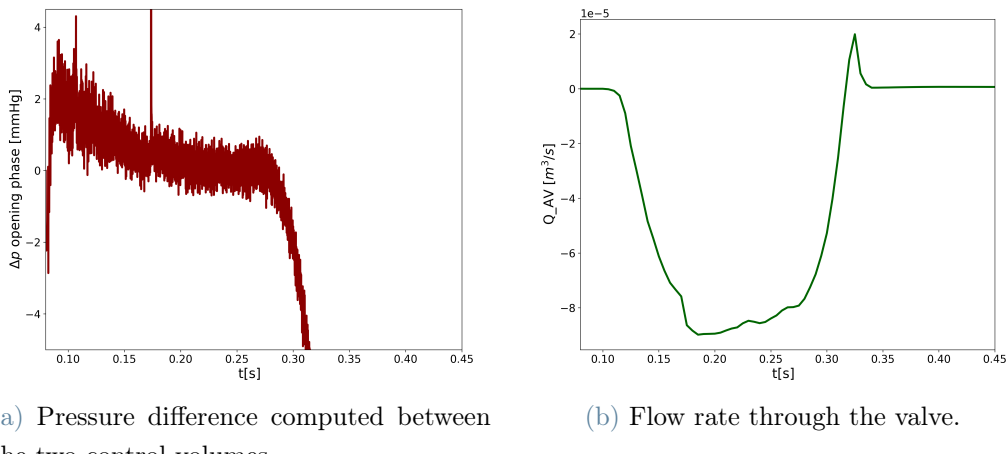


Figure 4.7: Pressure difference computed between the two control volumes in the opening phase and flow rate through the valve.

Two other important physiological aspects can be observed in Figure 4.7. The first one, shown in Figure 4.7 (a), is that the pressure difference computed between the two control volumes (that are shown in Figure 4.4, placed above and below the valve) does not exceed the value of 5 mmHg, that is considered to be the maximum limit that can be reached in the opening phase physiologically. Figure 4.7 (b), instead, shows the flow rate passing through the valve during the whole systole. The reverse flow that can be observed in the closing phase (from 0.30 to 0.32 s approximately) is acceptable both in duration and intensity (in particular with respect to the regurgitating configuration that will be shown in Section 4.3). Indeed, as already mentioned in Section 1.2, a short period of backward flow of blood immediately before the closure of the valve, followed by sudden cessation of the backflow, is observed even in healthy individuals [65].

4| A simulation study on the aortic valve

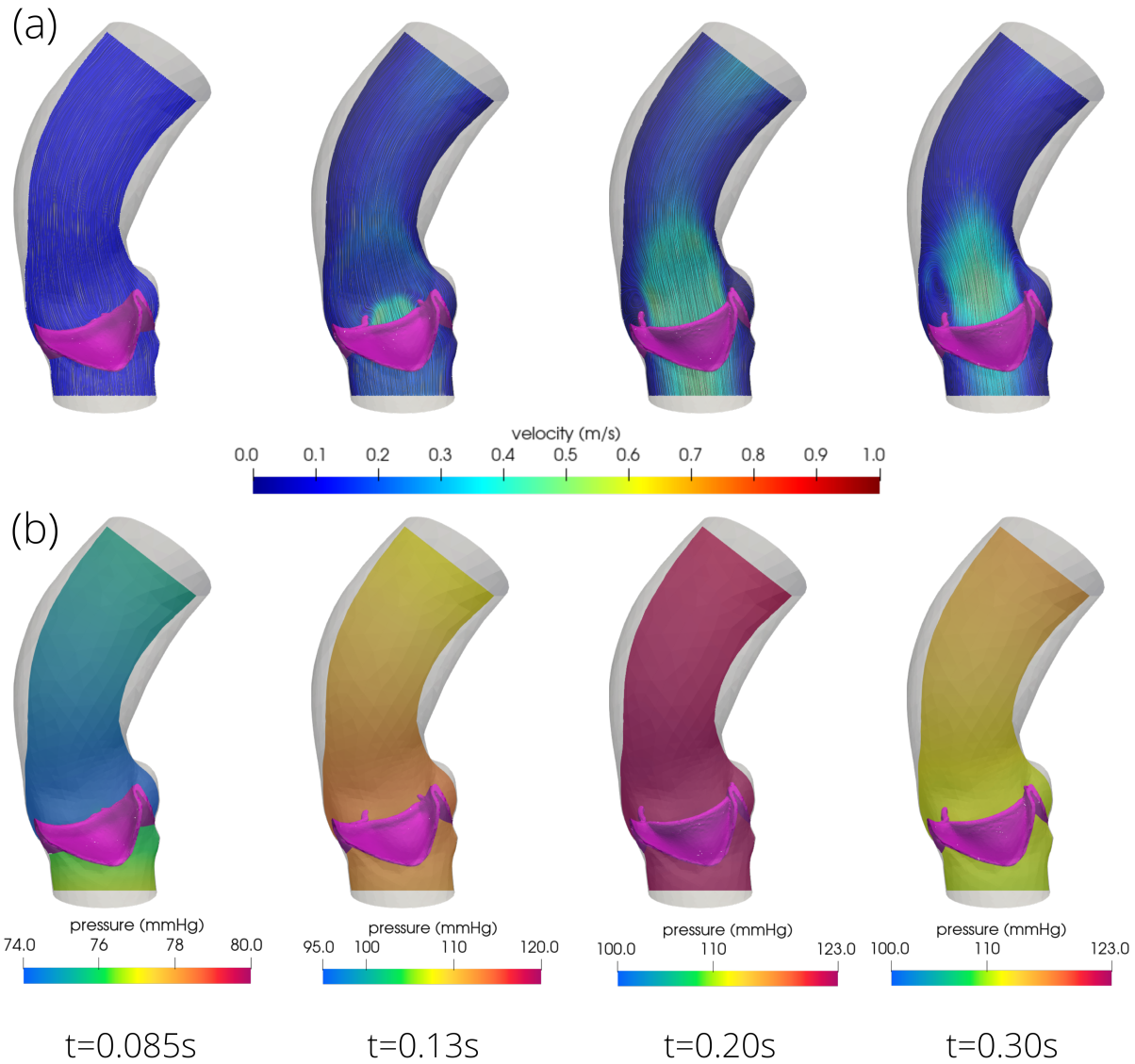


Figure 4.8: Velocity (a) and pressure (b) distribution at four different time steps: before the opening (0.085s), during the valve opening phase (0.13s), when the valve is completely open (0.20s) and during the closing phase (0.30s).

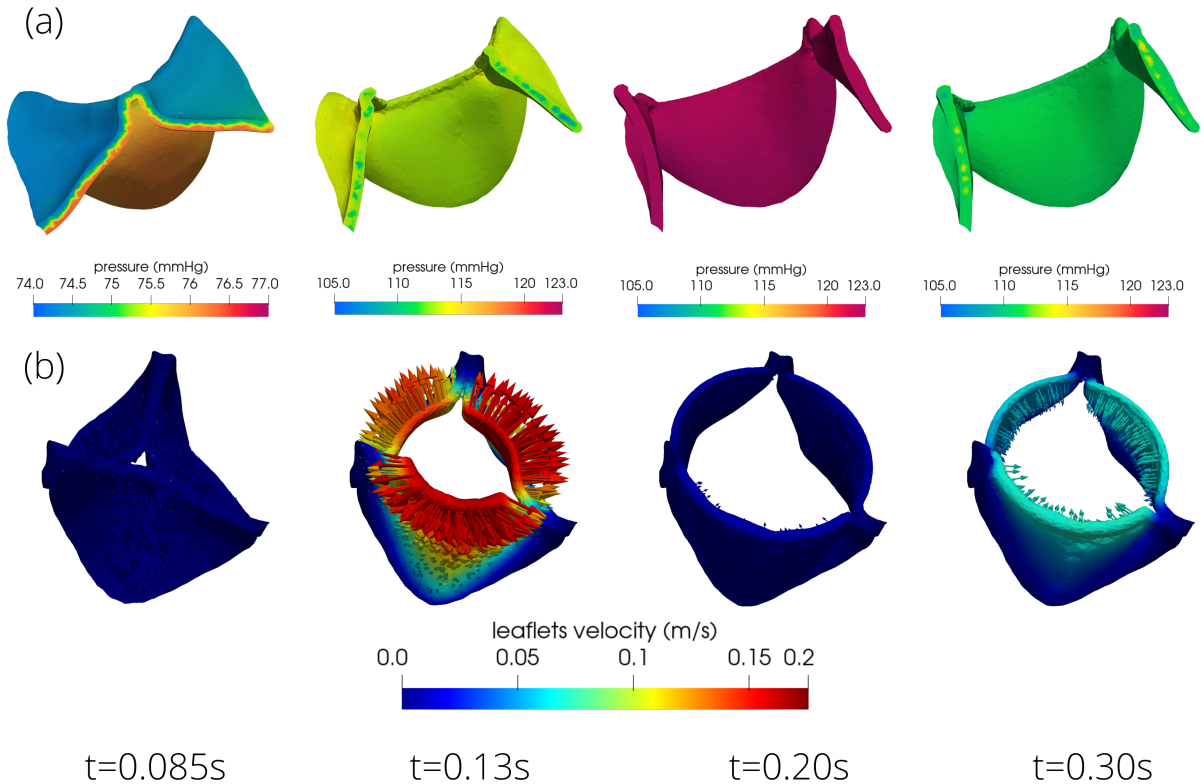


Figure 4.9: Pressure within the leaflets (a) and leaflets velocity \mathbf{u}_Γ (b) at four different time steps: before the opening (0.085 s), during the valve opening phase (0.13 s), when the valve is completely open (0.20 s) and during the closing phase (0.30 s).

The whole behavior of the fluid and the valve can be observed in Figure 4.8 and Figure 4.9. In Figure 4.8, the blood flow together with the corresponding pressure distribution at four different time steps is reported: before the opening, during the valve opening phase, when the valve is completely open and during the closing phase. Figure 4.9, instead, for the same time steps, shows the pressure distribution in the ε -neighborhood of the leaflets (a), the area in which the RIIS term is active, and the corresponding leaflets' velocity (b). As we can see from both Figure 4.8 (b) and Figure 4.9 (a) in the early stages of the simulation, while the valve is still closed, the whole pressure gradient is concentrated in correspondence of the valve and a pressure difference of about 2 to 3 mmHg is developed in this area which causes the beginning of the opening of the valve. Then, the opening is accompanied by a progressive development of the typical jet flow through the aortic orifice, and much smaller pressure differences can be observed. Despite this, during this phase, a non-negligible pressure gradient can be observed in the RIIS region, due to the non-zero leaflet velocity \mathbf{u}_Γ . Instead, when the valve reaches its fully open configuration, the pressure is essentially constant in the leaflets volume, since the valve velocity \mathbf{u}_Γ is

close to zero during this phase (except for the fluttering phenomenon described above, which can be observed, in particular, in Figure 4.9 (b) at time 0.20 s). With the valve fully open at the maximum orifice area, the aortic jet fully develops. We point out that the general behavior in the opening phase is qualitatively in accordance with [56]. As can be seen from in Figure 4.7 (a) the closing phase is accompanied by a strong negative pressure gradient. We remark that the beginning of the closing phase is delayed with respect to the inversion of the pressure jump which happens around $t = 0.2$ s. This happens due to the inertia of both the flow and the valve. Then, the valve starts its closing, at the beginning with \mathbf{u}_Γ much slower with respect to the opening phase, as can be appreciated from Figure 4.7 (b).

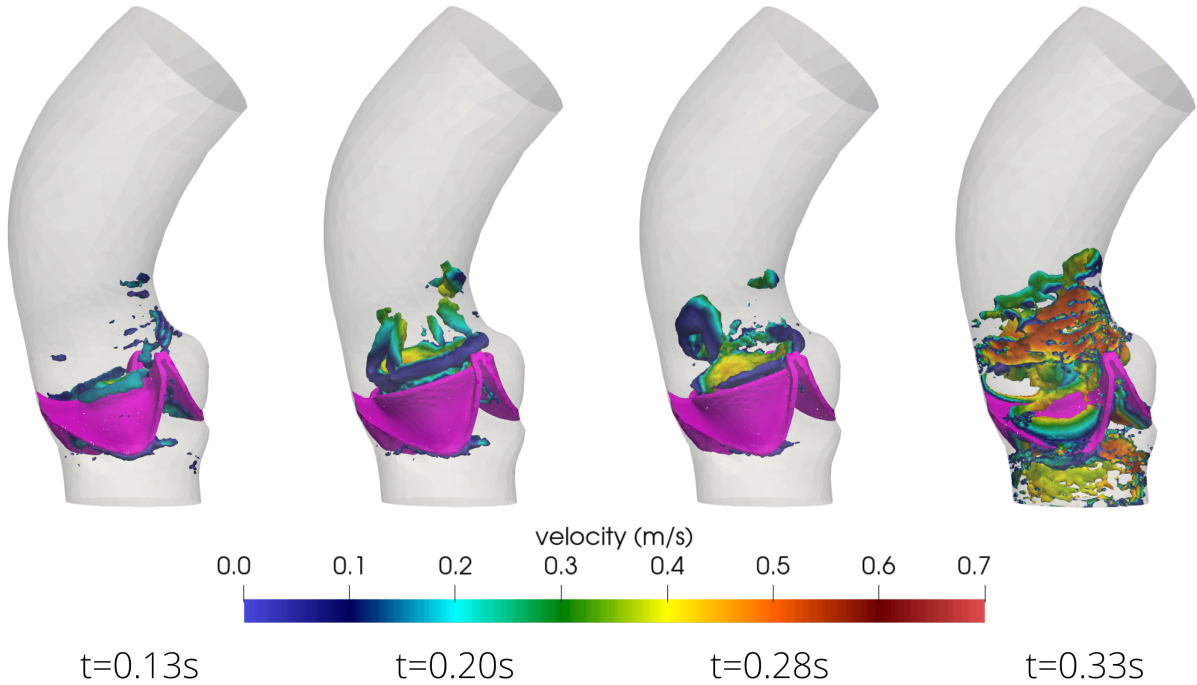


Figure 4.10: Q-criterion isosurfaces with $Q = 1000 \text{ s}^{-2}$ colored with velocity magnitude at four different time steps: during the valve opening phase (0.13 s), when the valve is completely open (0.20 s), during the slow part of the closing phase (0.28 s) and during the faster part of the closing phase (0.33 s).

Finally, in Figure 4.10 the Q-criterion isosurfaces [71] are shown for four different time steps: during the opening phase, when the valve is completely open, during the slow part of the closing phase and during the faster part of the closing phase. At $t = 0.2$ s we can see how the jet flow leads to the formation of the classical ring coherent structures detaching from the tips of the aortic leaflet, observed, for example, in [26]. As discussed in [30, 49], these vortices also help the leaflets not to attach to the aortic wall. The vortex structures

are then transported downwind in the ascending aorta and the jet breaks up just before the beginning of the fast part of the closing phase.

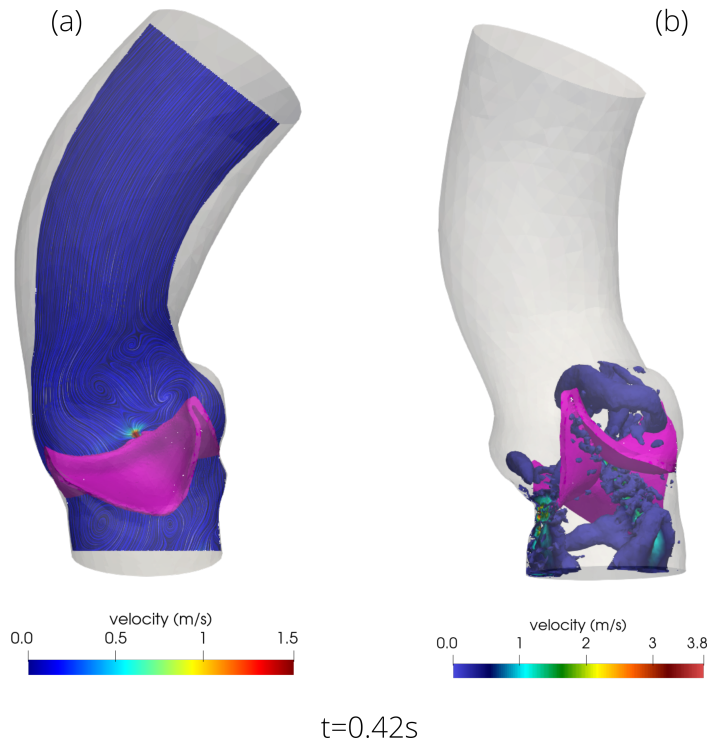


Figure 4.11: Velocity distribution (a) and Q-criterion isosurfaces with $Q = 1000 \text{ s}^{-2}$ colored with velocity magnitude (b) at $t=0.42 \text{ s}$.

We point out that, due to geometrical inconsistencies, some reverse flow can be observed when the valve is closed. This occurs both between the valve and the wall and at the center of the valve. The issue is associated to a mismatch between the valve and the aortic root geometry, on the one hand, and to the choice of the thickness parameter ε on the other. To avoid this issue, we would need to set $\varepsilon \geq 1.5 \text{ mm}$, corresponding to a valve thickness greater than 3 mm, much larger than what is observed in real valves. Alternatively, the valve and aortic root geometries could be manually adjusted to improve their consistency. However, in absence of imaging data to support this operation, we opted to keep the original models. Both approaches would require a thorough recalibration of the 0D valve model. We point out that this inconsistency does not affect significantly the valve behavior during its opening and closing, which are the main focus of this work, but is mostly relevant only after the valve is fully closed.

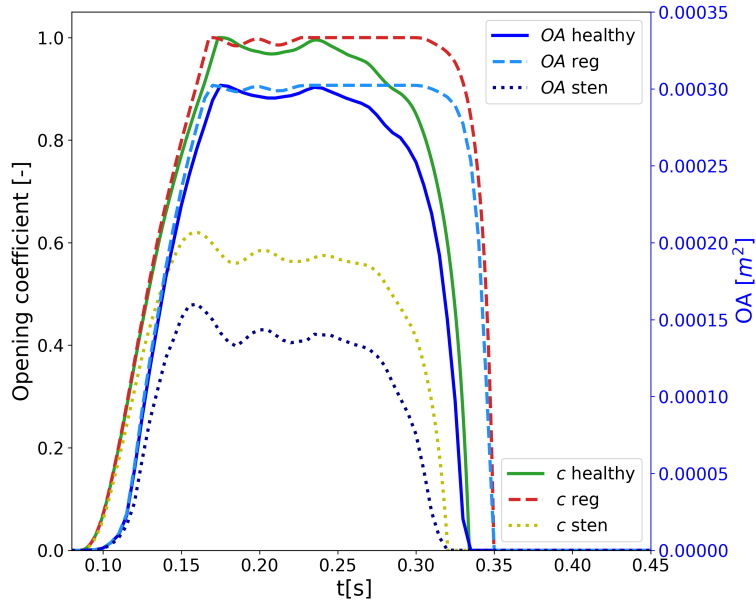
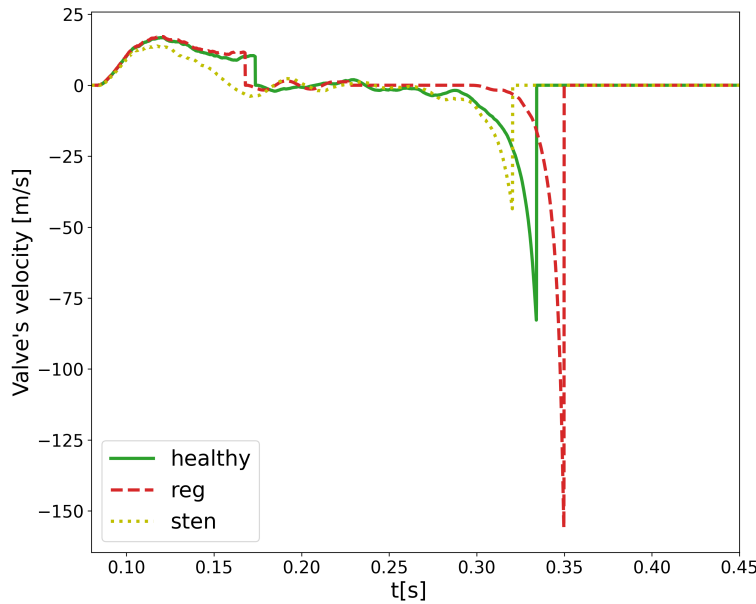
4.3. Simulation of pathological cases

This section is devoted to the analysis of the two most common pathological cases that can be caused by a dysfunction of the aortic valve, that are stenosis and regurgitation, as explained in Section 4.3. In particular, a comparison between these two cases and the healthy one (presented in Section 4.2) will be provided, with particular focus on the dynamics of the valve. For the regurgitation test case, we do not consider malformations in the valve that lead to reverse flow when it is closed. Instead, we consider a delayed closing that results in reverse flow occurring while the valve closes, and stopping once it is fully closed. This behavior was induced in the simulation by decreasing the elasticity coefficient $\gamma = 0.1 \text{ N/m}$, so that the elastic response of the valve is slower and the closure phase is even further delayed with respect to what happens in physiological conditions.

The stenotic configuration, instead, reproduces what can be observed in calcified stenosis: this pathology usually causes a reduced compliance of the leaflets which then oppose a higher resistance to the blood flow [26]. In accordance with this, this configuration was obtained by increasing the elasticity coefficient to $\gamma = 1.0 \text{ N/m}$. To classify the level of stenosis, the aortic stenosis ratio AS can be introduced, as in [49, 119]: this parameter is based on the maximum orifice area OA_{\max} in the following way: $AS = 1 - \frac{OA_{\max}}{OA_{\text{healthy}}}$ with OA_{healthy} corresponding to the max orifice area of the healthy case. With this setting $AS = 0.47$ was obtained, which corresponds to a moderate level of stenosis.

These considerations show how the parameters of the model can be interpreted in a physical sense, and how these can be tuned to obtain different configurations. For example, higher levels of stenosis can be obtained by further increasing γ : this is a very interesting feature of the lumped parameter mechanical model used for valve dynamics.

4.3.1. Comparison with healthy configuration

(a) Opening coefficient (c) and Orifice Area (OA).

(b) Valve's velocity.

Figure 4.12: Comparison of the opening coefficient and Orifice Area (a) and valve's velocity (b) in the three configurations.

Figure 4.12 shows the comparison between the dynamic of the valve in the three different configurations for the whole systole. In particular, from Figure 4.12 (a) we can see how both the orifice area and the opening coefficient for the stenotic case do not reach the

value of complete opening that is reached in both healthy and regurgitant cases. The opening stage takes less time in the stenotic case with respect to the healthy case (about 55 ms against 85 ms of the healthy one), and this happens even though the velocity of the valve during the opening is similar or smaller than the healthy one, as we can see from Figure 4.12 (b). However, this is justified by the fact that, since the maximum orifice area reached is much smaller, less time is required to reach this state. Similar considerations can be done for the closing phase: the velocity of the valve is slower, but the duration of this phase is shorter (about 47 ms).

Concerning the regurgitant case, we can see that the opening phase is only slightly faster with respect to the healthy one (about 73 ms), while the closing phase is much faster: only 35 ms. This happens because the closing phase is delayed, since we have a smaller elasticity coefficient, and by the instant when the closing starts the pressure gradient is already much higher. This is even more evident when looking at Figure 4.12 (b), where we can see how much higher is the velocity of the regurgitant valve during the closing phase with respect to the two other configurations. Moreover, for the regurgitant case we can notice that the fluttering of the valve is present only in the first part of the phase when the valve is completely open.

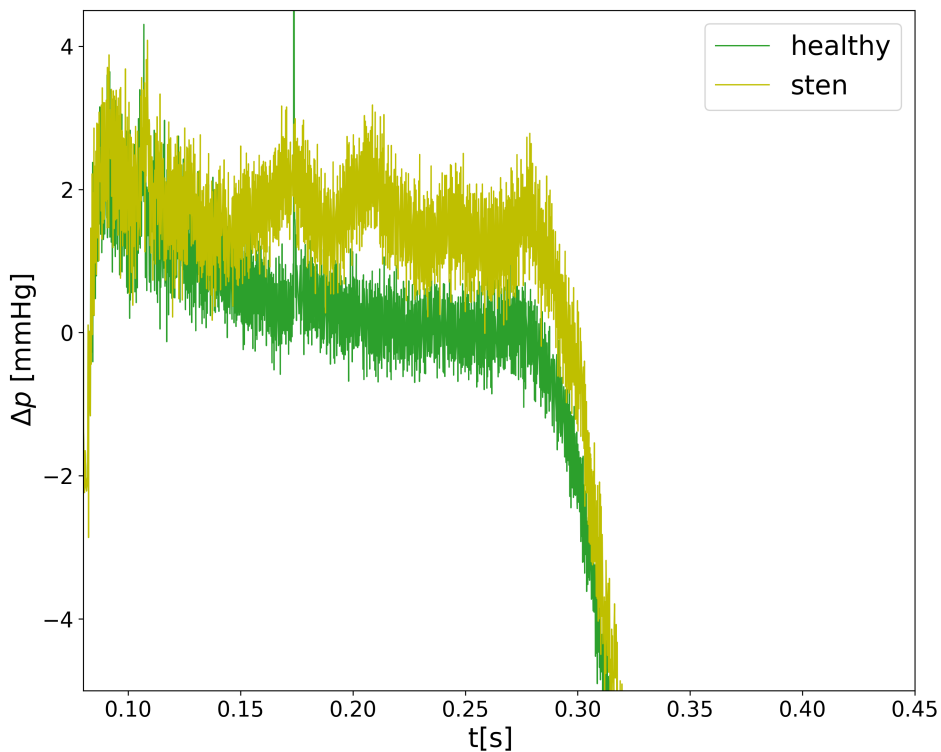


Figure 4.13: Comparison between pressure difference computed between the two control volumes in the healthy and stenotic cases.

The main difference in the pressure jump in the opening phase can be observed between the stenotic and healthy case in Figure 4.13 (the regurgitant case was not reported in this plot for ease of interpretation, since the behavior was very similar to the healthy case). Indeed, we can notice that the pressure jump has an average value that increases with stenosis in the opening and completely open phases.

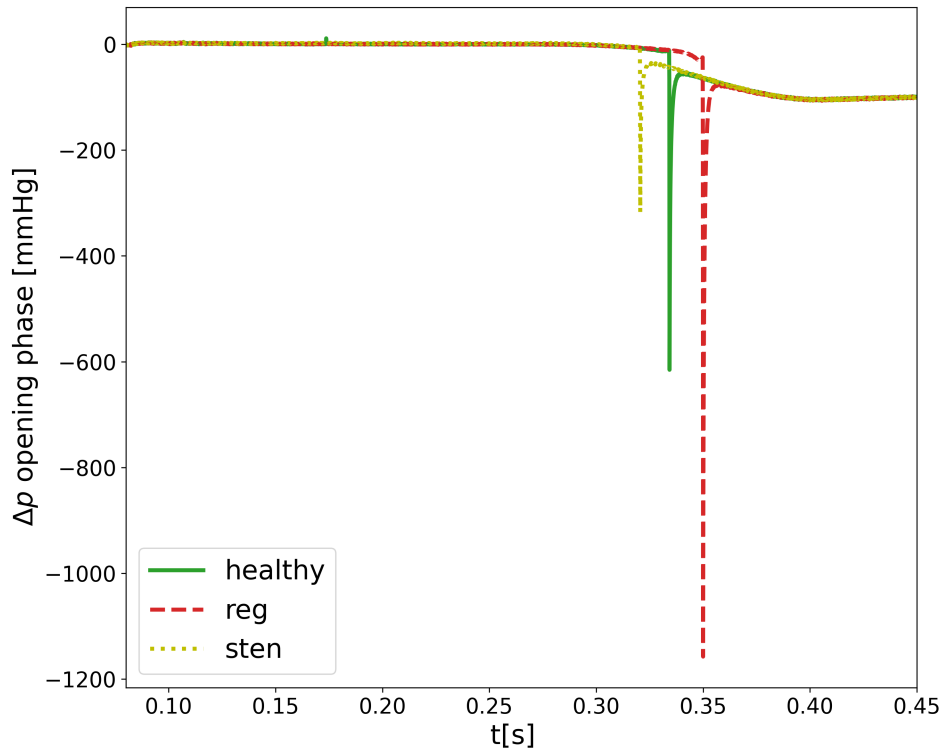


Figure 4.14: Comparison between pressure difference computed between the two control volumes in the three pathological cases.

Instead, from Figure 4.14 we can observe that the peak in the pressure jump reached during the closing phase is delayed for the regurgitant case while it is anticipated in the stenotic case, in accordance with what happens in the valve dynamic as shown in Figure 4.12.

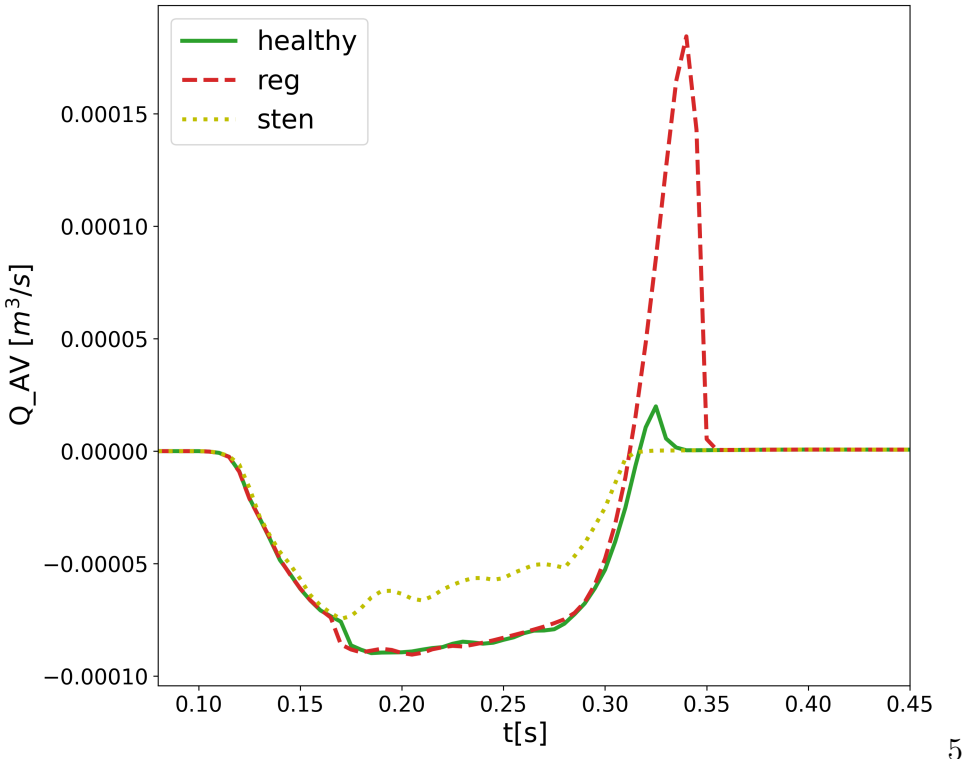


Figure 4.15: Comparison between flow rate through the valve in the three pathological cases.

Finally, Figure 4.15, shows the flow rate passing through the valve in the three different cases. As we can see, the stenotic valve shows no backward flux at all during the closure, and this is in accordance with the fact that regurgitation is uncommon when calcified stenosis is present [52]. We also point out that the reverse flow observed in the regurgitant case is not in the range associated with healthy valves, in terms of both duration and intensity. Indeed, in this case, the delay in the closure of the valve causes the pressure jump to increase significantly, and the valve begins closing too late, so that a strong backward flux returns into the ventricle. Not only this flux is very intense in magnitude, but, as we can see, the duration of this phenomenon is quite long: almost 5 ms. However, after this period, when the valve reaches its completely closed configuration, the regurgitation completely vanishes.

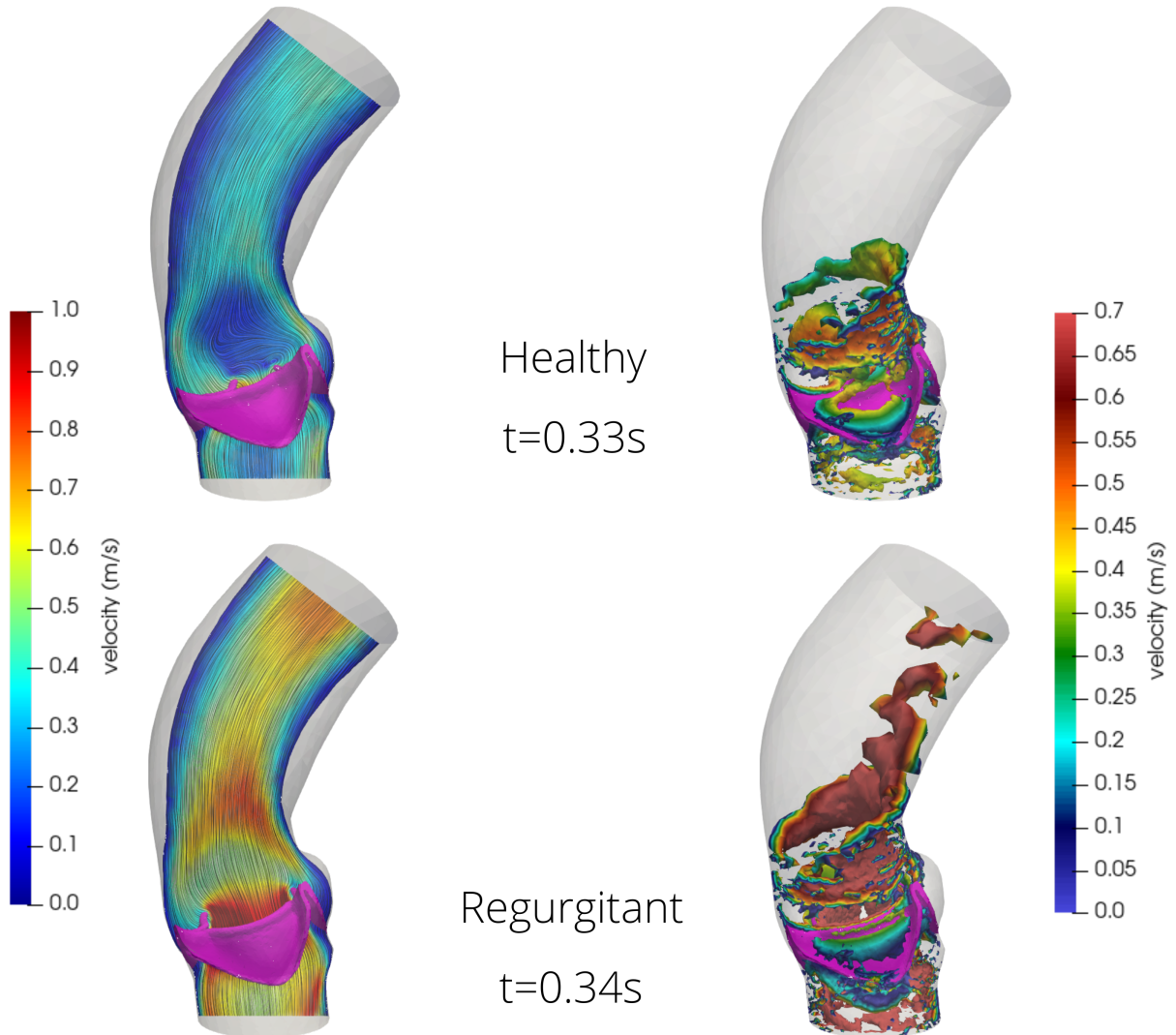


Figure 4.16: Comparison at the time of regurgitation between healthy (top) and regurgitant (bottom) valves. On the left the velocity distribution and on the right Q-criterion isosurfaces with $Q = 1000 \text{ s}^{-2}$ for the two cases respectively at $t=0.33\text{s}$ and $t=0.34\text{s}$.

This phenomenon has a strong impact on the dynamic of the flow, as can be observed in Figure 4.16 where we compare the velocity distribution and the vorticity visualized by Q-criterion isosurfaces for the healthy and regurgitant cases at $t=0.33\text{s}$ and $t=0.34\text{s}$, that are the instants of maximum backward flow for the two simulations, as can be seen from Figure 4.15. Indeed, in the healthy case this backward flow seems to have an ordinary regime and a relative small intensity, while for the regurgitant case the velocities are very high and the vorticity structures of the flux seem very unstable and chaotic: we highlight that this is caused by the high pressure jump that is generated by the delay in the start of the closing phase.

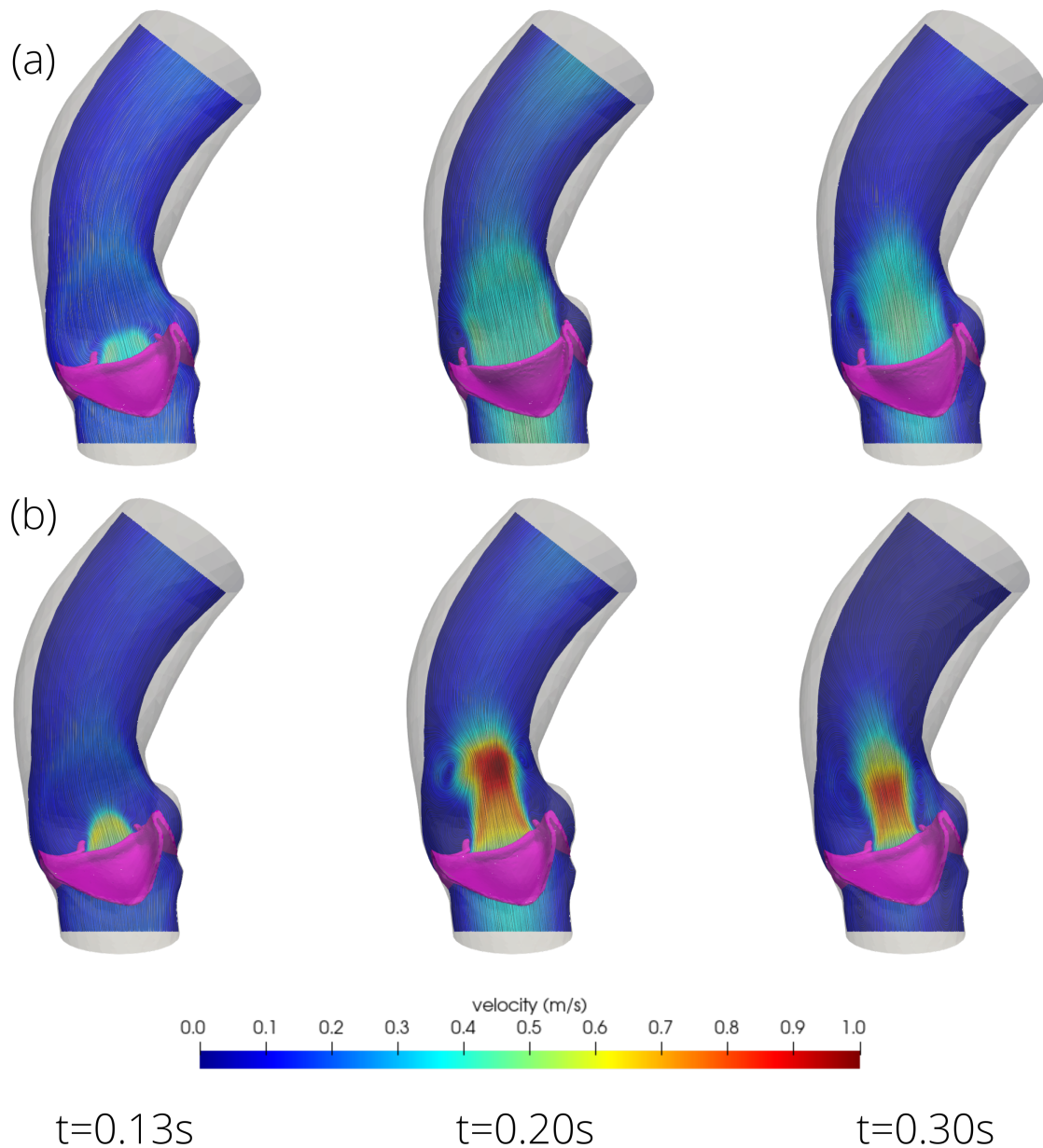


Figure 4.17: Velocity distribution in healthy (a) and stenotic (b) cases for three different time steps: during the valve opening phase (0.13 s), at maximum valve opening (0.20 s) and during the closing phase (0.30 s).

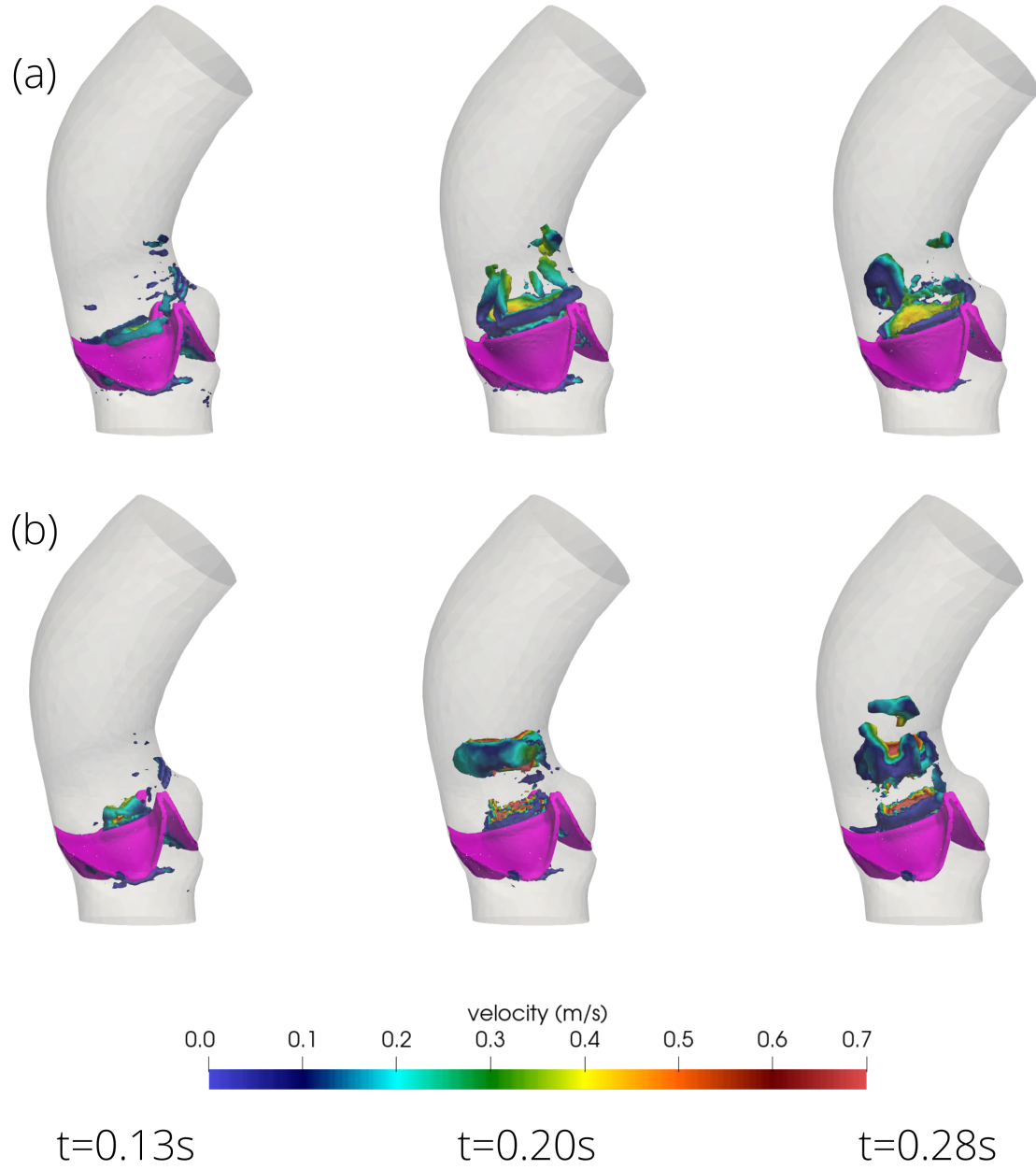


Figure 4.18: Q-criterion isosurfaces with $Q = 1000 \text{ s}^{-2}$ for healthy (a) and stenotic (b) configurations colored with velocity magnitude at three different time steps: during the opening phase (0.085 s), when the valve is completely open (0.20 s) and during the slow part of the closing phase (0.28 s).

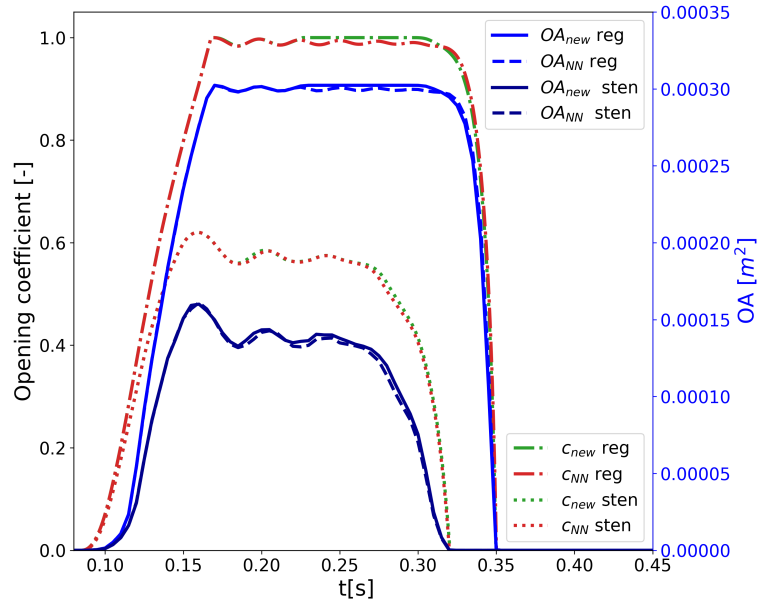
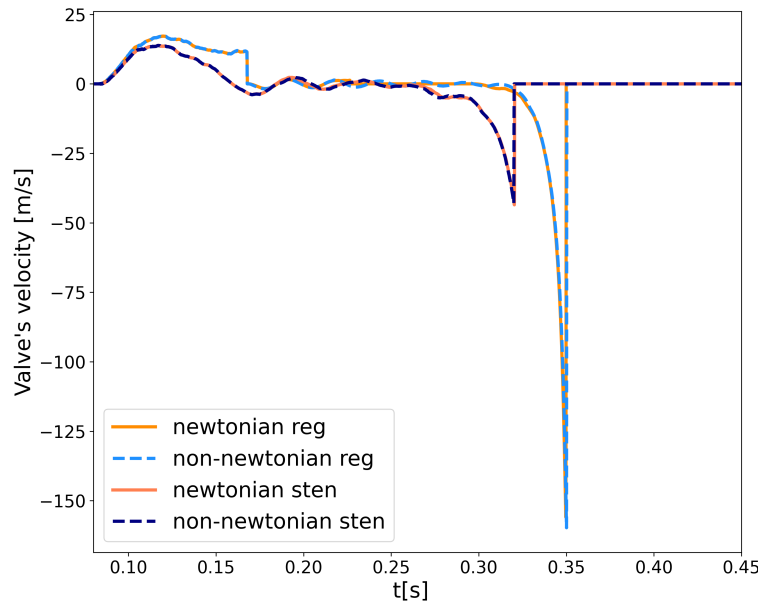
Some differences in the dynamics of the flux can be observed even in the stenotic case, as shown in both Figure 4.17 and Figure 4.18, where the velocity distribution and the Q-criterion isosurfaces are shown for the healthy (a) and stenotic (b) configurations for three different time steps: during the opening phase, when the valve is completely open

and during the closing phase. In the stenotic case, the reduced orifice area and the shorter time interval in which flow is allowed through the valve yield a stronger aortic jet and a more disorganized velocity distribution. Moreover, in the ascending aorta, slightly large and more persistent recirculation regions than in the healthy case, and the corresponding coherent structures, could indicate a longer residence time of blood in this portion of the vessel and thus a reduced cardiac output.

4.4. Comparison between Newtonian and non-Newtonian models in pathological cases

In this section the comparison of the simulations performed using the Newtonian rheology versus the ones using the non-Newtonian model will be provided. Similarities and differences between these simulations will be highlighted, providing some comparison with results that can be found in the literature. As already seen in Section 4.3 the results are obtained imposing the elasticity coefficient $\gamma = 0.1 \text{ N/m}$ for the regurgitant case, and $\gamma = 1.0 \text{ N/m}$ for the stenotic case. For each pathological configurations two simulations were performed: one with Newtonian rheology and one with the non-Newtonian model. We recall that the value of the constant viscosity μ_{new} for the Newtonian case was set to $3.5 \cdot 10^{-3} \text{ Pa} \cdot \text{s}$, as shown in Table 4.2. The values for the Carreau parameters are the ones shown in Table 2.1, except for μ_∞ which was set to be equal to μ_{new} , that is $\mu_\infty = 3.5 \cdot 10^{-3} \text{ Pa} \cdot \text{s}$. This variation with respect to the typical parameters used in [34] was performed to be coherent with the fact that, for very low values of the shear rate, the viscosity should be considered constant and equal to the value employed in the Newtonian model. Moreover, this guarantees a fairer comparison between the two models.

4.4.1. Valve's dynamic and pressure jump

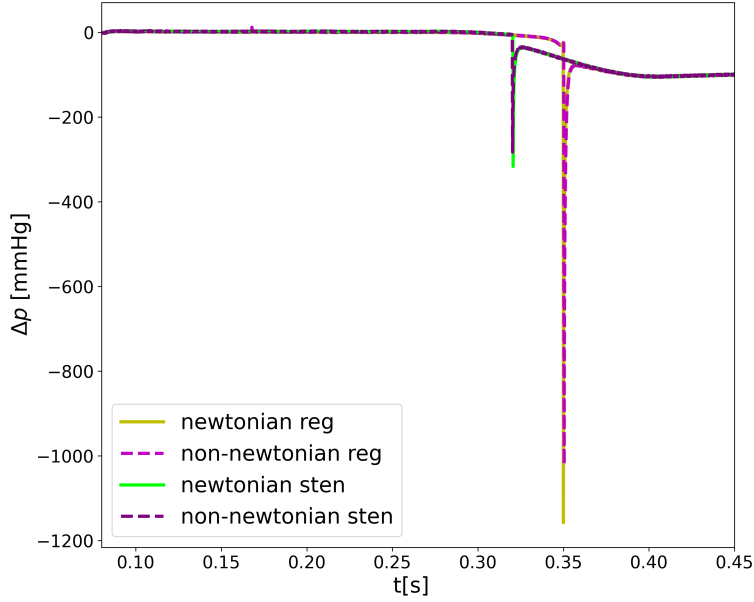
(a) Opening coefficient (c) and Orifice Area (OA).

(b) Valve's velocity.

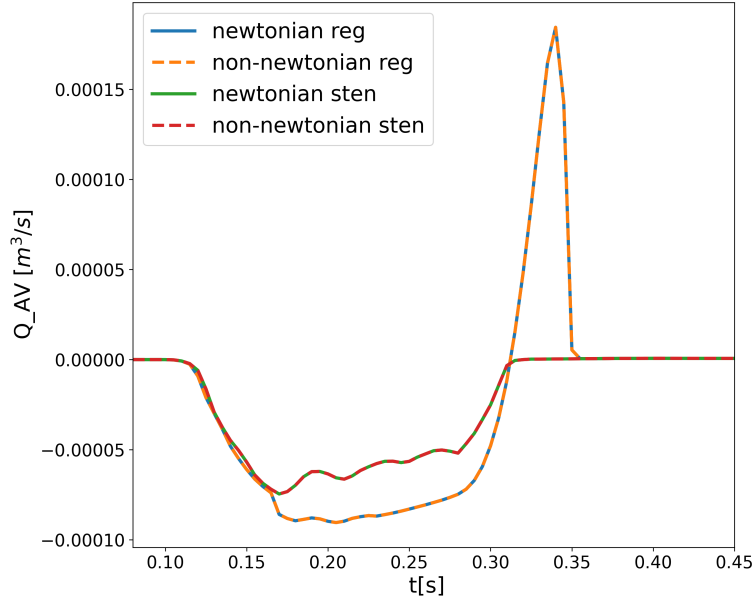
Figure 4.19: Comparison of the opening coefficient and Orifice Area (a) and valve's velocity (b) with Newtonian and non-Newtonian rheology in the two pathological cases.

As we have seen in the previous sections, the first thing that should be compared for this kind of simulation is the dynamic of the valve. As can be seen from Figure 4.19 (a) both the opening coefficient and the orifice area show very little differences when choosing a

non-Newtonian rheology, both for the regurgitant and the stenotic configurations. This can be observed even from Figure 4.19 (b) where the differences in the velocity of the valve are barely noticeable for both pathological configurations.



(a) Pressure jump.



(b) Flow rate through the valve.

Figure 4.20: Comparison of the pressure difference (a) and flow rate through the valve (b) with Newtonian and non-Newtonian rheology in the two pathological cases.

These observations can be extended to the pressure jump computed between the two

control volumes and to the flow rate passing through the valve during the whole systole. Indeed, it can be noticed from Figure 4.20 (a) that the behavior of the pressure jump is very similar for the two rheological models, except for the value reached at the peaks of the pressure jumps during the closing phase, which can be observed at $t = 0.35\text{ s}$ and $t = 0.32\text{ s}$ for the regurgitant and stenotic configurations, respectively. Moreover, Figure 4.20 (a) shows that there are no significant differences induced by the different rheology even for what concerns the flow rate passing through the valve during the whole systole.

These results are in accordance with what is observed in [8, 39], even if the model used and the problem studied are quite different (both these works study a mechanical bileaflet valve instead of a physiological one). However, our results are in accordance with these references: the authors also conclude that the rheological model has only little influence on quantities such as valve dynamics, transvalvular pressure drop and large-scale flow structure.

4.4.2. Wall shear stress

A more significant difference, instead, can be observed in more “specific” quantities, such as wall shear stress. In arterial blood flow, the wall shear stress, is defined as

$$\mathbf{WSS} = \left(\mu \frac{\partial \mathbf{u}_t}{\partial r} \right)_{r=0} \quad (4.2)$$

where \mathbf{u}_t is the flow velocity parallel to the wall and r is the radial distance to the wall [81, 124]. Physically it expresses the force per unit area exerted by the wall on the fluid in a direction on the local tangent plane [79]. Wall shear stress has often great importance in the medical field [79, 95, 103, 144], for example it has great influence in the formation of plaque in atherosclerosis [95] or in the wall elasticity [144].

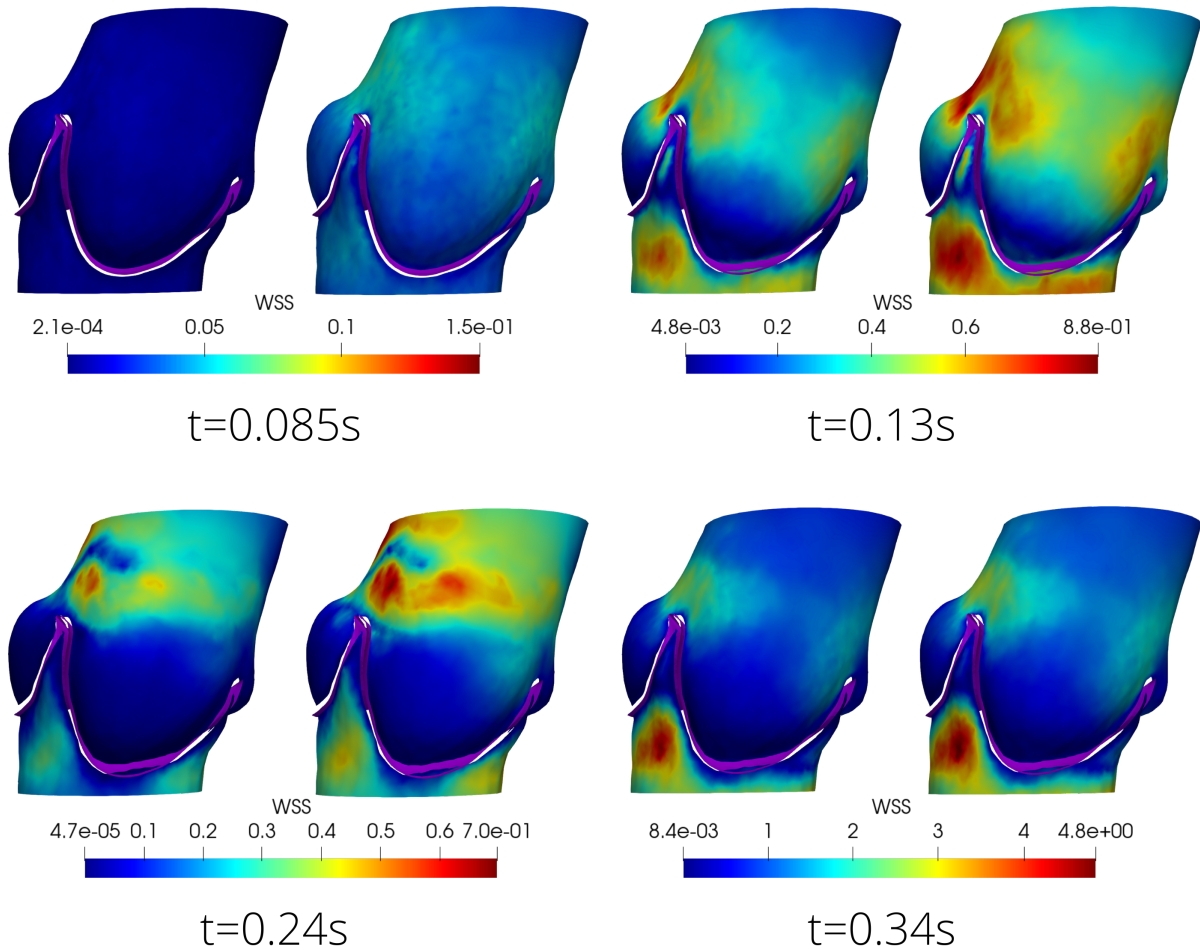


Figure 4.21: Comparison with Newtonian (left) and non-Newtonian (right) magnitude of the wall shear stress on the aortic root for regurgitant configuration on four different time steps: before the opening (0.085s), during the valve opening phase (0.13s), when the valve is completely open (0.24s) and during the closing phase (0.34s).

Figure 4.21 shows the magnitude of WSS for the regurgitant configuration in the aortic root at four different time steps. As we can see, in this case, the differences observed between the two rheological models are not negligible, and at different time steps we can observe different behaviors. It should be mentioned that the area corresponding to the aortic valve was removed during the post-processing (the area is colored in violet and contoured by white in Figure 4.21) for all these simulations. Indeed, in this area, because of how the RIIS method works, we are not solving the Navier-Stokes problem, but we are weakly imposing the velocity of the valve, so that evaluations of the WSS in this region have no physical meaning. We can observe that the wall shear stress is always higher in the non-Newtonian case, probably because in this case the viscosity of the fluid is always

greater or equal than the Newtonian one (that corresponds to μ_∞ of the Carreau model, so the minimum viscosity that can be achieved). It is interesting to notice how these differences change for different time periods and for different areas of the domain. For example, we can observe that before the opening of the valve, when the fluid velocity is low, the differences between the two rheological models are significant in the whole domain. Instead, during the peak of regurgitation ($t = 0.34$ s), happening in the closing phase, where the velocities are much higher, the value of the wall shear stress increases a lot, but the differences observed between the two rheological models are less significant.

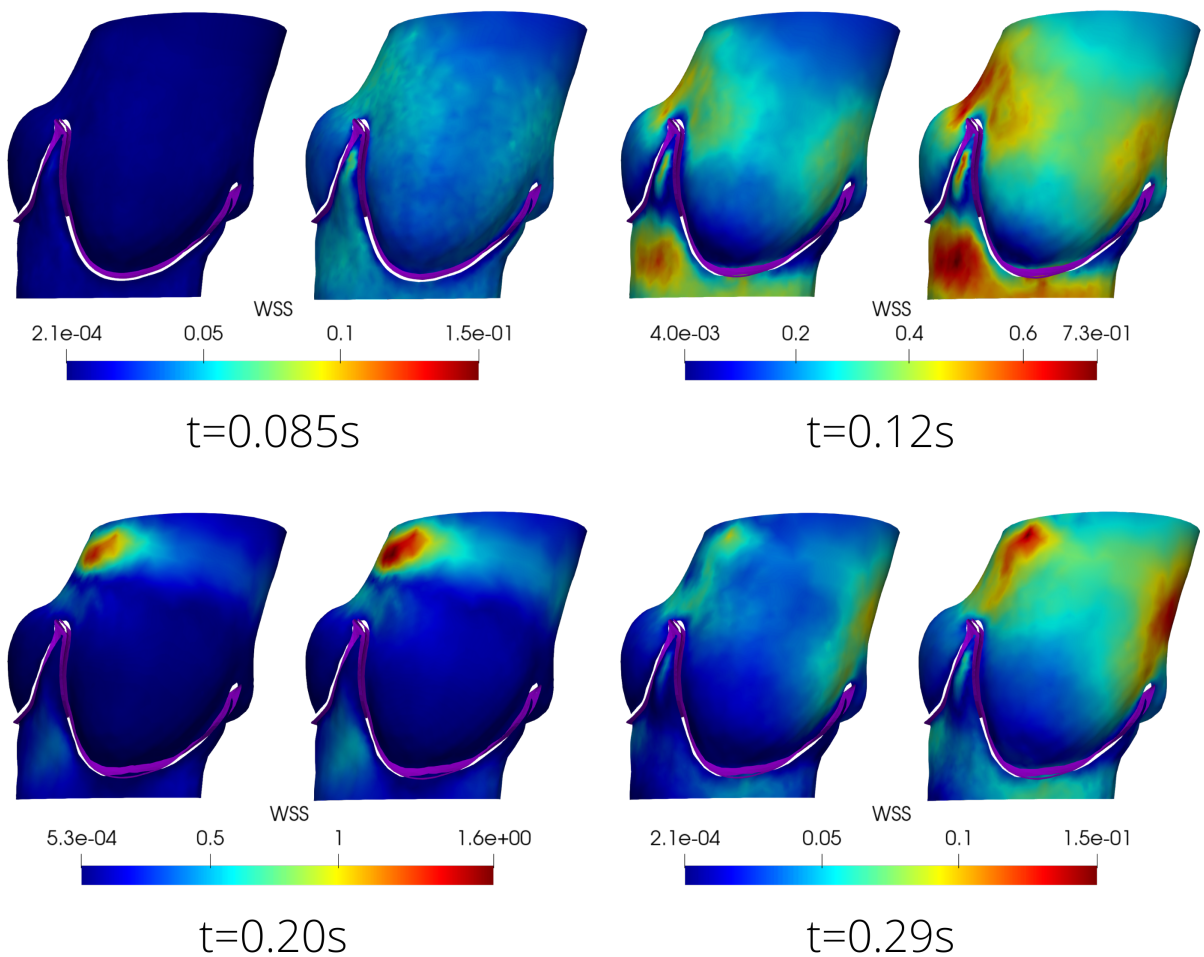


Figure 4.22: Comparison with Newtonian (left) and non-Newtonian (right) magnitude of the wall shear stress for stenotic configuration on four different time steps: before the opening (0.0085 s), during valve opening phase (0.12 s), when the valve is completely open (0.20 s) and during the closing phase (0.29 s).

A similar behavior can be observed in the stenotic case, as shown in Figure 4.21. It is interesting to notice that at $t = 0.20$ s there is an area with high value for the wall shear

stress. This area is probably generated by the strong aortic jet that can be observed in Figure 4.17. In the closure, the wall shear stress has a significantly smaller value with respect to the regurgitant case, because in this case the velocity of the fluid is much slower. However, more differences in the wall shear stress distribution can be observed between the two rheological models, probably because of the smaller shear rate that is developed in this scenario.

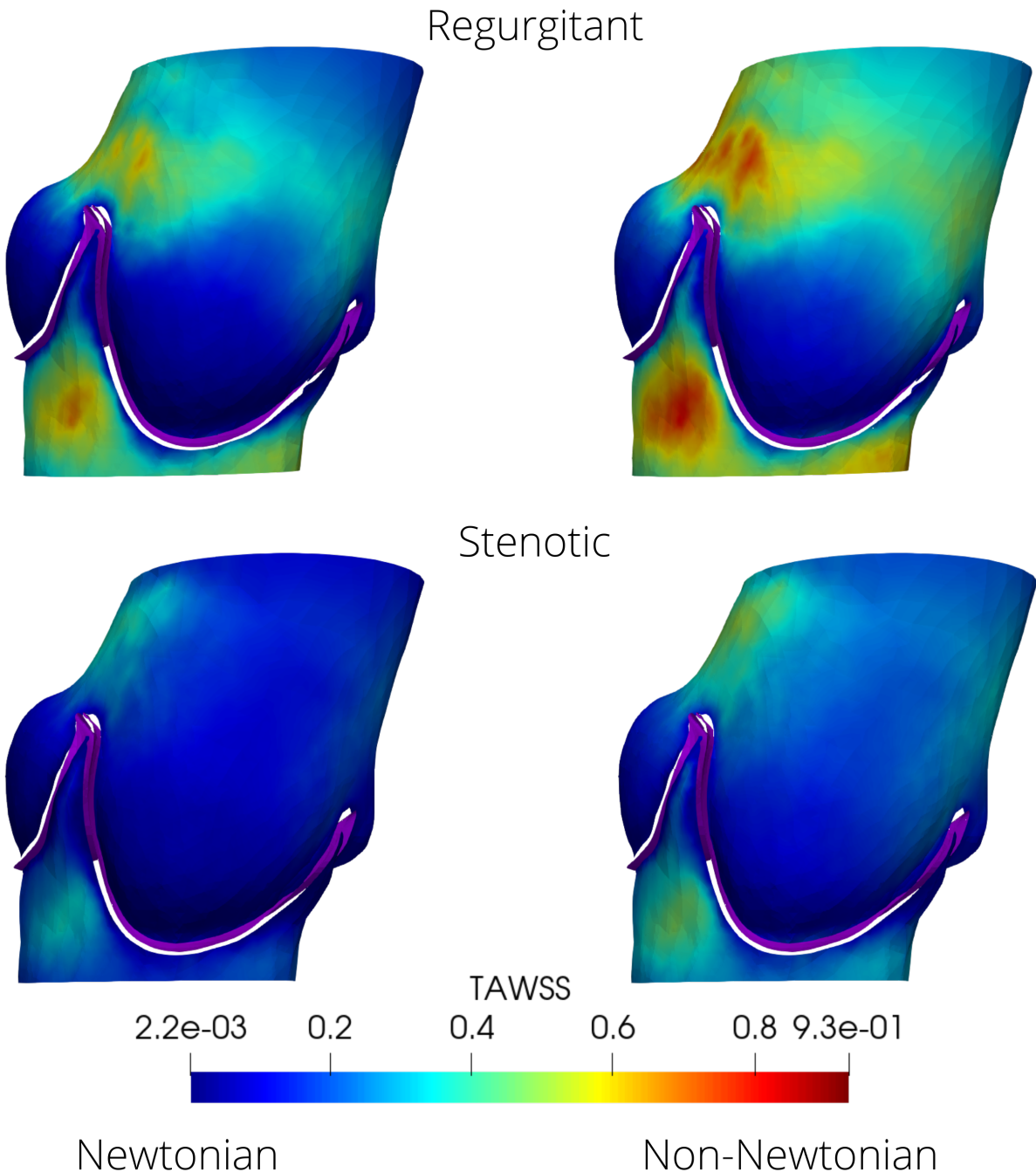


Figure 4.23: Time-Averaged Wall Shear Stress comparison between Newtonian (left) and non-Newtonian (right) model in regurgitant and stenotic configurations.

A useful indicator to understand the behavior of the shear stress on the vessel wall throughout the whole time period is the Time-Averaged Wall Shear Stress (TAWSS). This quantity can be computed as

$$\text{TAWSS} = \frac{1}{T} \int_0^T |\mathbf{WSS}(\mathbf{s}, t)| dt \quad (4.3)$$

in the same way as [145]. Figure 4.23 shows the TAWSS computed for both stenotic and regurgitant cases with Newtonian and non-Newtonian rheology. For the regurgitant case, we compute the TAWSS until $T = 0.35$ s. Conversely, for the stenotic case, we compute it until $T = 0.29$ s, to better focus on the time frame of interest, excluding the phase when the valve is fully closed. As we can see the value of TAWSS is generally higher in the regurgitant case, probably because the regurgitation induces a period of very high velocity, particularly in some (red) areas.

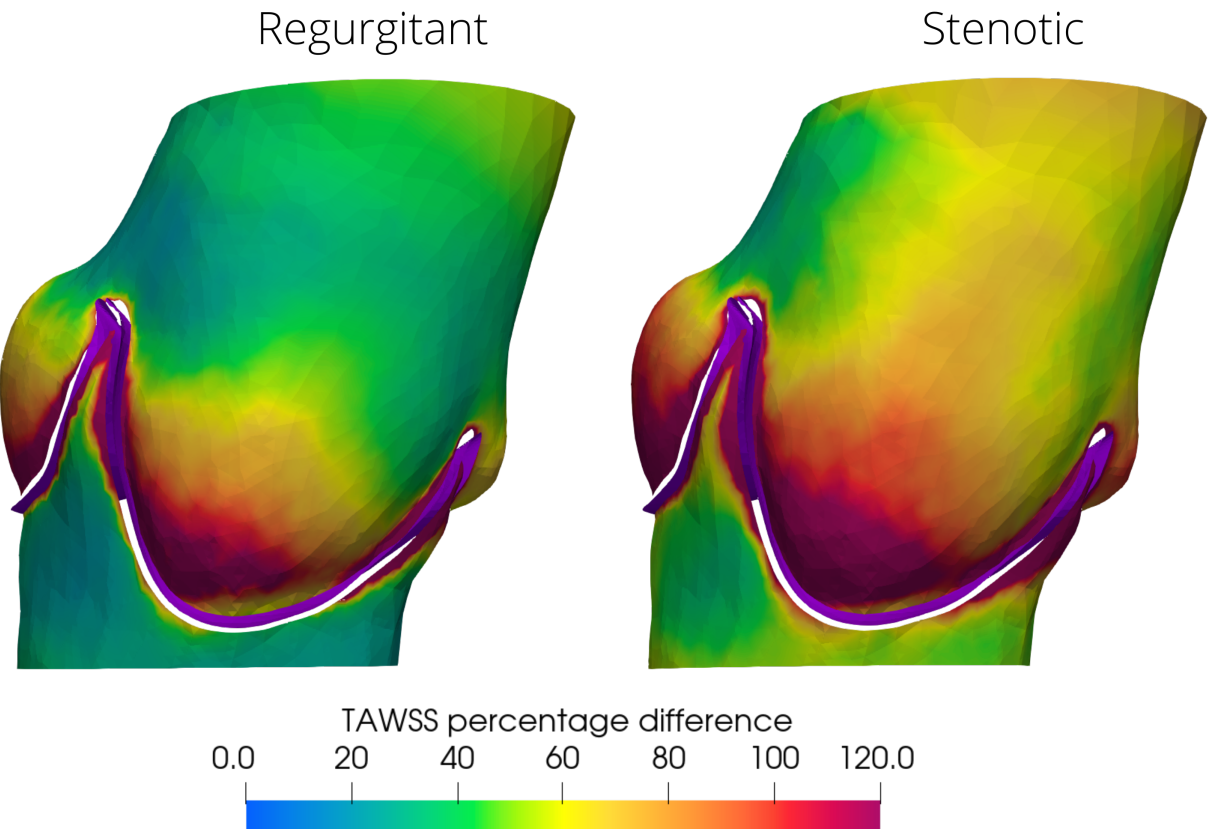


Figure 4.24: Percentage difference between Time-Averaged Wall Shear Stress (see Equation (4.4)) in regurgitant (left) and stenotic (right) cases.

These observations can be summarized by Figure 4.24. This picture shows the percentage

difference in the TAWSS. This quantity is computed as:

$$\text{TAWSS percentage difference} = 100 \frac{\text{TAWSS}_{\text{non-Newtonian}} - \text{TAWSS}_{\text{Newtonian}}}{\text{TAWSS}_{\text{Newtonian}}} \quad (4.4)$$

similarly to what is done to compute the percentage difference of WSS in [84]. This picture shows the difference that is generated by the rheological model, and as we can see, this difference is significant for both configurations. In the red areas this difference reaches more than 100%. As we can see from Figure 4.23 these are typically areas where the value of TAWSS is quite low, and so the quantitative difference may be not as significant as it seems. However, basically in the whole domain and even in the areas where the TAWSS is higher, we can observe differences that are around $20 \sim 50\%$. This means that if one is interested in computing the WSS in the aortic valve domain, the choice of the rheological model is very impactful, and the non-Newtonian nature of blood should not be neglected.

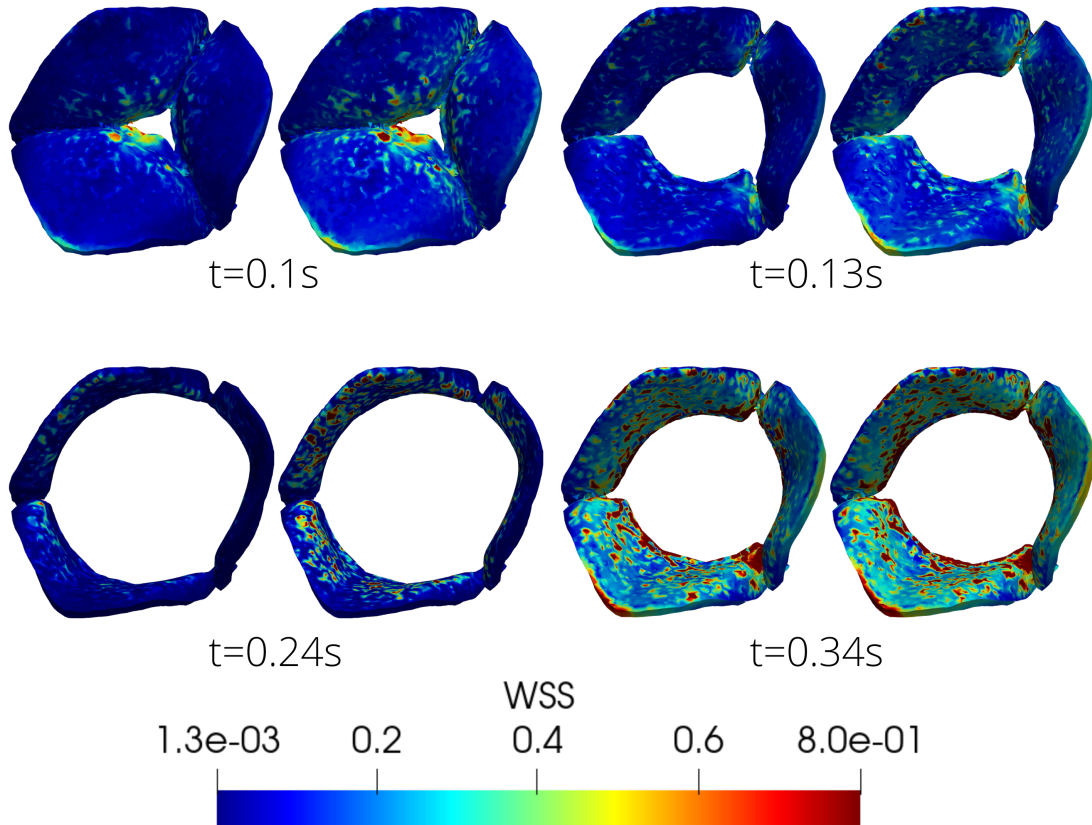


Figure 4.25: Comparison with Newtonian (left) and non-Newtonian (right) magnitude of the wall shear stress on the aortic valve for regurgitant configuration on four different time steps: during the first stage of the valve opening (0.1s), in the middle of the opening phase (0.13s), when the valve is completely open (0.24s) and during the closing phase (0.34s).

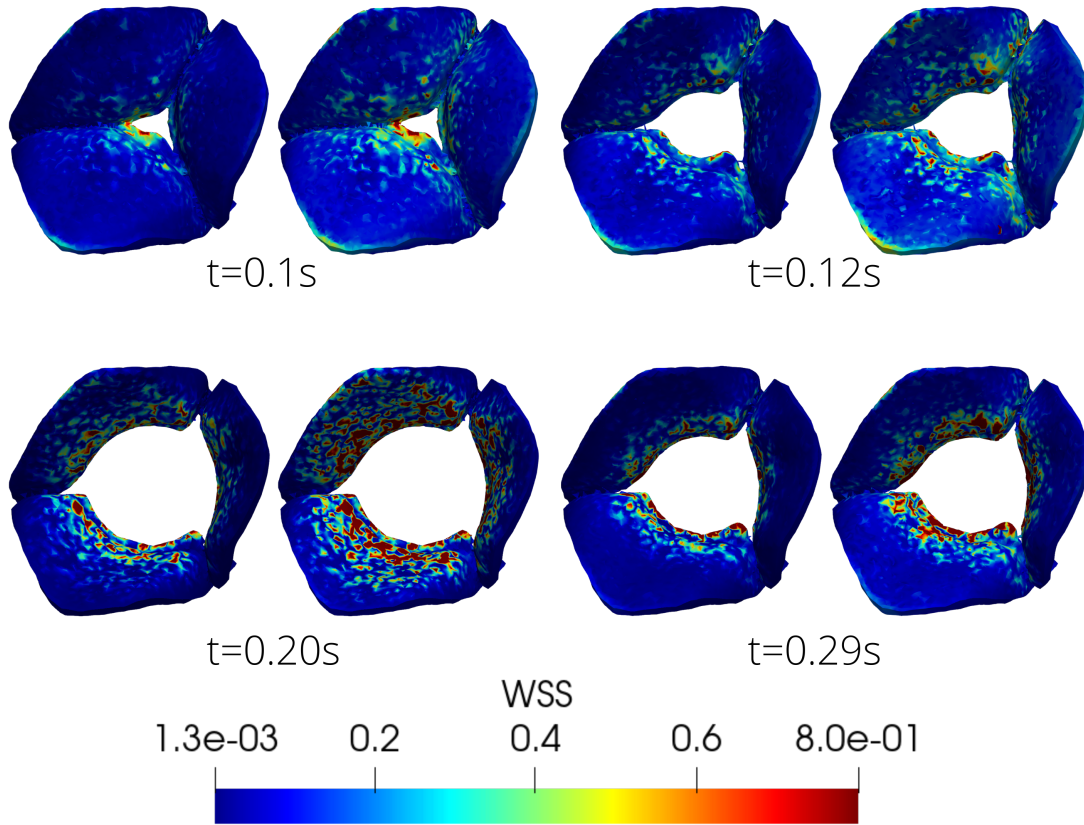


Figure 4.26: Comparison with Newtonian (left) and non-Newtonian (right) magnitude of the wall shear stress on the aortic valve for stenotic configurations on four different time steps: during the first stage of the valve opening (0.1 s), in the middle of the opening phase (0.13 s), when the valve is completely open (0.20 s) and closing phase (0.29 s).

Finally, Figure 4.25 and Figure 4.26 show the magnitude of WSS computed at different time steps on the “wall” of the valve, respectively for the regurgitant and stenotic configurations. In this case, due to the RIIS method, there is no physical wall, but we considered as wall the limit part where the resistive term has action (thus, at distance $\pm\varepsilon$ from the valve). Even if the numerical values are not rigorous as in the previous case because of the mentioned approximation, the difference in accuracy should be similar for the two rheological models. Even in this case we can see how the WSS is generally higher in the non-Newtonian case for both configurations, when the valve is completely open. It is interesting to observe the high value of WSS reached during regurgitation (Figure 4.25 at $t = 0.20\text{ s}$), as could be expected because of the high flow rate passing through the valve at this moment of the simulation.

5 | Conclusions and further development

In this work, we investigated the mathematical modeling of the aortic valve. The clinical motivation for this work stems from the millions of patients annually diagnosed with pathologies of the aortic valve.

The purpose of the thesis was twofold. First, we investigated the coupling of the RIIS method with the momentum balance on the leaflets as 0D equation, for blood-valve FSI. This method could drastically improve the computational performance of the simulation with respect to other popular approaches used in the literature, which require a full 3D representation of the valve geometry and of its mechanics solver. At the same time, this method is able to retain a physical meaning for the parameters of the 0D equations. The aim was to understand the role of the different parameters of the model and calibrate them to reproduce different physiological scenarios. In particular, we investigated the healthy configuration and two configurations related to the two most common pathological cases related to a malfunctioning of the valve: stenosis and regurgitation. Second, we complemented the FSI model with a non-Newtonian model for blood rheology, with the purpose of assessing the impact of the blood rheology on the valve dynamics and on blood flow. The non-Newtonian model was implemented in `lifex`: a high-performance library for the solution of multi-physics and multiscale problems, mainly for cardiac applications. As discussed in Section 1.6.1, no studies can be found in the literature concerning the usage of a non-Newtonian model in proximity of a physiological trileaflet valve: with this work we tried to fill this gap.

First, we presented the mathematical and numerical methods used to model the FSI-nature of the problem and the non-Newtonian rheology of blood (see Chapter 2). Then, we performed the validation of the non-Newtonian model, by comparing it with the literature on a simple geometry (see Chapter 3). Finally, we presented the results of the simulation in proximity of the aortic valve (see Chapter 4). The healthy configuration was proved to be in accordance with most of the physiological parameters measured in the literature during

the systole, such as the duration of the opening and closing phases, transvalvular pressure difference, and the general dynamic of the valve and of blood flow (see Section 4.2). In this sense, this could be considered an improvement with respect to [49], where the opening phase was a lot shorter than what is physiologically observed, and to [56] where only the opening stage was investigated. We investigated a stenotic and a regurgitant valve, characterized by different values of the elasticity coefficient of the reduced valve model. Then, these configurations were investigated and compared with the healthy case (see Section 4.3). In the stenotic case, we observed a reduced orifice area, a shorter time interval in which blood flow is allowed through the valve and a stronger aortic jet, with larger vorticity structures, when the valve reaches its maximum orifice area and during the closure. In the regurgitant case, we showed that a delaying in the beginning of the valve closing phase induces regurgitation, and that regurgitation affects the blood dynamics mostly in the closing phase. Finally, the comparison between the Newtonian and non-Newtonian rheology was carried out for the two pathological configurations (see Section 4.4). Our results confirmed that the rheological model has only little influence on quantities such as valve dynamics, transvalvular pressure drop and large-scale flow structure: this is in accordance with what can be found in literature, even if a different type of valve and model were considered. Significant differences, instead, could be observed in the wall shear stress. In particular, considering a Newtonian blood rheology leads to an underestimation of the wall shear stress. This quantity has great importance in the medical field, due to its relation with the formation of plaque in atherosclerosis and with wall wearing and possible tearing. We thus conclude that the non-Newtonian rheology of blood must be taken into account whenever wall shear stress is in the focus of the clinical investigation.

The main limitation in this thesis is in the study of the period after the closure of the valve, when, due to geometrical inconsistencies, some reverse flow can be observed when the valve should be closed. As mentioned in Section 4.2, this issue could be overcome by manually adjusting the valve and aortic root geometries to improve their consistency. We remark that a proper recalibration of the parameters of the model should be done afterward. Other limitations are induced by the choice of the model itself. For example, although the reduced 0D model for the valve induces a reduction in the computational time required for the simulation, it should be considered that this can cause a loss in the accuracy of the model with respect to 3D coupling of the valve.

Further developments of this work can be carried out in multiple directions:

- Concerning the rheology of blood, other types of non-Newtonian models could be investigated. Other generalized non-Newtonian models such as Power Law [87],

Carreau-Yasuda [64] and Casson [134] could be studied to assess the differences in the quantities of interest, such as valve dynamic, pressure jump and wall shear stress. Moreover, more complicated models could be analyzed, such as viscoelastic models [7], in order to take into account the elastic properties of the blood together with the viscous properties.

- A wider domain of investigation, for example including the left ventricle, instead of the flow extension of the domain, used for simplicity in this thesis, could be analyzed in order to conduct a more complete simulation and observe the differences caused by the non-Newtonian model also in the left ventricle.
- The compliance of the aortic wall could be taken into account. Indeed, to improve the accuracy of the results, particularly on the wall shear stress, interactions between the blood and the aortic wall should be considered [135].
- Finally, this computational framework could be applied to a patient-specific geometry and data as in [49]. Indeed, variability among different patients can be captured only considering the patient-specific aortic geometry and the patient-specific leaflets in the correct position.

Bibliography

- [1] Vmtk. URL <http://www.vmtk.org>.
- [2] Zygote. URL <https://www.zygote.com>.
- [3] Blood composition. URL <https://www.freepik.com/>.
- [4] The deal.ii finite element library. URL <https://www.dealii.org>.
- [5] lifex. URL <https://lifex.gitlab.io>.
- [6] World health organization. URL <https://www.who.int>.
- [7] A. Ramiar, M.M. Larimi, A.A. Ranjbar. Investigation of blood flow rheology using second-grade viscoelastic model (phan-thien-tanner) within carotid artery. *Bioeng Biomech.*, 19:27–41, 2017.
- [8] S. S. Abbas, M. S. Nasif, M. A. M. Said, and R. Al-Waked. Numerical simulation of the non-Newtonian blood flow through aortic bileaflet mechanical heart valve using fluid-structure interaction approach. *AIP Conference Proceedings*, 2035(1):070003, 2018. doi: 10.1063/1.5075593.
- [9] P. Africa, R. Piersanti, M. Fedele, L. Dede, and A. Quarteroni. lifex - heart module: a high-performance simulator for the cardiac function - package 1: Fiber generation. 01 2022. doi: 10.5281/zenodo.5810269.
- [10] N. S. Akbar and S. Nadeem. Carreau fluid model for blood flow through a tapered artery with a stenosis. *Ain Shams Engineering Journal*, 5(4):1307–1316, 2014. ISSN 2090-4479. doi: <https://doi.org/10.1016/j.asej.2014.05.010>.
- [11] M. G. Al-Azawy, A. Turan, and A. J. Revell. Investigating the impact of non-Newtonian blood models within a heart pump. *International Journal for Numerical Methods in Biomedical Engineering*, 33:e02780, 2017.
- [12] F. Alauzet, B. Fabrèges, M. A. Fernández, and M. Landajuela. Nitsche-xfem for the coupling of an incompressible fluid with immersed thin-walled structures. *Computer*

- Methods in Applied Mechanics and Engineering*, 301:300–335, 2016. ISSN 0045-7825. doi: <https://doi.org/10.1016/j.cma.2015.12.015>.
- [13] A. Arzani. Accounting for residence-time in blood rheology models: do we really need non-Newtonian blood flow modelling in large arteries? *Journal of The Royal Society Interface*, 15(146):20180486, 2018. doi: 10.1098/rsif.2018.0486.
 - [14] M. Astorino, J. Hamers, S. Shadden, and J.-F. Gerbeau. A robust and efficient valve model based on resistive immersed surfaces. *International journal for numerical methods in biomedical engineering*, 28:937–59, 09 2012. doi: 10.1002/cnm.2474.
 - [15] Y. Bazilevs, V. Calo, J. Cottrell, T. Hughes, A. Reali, and G. Scovazzi. Variational multiscale residual-based turbulence modeling for large eddy simulation of incompressible flows. *Computer Methods in Applied Mechanics and Engineering*, 197(1): 173–201, 2007. ISSN 0045-7825. doi: <https://doi.org/10.1016/j.cma.2007.07.016>.
 - [16] J. Benitez, D. Fontanarosa, J. Wang, P. Paritala, T. McGahan, T. Lloyd, and Z. Li. The importance of blood rheology in patient-specific computational fluid dynamics simulation of stenotic carotid arteries. *Biomechanics and Modeling in Mechanobiology*, 19, 10 2020. doi: 10.1007/s10237-019-01282-7.
 - [17] L. Bennati, C. Vergara, M. Domanin, C. Malloggi, D. Bissacco, S. Trimarchi, V. Silani, G. Parati, and R. Casana. A computational fluid–structure interaction study for carotids with different atherosclerotic plaques. *Journal of Biomechanical Engineering*, 143, 04 2021. doi: 10.1115/1.4050910.
 - [18] L. C. Berselli, P. Miloro, A. Menciassi, and E. Sinibaldi. Exact solution to the inverse Womersley problem for pulsatile flows in cylindrical vessels, with application to magnetic particle targeting. *Applied Mathematics and Computations*, 219:5717–5729, 2013.
 - [19] P. Blanco and R. Feijóo. A 3d-1d-0d computational model for the entire cardiovascular system. 09 2009.
 - [20] I. Borazjani. Fluid–structure interaction, immersed boundary-finite element method simulations of bio-prosthetic heart valves. *Computer Methods in Applied Mechanics and Engineering*, 257:103–116, 2013.
 - [21] I. Borazjani, L. Ge, and F. Sotiropoulos. High-resolution fluid-structure interaction simulations of flow through a bi-leaflet mechanical heart valve in an anatomic aorta. *Ann Biomed Eng.*, 38:326–344, 2010.

- [22] M. Bucelli, L. Dede', A. Quarteroni, and C. Vergara. Partitioned and monolithic algorithms for the numerical solution of cardiac fluid-structure interaction. *MOX*.
- [23] E. Burman and M. A. Fernández. An unfitted nitsche method for incompressible fluid-structure interaction using overlapping meshes. *Computer Methods in Applied Mechanics and Engineering*, 279:497–514, 2014. ISSN 0045-7825. doi: <https://doi.org/10.1016/j.cma.2014.07.007>.
- [24] G. C. Buscaglia and R. F. Ausas. Variational formulations for surface tension, capillarity and wetting. *Computer Methods in Applied Mechanics and Engineering*, 200(45):3011–3025, 2011. ISSN 0045-7825. doi: <https://doi.org/10.1016/j.cma.2011.06.002>.
- [25] A. Caballero and S. Laín. A review on computational fluid dynamics modelling in human thoracic aorta. *Cardiovascular Engineering and Technology*, 4:103–130, 2013.
- [26] B. A. Carabello and W. J. Paulus. Aortic stenosis. *The Lancet*, 373(9667):956–966, 2009. ISSN 0140-6736. doi: [https://doi.org/10.1016/S0140-6736\(09\)60211-7](https://doi.org/10.1016/S0140-6736(09)60211-7).
- [27] Y. Çengel and J. Cimbala. *Fluid Mechanics: Fundamentals and Applications*. McGraw-Hill series in mechanical engineering. McGraw-HillHigher Education, 2006. ISBN 9780073044651.
- [28] R. R. Chamley, D. A. Holdsworth, K. Rajappan, and E. D. Nicol. ECG interpretation: Interpretation of the ECG in young, fit, asymptomatic individuals undertaking high-hazard occupations is the topic of the fourth article in the occupational cardiology series. *European Heart Journal*, 40(32):2663–2666, 08 2019. ISSN 0195-668X. doi: [10.1093/eurheartj/ehz559](https://doi.org/10.1093/eurheartj/ehz559).
- [29] K. B. Chandran and S. C. Vigmostad. Patient-specific bicuspid valve dynamics: overview of methods and challenges. *Journal of biomechanics*, 46 2:208–16, 2013.
- [30] E. Charitos and H.-H. Sievers. Anatomy of the aortic root: implications for valve-sparing surgery. *Annals of cardiothoracic surgery*, 2:53–6, 08 2013. doi: [10.3978/j.issn.2225-319X.2012.11.18](https://doi.org/10.3978/j.issn.2225-319X.2012.11.18).
- [31] P. Chaturani and V. Palanisamy. Pulsatile flow of blood with periodic body acceleration. *Int. J. Eng. Sci.*, 29(1):113–121, Jan. 1991.
- [32] J. Chen, X.-Y. Lu, and W. Wang. Non-newtonian effects of blood flow on hemodynamics in distal vascular graft anastomoses. *Journal of biomechanics*, 39:1983–95, 02 2006. doi: [10.1016/j.jbiomech.2005.06.012](https://doi.org/10.1016/j.jbiomech.2005.06.012).

- [33] Y. Cheng, H. Oertel, and T. Schenkel. Fluid-structure coupled CFD simulation of the left ventricular flow during filling phase. *Annals of Biomedical Engineering*, 33(5):567–576, 2005.
- [34] Y. I. Cho and K. R. Kensey. Effects of the non-Newtonian viscosity of blood on flows in a diseased arterial vessel. part 1: Steady flows. *Biorheology*, 28(3-4):241–62, 1991.
- [35] C. A. Conti, A. Della Corte, E. Votta, L. Del Viscovo, C. Bancone, L. S. De Santo, and A. Redaelli. Biomechanical implications of the congenital bicuspid aortic valve: A finite element study of aortic root function from in vivo data. *The Journal of Thoracic and Cardiovascular Surgery*, 140(4):890–896.e2, 2010.
- [36] J. D. Cutnell and K. W. Johnson. *Physics*. New York: Wiley, 1998.
- [37] J. De Hart, G. Peters, P. Schreurs, and F. Baaijens. A two-dimensional fluid–structure interaction model of the aortic valve. *Journal of Biomechanics*, 33(9):1079–1088, 2000.
- [38] J. De Hart, G. Peters, P. Schreurs, and F. Baaijens. A three-dimensional computational analysis of fluid–structure interaction in the aortic valve. *Journal of Biomechanics*, 36(1):103–112, 2003. ISSN 0021-9290. doi: [https://doi.org/10.1016/S0021-9290\(02\)00244-0](https://doi.org/10.1016/S0021-9290(02)00244-0).
- [39] F. De Vita, M. D. de Tullio, and R. Verzicco. Numerical simulation of the non-Newtonian blood flow through a mechanical aortic valve. Non-Newtonian blood flow in the aortic root. *Theoretical and Computational Fluid Dynamics*, 30(1-2):129–138, Apr. 2016. doi: 10.1007/s00162-015-0369-2.
- [40] M. C. Delfour and J.-P. Zolésio. Shapes and geometries - metrics, analysis, differential calculus, and optimization, second edition. In *Advances in design and control*, 2011.
- [41] S. Deparis, G. Grandperrin, and A. Quarteroni. Parallel preconditioners for the unsteady Navier–Stokes equations and applications to hemodynamics simulations. *Computers & Fluids*, 92:253–273, 2014. ISSN 0045-7930. doi: <https://doi.org/10.1016/j.compfluid.2013.10.034>.
- [42] E. G. Dimond and A. Benchimol. Phonocardiography. *California medicine*, 94(3):139–146, 1961.
- [43] F. Domenichini and G. Pedrizzetti. Asymptotic model of fluid–tissue interaction

- for mitral valve dynamics. *Cardiovascular Engineering and Technology*, 6:95–104, 06 2015. doi: 10.1007/s13239-014-0201-y.
- [44] S. N. Doost, L. Zhong, B. Su, and Y. Y. Morsi. The numerical analysis of non-Newtonian blood flow in human patient-specific left ventricle. *Computer Methods and Programs in Biomedicine*, 127, 01 2016. doi: 10.1016/j.cmpb.2015.12.020.
- [45] R. L. Drake, A. W. Vogl, and A. W. M. Mitchell. *Gray's anatomy for students*. Elsevier, 2020.
- [46] K. Durairaj, R. Vinoth, A. Raviraj, and C. Shankar. Non-Newtonian and Newtonian blood flow in human aorta: A transient analysis. *Biomedical Research (India)*, 28: 3194–3203, 01 2017.
- [47] E. Nader, S. Skinner, M. Romana et al. Blood rheology: Key parameters, impact on blood flow, role in sickle cell disease and effects of exercise. *Frontiers in Physiology*, 2019.
- [48] E. Faggiano, L. Antiga, G. Puppini, A. Quarteroni, G. B. Luciani, and C. Vergara. Helical flows and asymmetry of blood jet in dilated ascending aorta with normally functioning bicuspid valve. *Biomechanics and modeling in mechanobiology*, 12, 10 2012.
- [49] M. Fedele, E. Faggiano, L. Dede, and A. Quarteroni. A patient-specific aortic valve model based on moving resistive immersed implicit surfaces. *Biomechanics and modeling in mechanobiology*, 16:1779–1803, 10 2017. doi: 10.1007/s10237-017-0919-1.
- [50] D. Fedosov, W. Pan, B. Caswell, G. Gompper, and G. Karniadakis. Predicting human blood viscosity in silico. *Proceedings of the National Academy of Sciences of the United States of America*, 108:11772–7, 07 2011. doi: 10.1073/pnas.1101210108.
- [51] M. Fernández, J.-F. Gerbeau, and V. Martin. Numerical simulation of blood flows through a porous interface. <http://dx.doi.org/10.1051/m2an:2008031>, 42, 11 2008. doi: 10.1051/m2an:2008031.
- [52] G. A. Fishbein and M. C. Fishbein. Pathology of the aortic valve: Aortic valve stenosis/aortic regurgitation. *Current Cardiology Reports*, 21(8):1226–1233, July 2019. doi: <https://doi.org/10.1007/s11886-019-1162-4>.
- [53] M. Fok, M. Shaw, E. Sancho, D. Abello, and M. Bashir. Aortic valve repair: A systematic review and meta-analysis of published literature. *Aorta (Stamford, Conn)*, 2:10–21, 2014. doi: <https://doi.org/10.12945/j.aorta.2014.14-003>.

- [54] L. Formaggia, C. Vergara, and S. Zonca. Unfitted extended finite elements for composite grids. *Computers & Mathematics with Applications*, 76(4):893–904, 2018. ISSN 0898-1221. doi: <https://doi.org/10.1016/j.camwa.2018.05.028>.
- [55] D. Forti and L. Dedè. Semi-implicit BDF time discretization of the Navier–Stokes equations with VMS-LES modeling in a High Performance Computing framework. *Computers & Fluids*, 117:168–182, 2015. ISSN 0045-7930. doi: <https://doi.org/10.1016/j.compfluid.2015.05.011>.
- [56] I. Fumagalli. A reduced 3d-0d fsi model of the aortic valve including leaflets curvature. *arXiv*, 01 2021.
- [57] I. Fumagalli, N. Parolini, and M. Verani. On a free-surface problem with moving contact line: From variational principles to stable numerical approximations. *Journal of Computational Physics*, 355:253–284, 2018. ISSN 0021-9991. doi: <https://doi.org/10.1016/j.jcp.2017.11.004>.
- [58] Y. C. Fung. Biomechanics: Circulation. 1997.
- [59] L. Ge and F. Sotiropoulos. A numerical method for solving the 3d unsteady incompressible Navier–Stokes equations in curvilinear domains with complex immersed boundaries. *Journal of Computational Physics*, 225(2):1782–1809, 2007.
- [60] L. Ge and F. Sotiropoulos. Direction and magnitude of blood flow shear stresses on the leaflets of aortic valves: is there a link with valve calcification? *J Biomech Eng.*, 132(1), 2010.
- [61] A. Gerstenberger and W. Wall. An embedded dirichlet formulation for 3d continua. *International Journal for Numerical Methods in Engineering*, 82:537 – 563, 01 2009. doi: 10.1002/nme.2755.
- [62] A. Gerstenberger and W. A. Wall. An extended finite element method/lagrange multiplier based approach for fluid–structure interaction. *Computer Methods in Applied Mechanics and Engineering*, 197(19):1699–1714, 2008. ISSN 0045-7825. doi: <https://doi.org/10.1016/j.cma.2007.07.002>. Computational Methods in Fluid–Structure Interaction.
- [63] B. Griffith. Immersed boundary model of aortic heart valve dynamics with physiological driving and loading conditions. *Int J Numer Meth Biomed Eng*, 28(3):317–345, 2012.
- [64] B. Guerciotti and C. Vergara. Computational comparison between Newtonian and non-Newtonian blood rheologies in stenotic vessels. 2016.

- [65] J. E. Hall. *Guyton and hall textbook of medical physiology*. W B Saunders, London, 2015.
- [66] M. Handke, G. Heinrichs, F. Beyersdorf, M. Olschewski, C. Bode, and A. Geibel. In vivo analysis of aortic valve dynamics by transesophageal 3-dimensional echocardiography with high temporal resolution. *The Journal of Thoracic and Cardiovascular Surgery*, 125(6):1412–1419, 2003. ISSN 0022-5223. doi: [https://doi.org/10.1016/S0022-5223\(02\)73604-0](https://doi.org/10.1016/S0022-5223(02)73604-0).
- [67] P. Hansbo, M. G. Larson, and S. Zahedi. Characteristic cut finite element methods for convection-diffusion problems on time dependent surfaces. *Computer Methods in Applied Mechanics and Engineering*, 293:431–461, 2015. ISSN 0045-7825. doi: <https://doi.org/10.1016/j.cma.2015.05.010>.
- [68] T. Hofmann, W. Kasper, T. Meinertz, G. Spillner, V. Schlosser, and H. Just. Determination of aortic valve orifice area in aortic valve stenosis by two-dimensional transesophageal echocardiography. *The American Journal of Cardiology*, 59(4):330–335, 1987. ISSN 0002-9149. doi: [https://doi.org/10.1016/0002-9149\(87\)90808-3](https://doi.org/10.1016/0002-9149(87)90808-3).
- [69] V. Honzlová-Exnerová, J. Malý, and O. Martio. AM -modulus and Hausdorff measure of codimension one in metric measure spaces. *Mathematische Nachrichten*, 295, 01 2022. doi: 10.1002/mana.202000059.
- [70] M.-C. Hsu, D. Kamensky, Y. Bazilevs, M. Sacks, and T. Hughes. Fluid-structure interaction analysis of bioprosthetic heart valves: Significance of arterial wall deformation. *Computational mechanics*, 54:1055–1071, 10 2014. doi: 10.1007/s00466-014-1059-4.
- [71] J. Hunt, A. Wray, and P. Moin. Eddies, streams, and convergence zones in turbulent flows. *Studying Turbulence Using Numerical Simulation Databases*, -1:193–208, 11 1988.
- [72] J. Biasetti, T. C. Gasser, M. Auer, U. Hedin, F. Labruto. Hemodynamics of the normal aorta compared to fusiform and saccular abdominal aortic aneurysms with emphasis on a potential thrombus formation mechanism. *Annals of Biomedical Engineering*, 2009.
- [73] J. Boyd, J. M. Buick, S. Green. Analysis of the Casson and Carreau-Yasuda non-Newtonian blood models in steady and oscillatory flow using the lattice Boltzmann method. *Physics of Fluids*, 2007.
- [74] M. Jahangiri, M. Saghafian, and M. Sadeghi. Effect of six non-Newtonian viscosity

- models on hemodynamic parameters of pulsatile blood flow in stenosed artery. *Journal of Computational and Applied Research in Mechanical Engineering (JCARME)*, 7, 01 2018. doi: 10.22061/jcarme.2017.1433.1114.
- [75] J. Janela, A. Moura, and A. Sequeira. A 3d non-Newtonian fluid–structure interaction model for blood flow in arteries. *Journal of Computational and Applied Mathematics*, 234(9):2783–2791, 2010. ISSN 0377-0427. doi: <https://doi.org/10.1016/j.cam.2010.01.032>. Third International Workshop on Analysis and Numerical Approximation of Singular Problems [IWANASP08].
- [76] O. Jones. The valves of the heart, 2017. URL <https://teachmeanatomy.info/thorax/organs/heart/hearts-valves/>.
- [77] D. Kamensky, M.-C. Hsu, D. Schillinger, J. A. Evans, A. Aggarwal, Y. Bazilevs, M. S. Sacks, and T. J. Hughes. An immersogeometric variational framework for fluid–structure interaction: Application to bioprosthetic heart valves. *Computer Methods in Applied Mechanics and Engineering*, 284:1005–1053, 2015. ISSN 0045-7825. doi: <https://doi.org/10.1016/j.cma.2014.10.040>. Isogeometric Analysis Special Issue.
- [78] D. L. Kasper, A. S. Fauci, S. L. Hauser, D. L. Longo, J. L. Jameson, and J. Loscalzo. *Harrison’s principles of internal medicine (19th edition.)*. McGraw Hill Education, New York, 2015.
- [79] D. Katritsis, L. Kaiktsis, A. Chaniotis, J. Pantos, E. P. Efstatopoulos, and V. Marmarlis. Wall shear stress: Theoretical considerations and methods of measurement. *Progress in Cardiovascular Diseases*, 49(5):307–329, 2007. ISSN 0033-0620. doi: <https://doi.org/10.1016/j.pcad.2006.11.001>. Special Articles.
- [80] T. Korakianitis and Y. Shi. Numerical simulation of cardiovascular dynamics with healthy and diseased heart valves. *Journal of Biomechanics*, 39(11):1964–1982, 2006. ISSN 0021-9290. doi: <https://doi.org/10.1016/j.jbiomech.2005.06.016>.
- [81] D. N. Ku, D. P. Giddens, C. K. Zarins, and S. Glagov. Pulsatile flow and atherosclerosis in the human carotid bifurcation: Positive correlation between plaque location and low and oscillating shear stress. *Arteriosclerosis, Thrombosis, and Vascular Biology*, 5:293–302, 1985.
- [82] T. B. Le and F. Sotiropoulos. Fluid–structure interaction of an aortic heart valve prosthesis driven by an animated anatomic left ventricle. *Journal of Computational Physics*, 244:41–62, 2013.

- [83] R. G. Leyh, C. Schmidtke, H.-H. Sievers, and M. H. Yacoub. Opening and closing characteristics of the aortic valve after different types of valve-preserving surgery. *Circulation*, 100(21):2153–60, 1999.
- [84] X. Liu, Y. Fan, X. Deng, and F. Zhan. Effect of non-Newtonian and pulsatile blood flow on mass transport in the human aorta. *Journal of biomechanics*, 44:1123–31, 02 2011. doi: 10.1016/j.jbiomech.2011.01.024.
- [85] X. Liu, Z. Wang, P. Zhao, Z. Fan, A. Sun, F. Zhan, Y. Fan, and X. Deng. Nitric oxide transport in normal human thoracic aorta: Effects of hemodynamics and nitric oxide scavengers. *PloS one*, 9:e112395, 11 2014. doi: 10.1371/journal.pone.0112395.
- [86] Z. Lou and W.-J. Yang. A computer simulation of the non-Newtonian blood flow at the aortic bifurcation. *Journal of Biomechanics*, 26(1):37–49, 1993. ISSN 0021-9290. doi: [https://doi.org/10.1016/0021-9290\(93\)90611-H](https://doi.org/10.1016/0021-9290(93)90611-H).
- [87] M. Hussain, S. Kar, R.R. Puniyani. Relationship between power law coefficients and major blood constituents affecting the whole blood viscosity. *Journal of Biosciences*, 24:329–337, 1999.
- [88] R. Mahmood, S. Bilal, I. Khan, N. Kousar, A. H. Seikh, and E.-S. M. Sherif. A comprehensive finite element examination of Carreau Yasuda fluid model in a lid driven cavity and channel with obstacle by way of kinetic energy and drag and lift coefficient measurements. *Journal of Materials Research and Technology*, 9(2): 1785–1800, 2020. ISSN 2238-7854. doi: <https://doi.org/10.1016/j.jmrt.2019.12.010>.
- [89] J. Marn, J. Iljaž, Z. Žunič, and P. Ternik. Non-Newtonian blood flow around healthy and regurgitated aortic valve with coronary blood flow involved. *Strojniški vestnik - Journal of Mechanical Engineering*, 58(7-8):482–491, 2012. ISSN 0039-2480. doi: 10.5545/sv-jme.2010.023.
- [90] G. Marom, H.-S. Kim, M. Rosenfeld, E. Raanani, and R. Haj-Ali. Fully coupled fluid-structure interaction model of congenital bicuspid aortic valves: Effect of asymmetry on hemodynamics. *Medical and biological engineering and computing*, 51, 03 2013.
- [91] A. Massing, M. Larson, A. Logg, and M. Rognes. A nitsche-based cut finite element method for a fluid–structure interaction problem. *Communications in Applied Mathematics and Computational Science*, 10, 11 2013. doi: 10.2140/camcos.2015.10.97.
- [92] U. Mayer, A. Popp, A. Gerstenberger, and W. Wall. 3d fluid-structure-contact

- interaction based on a combined XFEM FSI and dual mortar contact approach. *Computational Mechanics*, 46:53–67, 06 2010. doi: 10.1007/s00466-010-0486-0.
- [93] V. Meschini and R. Mittal. Systolic anterior motion in hypertrophic cardiomyopathy: a fluid–structure interaction computational model. *Theoretical and Computational Fluid Dynamics*, 35:1–16, 06 2021. doi: 10.1007/s00162-021-00564-0.
- [94] A. M. Mirza, A. Barreto, T. Boodooram, and S. Ramaswamy. Importance of non-Newtonian modeling of blood flow for calcified aortic valves: Relevance to sub-clinical thrombosis. *Structural Heart*, 5(sup1):30–30, 2021. doi: 10.1080/24748706.2021.1901539.
- [95] A. Moerman, S. Korteland, K. Dilba, K. Gaalen, D. Poot, A. Lugt, H. Verhagen, J. Wentzel, A. van der Steen, F. Gijsen, and K. Van der Heiden. The correlation between wall shear stress and plaque composition in advanced human carotid atherosclerosis. *Frontiers in Bioengineering and Biotechnology*, 9, 01 2022. doi: 10.3389/fbioe.2021.828577.
- [96] U. Morbiducci, D. Gallo, D. Massai, R. Ponzini, M. A. Deriu, L. Antiga, A. Redaelli, and F. M. Montevercchi. On the importance of blood rheology for bulk flow in hemodynamic models of the carotid bifurcation. *Journal of Biomechanics*, 44(13):2427–2438, 2011. ISSN 0021-9290. doi: <https://doi.org/10.1016/j.jbiomech.2011.06.028>.
- [97] Y. Y. Morsi, W. Yang, C. Wong, and S. Das. Transient fluid-structure coupling for simulation of a trileaflet heart valve using weak coupling. *Journal of artificial organs : the official journal of the Japanese Society for Artificial Organs*, 10:96–103, 02 2007.
- [98] D. Mozaffarian et al. Heart disease and stroke statistics-2016 update a report from the american heart association. *Circulation*, 133(4):e38–e48, Jan. 2016. ISSN 0009-7322. doi: 10.1161/CIR.0000000000000350.
- [99] S. Nadeem, N. S. Akbar, A. A. Hendi, and T. Hayat. Power law fluid model for blood flow through a tapered artery with a stenosis. *Applied Mathematics and Computation*, 217(17):7108–7116, 2011. ISSN 0096-3003. doi: <https://doi.org/10.1016/j.amc.2011.01.026>.
- [100] D. Nordsletten, M. McCormick, P. Kilner, P. Hunter, D. Kay, and N. Smith. Fluid–solid coupling for the investigation of diastolic and systolic human left ventricular function. *International Journal for Numerical Methods in Biomedical Engineering*, 27:1017 – 1039, 07 2011. doi: 10.1002/cnm.1405.

- [101] S. Osher and R. P. Fedkiw. Level set methods: An overview and some recent results. *Journal of Computational Physics*, 169(2):463–502, 2001. ISSN 0021-9991. doi: <https://doi.org/10.1006/jcph.2000.6636>.
- [102] S. Pasta, A. Rinaudo, A. Luca, M. Pilato, C. Scardulla, T. Gleason, and D. Vorp. Difference in hemodynamic and wall stress of ascending thoracic aortic aneurysms with bicuspid and tricuspid aortic valve. *Journal of biomechanics*, 46, 05 2013.
- [103] J. Paszkowiak and A. Dardik. Arterial wall shear stress: Observations from the bench to the bedside. *Vascular and endovascular surgery*, 37:47–57, 01 2003. doi: 10.1177/153857440303700107.
- [104] T. J. Pedley. The fluid mechanics of large blood vessels. 1980.
- [105] K. Perktold, R. Peter, M. Resch, and G. Langs. Pulsatile non-Newtonian blood flow in three-dimensional carotid bifurcation models: a numerical study of flow phenomena under different bifurcation angles. *Journal of Biomedical Engineering*, 13(6):507–515, 1991. ISSN 0141-5425. doi: [https://doi.org/10.1016/0141-5425\(91\)90100-L](https://doi.org/10.1016/0141-5425(91)90100-L).
- [106] C. S. Peskin. Flow patterns around heart valves: A numerical method. *Journal of Computational Physics*, 10(2):252–271, 1972.
- [107] C. S. Peskin. The immersed boundary method. *Acta Numerica*, 11:479–517, 2002.
- [108] A. Pick. Aortic stenosis: Symptoms, diagnosis & treatment. URL <https://www.heart-valve-surgery.com/aortic-stenosis-valve-heart-narrowing.php>.
- [109] R. Ponagalagusamy and R. Tamil Selvi. A study on two-layered model (Casson–Newtonian) for blood flow through an arterial stenosis: Axially variable slip velocity at the wall. *Journal of the Franklin Institute*, 348(9):2308–2321, 2011. ISSN 0016-0032. doi: <https://doi.org/10.1016/j.jfranklin.2011.06.020>.
- [110] Y. Pratumwal, W. Limtrakarn, S. Muengtaweepongsa, P. Phakdeesan, S. Duangburong, P. Eiamaram, and K. Intharakham. Whole blood viscosity modeling using power law, Casson, and Carreau Yasuda models integrated with image scanning U-tube viscometer technique. *Songklanakarin Journal of Science and Technology*, 39:625–631, 09 2017. doi: 10.14456/sjst-psu.2017.77.
- [111] A. Quarteroni. *Numerical models for differential problems*, volume 16 of *Modeling, Simulation & Applications*. Springer, Cham, third edition, 2020. doi: 10.1007/978-3-319-49316-9.

- [112] A. Quarteroni, L. Dede', A. Manzoni, and C. Vergara. *Mathematical Modelling of the Human Cardiovascular System: Data, Numerical Approximation, Clinical Applications*. Cambridge Monographs on Applied and Computational Mathematics. Cambridge University Press, 2019. doi: 10.1017/9781108616096.
- [113] F. Regazzoni, M. Salvador, P. Africa, M. Fedele, L. Dedè, and A. Quarteroni. A cardiac electromechanical model coupled with a lumped-parameter model for closed-loop blood circulation. *Journal of Computational Physics*, 457:111083, 2022. ISSN 0021-9991. doi: <https://doi.org/10.1016/j.jcp.2022.111083>.
- [114] A. Rinaudo and S. Pasta. Regional variation of wall shear stress in ascending thoracic aortic aneurysms. *Proceedings of the Institution of Mechanical Engineers. Part H, Journal of engineering in medicine*, 228, 06 2014. doi: 10.1177/0954411914540877.
- [115] Y. Sahasakul, W. D. Edwards, J. M. Naessens, and A. Tajik. Age-related changes in aortic and mitral valve thickness: Implications for two-dimensional echocardiography based on an autopsy study of 200 normal human hearts. *The American Journal of Cardiology*, 62(7):424–430, 1988. ISSN 0002-9149. doi: [https://doi.org/10.1016/0002-9149\(88\)90971-X](https://doi.org/10.1016/0002-9149(88)90971-X).
- [116] S. Salsa. Partial differential equations in action - from modelling to theory. 2008.
- [117] C. Schmidtke, H.-H. Sievers, A. Frydrychowicz, M. Petersen, M. Scharfschwerdt, A. Karluss, U. Stierle, and D. Richardt. First clinical results with the new sinus prosthesis used for valve-sparing aortic root replacement. *European Journal of Cardio-Thoracic Surgery*, 43:585–90, 03 2013. doi: 10.1093/ejcts/ezs318.
- [118] B. Schott, C. Ager, and W. Wall. Monolithic cut finite element based approaches for fluid-structure interaction. *International Journal for Numerical Methods in Engineering*, 119, 03 2019. doi: 10.1002/nme.6072.
- [119] J.-H. Seo, C. Zhu, J. Resar, and R. Mittal. Flow physics of normal and abnormal bioprosthetic aortic valves. *International Journal of Heat and Fluid Flow*, 86:108740, 2020. ISSN 0142-727X. doi: <https://doi.org/10.1016/j.ijheatfluidflow.2020.108740>.
- [120] D. Shier, J. Butler, and R. Lewis. *Hole's Human Anatomy & Physiology*. Hole's Human Anatomy & Physiology. WCB/McGraw-Hill, 1999. ISBN 9780697341938.
- [121] H.-H. Sievers and C. Schmidtke. A classification system for the bicuspid aortic valve from 304 surgical specimens. *The Journal of Thoracic and Cardiovascular Surgery*,

- 133(5):1226–1233, 2007. ISSN 0022-5223. doi: <https://doi.org/10.1016/j.jtcvs.2007.01.039>.
- [122] F. Sotiropoulos and X. Yang. Immersed boundary methods for simulating fluid–structure interaction. *Progress in Aerospace Sciences*, 65:1–21, 2014.
- [123] M. Souli, A. Ouahsine, and L. Lewin. Ale formulation for fluid–structure interaction problems. *Computer Methods in Applied Mechanics and Engineering*, 190(5):659–675, 2000.
- [124] J. V. Soulis, G. D. Giannoglou, Y. S. Chatzizisis, K. V. Seralidou, G. E. Parcharidis, and G. E. Louridas. Non-newtonian models for molecular viscosity and wall shear stress in a 3d reconstructed human left coronary artery. *Medical Engineering & Physics*, 30(1):9–19, 2008. ISSN 1350-4533. doi: <https://doi.org/10.1016/j.medengphy.2007.02.001>.
- [125] C. Spadaccio, K. Alkhamees, and N. Al-Attar. Recent advances in aortic valve replacement. *Faculty Rev*, 1159, 2019. doi: <https://doi.org/10.12688/f1000research.17995.1>.
- [126] A. Steenhoven, C. Verlaan, P. Veenstra, and R. Reneman. In vivo cinematographic analysis of the aortic valve. *The American journal of physiology*, 240:H286–92, 03 1981. doi: 10.1152/ajpheart.1981.240.2.H286.
- [127] E. Süli and D. F. Mayers. *An Introduction to Numerical Analysis*. Cambridge University Press, 2003. doi: 10.1017/CBO9780511801181.
- [128] S. Tabakova, E. Nikolova, and S. Radev. Carreau model for oscillatory blood flow in a tube. *AIP Conference Proceedings*, 1629, 06 2014. doi: 10.1063/1.4902290.
- [129] T. Tezduyar and S. Sathe. Stabilization parameters in SUPG and PSPG formulations. *Journal of Computational and Applied Mechanics*, 4:71–88, 01 2003.
- [130] M. Thubrikar. *The Aortic Valve*. 05 2018. ISBN 9780203737163. doi: 10.4324/9780203737163.
- [131] K. M. Tse, P. Chiu, H. P. Lee, and P. Ho. Investigation of hemodynamics in the development of dissecting aneurysm within patient-specific dissecting aneurismal aortas using computational fluid dynamics (CFD) simulations. *Journal of Biomechanics*, 44(5):827–836, 2011. ISSN 0021-9290. doi: <https://doi.org/10.1016/j.jbiomech.2010.12.014>.
- [132] F. van de Vosse. Cardiovascular fluid mechanics. 1991.

- [133] R. van Loon, P. Anderson, and F. van de Vosse. A fluid–structure interaction method with solid-rigid contact for heart valve dynamics. *Journal of Computational Physics*, 217(2):806–823, 2006.
- [134] J. Venkatesan, S. Sankar, H. Kola, and Y. Yatim. Mathematical analysis of Casson fluid model for blood rheology in stenosed narrow arteries. *Journal of Applied Mathematics*, 2013, 01 2013. doi: 10.1155/2013/583809.
- [135] E. Vignali, E. Gasparotti, S. Celi, and S. Avril. Fully-coupled FSI computational analyses in the ascending thoracic aorta using patient-specific conditions and anisotropic material properties. *Frontiers in Physiology*, 12:732561, 10 2021. doi: 10.3389/fphys.2021.732561.
- [136] J. Vimmr and A. Jonasova. Non-Newtonian effects of blood flow in complete coronary and femoral bypasses. *Mathematics and Computers in Simulation*, 80:1324–1336, 02 2010. doi: 10.1016/j.matcom.2009.01.004.
- [137] F. Viola, V. Meschini, and R. Verzicco. Fluid–structure-electrophysiology interaction (fsei) in the left-heart: A multi-way coupled computational model. *European Journal of Mechanics - B/Fluids*, 79:212–232, 2020. ISSN 0997-7546. doi: <https://doi.org/10.1016/j.euromechflu.2019.09.006>.
- [138] D. Wendell, M. Samyn, J. Cava, L. Ellwein-Fix, M. Krolikowski, K. Gandy, A. Pelech, S. Shadden, and J. LaDisa. Including aortic valve morphology in computational fluid dynamics simulations: Initial findings and application to aortic coarctation. *Medical engineering & physics*, 35, 08 2012. doi: 10.1016/j.medengphy.2012.07.015.
- [139] P. Wenn and R. Zeltser. Aortic valve disease. *StatPearls*, 2022. doi: <https://doi.org/10.1007/s11886-019-1162-4>.
- [140] C. Wiggers. *Modern Aspects of the Circulation in Health and Disease*. Lea & Febiger, 1915.
- [141] J. Womerlsey. Method for the calculation of velocity, rate of flow and viscous drag in arteries when the pressure gradient is known. *The journal of physiology*, pages 553–563, 1955.
- [142] P. K. Yadav, B. D. Sharma, and A. N. Filippov. Oscillatory viscoelastic model of blood flow in stenotic artery. *Colloid J.*, 82(5):617–625, Sept. 2020.
- [143] S. Yadgir et al. Global, regional, and national burden of calcific aortic valve and degenerative mitral valve diseases, 1990–2017. *Clinical*, 141:1670–1680, 2020.

- [144] B. Zhang, J. Gu, M. Qian, and et al. Study of correlation between wall shear stress and elasticity in atherosclerotic carotid arteries. *BioMed Eng OnLine*, 17, 01 2018. doi: <https://doi.org/10.1186/s12938-017-0431-y>.
- [145] P. Zhang, X. Liu, A. Sun, Y. Fan, and X. Deng. Hemodynamic insight into overlapping bare-metal stents strategy in the treatment of aortic aneurysm. *Journal of biomechanics*, 48, 04 2015. doi: 10.1016/j.jbiomech.2015.03.028.
- [146] A. Zingaro, M. Bucelli, I. Fumagalli, L. Dede, and A. Quarteroni. Modeling isovolumetric phases in cardiac flows by an augmented resistive immersed implicit surface method. 08 2022.
- [147] S. Zonca, C. Vergara, and L. Formaggia. An unfitted formulation for the interaction of an incompressible fluid with a thick structure via an XFEM/DG approach. *SIAM Journal on Scientific Computing*, 40:B59–B84, 01 2018. doi: 10.1137/16M1097602.
- [148] I. Zygote Media Group. Zygote solid 3d heart generation II development report. tech. rep. 2014.
- [149] D. Šedivý and S. Fialová. Computational fluid dynamics simulation and comparison of flow through mechanical heart valve using Newtonian and non-Newtonian fluid. *International Journal of Biomedical and Biological Engineering*, 11(9):1534 – 1539, 2017. ISSN eISSN: 1307-6892.

A | Appendix A

A.1. Sensitivity to parameters of the healthy configuration

This Appendix has the purpose of showing the sensitivity of the healthy configuration to different parameters.

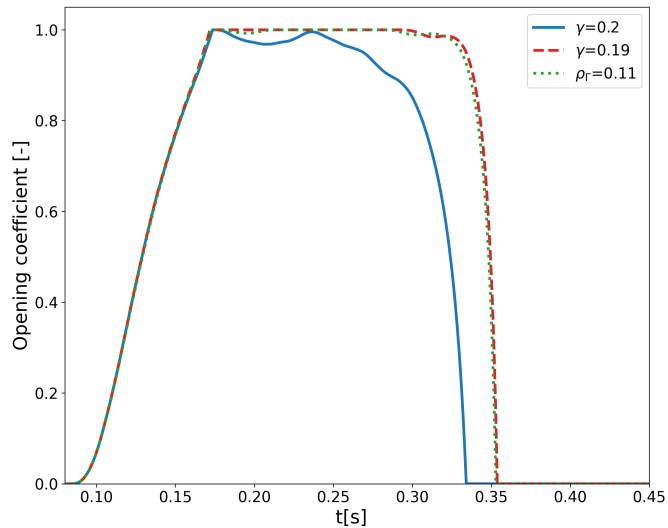


Figure A.1: Comparison between the opening coefficient of the healthy configuration (obtained using the parameters of Table 4.3) and the ones imposing the same exact parameters except for $\gamma = 0.19 \text{ N/m}$ in one case, and $\rho_\Gamma = 0.11$ in the other case.

As we can see from Figure A.1, starting from the healthy configuration of Section 4.2 and changing by only 5 % the elasticity coefficient γ and 10 % the scaling factor for density ρ_Γ in the 0D valve model, we obtained a completely different behavior of the opening coefficient in both cases, which leads to a different behavior of the whole simulation. Indeed, for both cases, we obtained the general behavior of a regurgitant valve: the closure is delayed with respect to the healthy case and this causes regurgitation during the closing phase (see Section 4.3). This was the case even when switching to the non-Newtonian rheology.

List of Figures

1.1	Structure of the heart and direction of blood flow through the heart chambers and heart valves; image taken from [65] Figure 9-1	2
1.2	Cardiac cycle for left ventricular function, showing changes in left atrial pressure, left ventricular pressure, aortic pressure, ventricular volume, the electrocardiogram, and phonocardiogram; image taken from [65] Figure 9-6	3
1.3	Aortic root	5
1.4	Open and closed configuration of healthy and stenotic valve; image taken from [108].	7
1.5	Composition of blood; image taken from [3].	8
1.6	Visualization of aggregation. The left column corresponds to low shear rates, the center column to moderate share rates, and the right column to high shear rates; image taken from [50].	9
2.1	Relation between shear rate and dynamic viscosity according to Carreau model, given by Equation (2.10).	21
2.2	Schematic representation of d_F and different configurations of the section of the leaflet; image taken from [56] Figure 1.	26
3.1	Pressure and viscosity distribution in the domain for the steady case.	34
3.2	Velocity profiles for the steady case in a cylinder domain.	35
3.3	Velocity profiles corresponding to the maximum flow rate for the pulsatile case in a cylinder domain.	37
3.4	Velocity profiles corresponding to the minimum flow rate for the pulsatile case in a cylinder domain.	37
3.5	Comparison between the Newtonian and the non-Newtonian viscosity at the maximum flow rate.	38
3.6	Comparison between the Newtonian and the non-Newtonian viscosity at the minimum flow rate.	39
4.1	Aortic root domain with flow extension and closed valve leaflets.	42
4.2	Closed (a) and open (b) configuration of the valve.	43

4.3	3D tetrahedral mesh of the aortic root with zoom on the area close to the aortic valve.	44
4.4	Control volumes location with respect to the leaflets.	45
4.5	Physiological pressure boundary conditions.	46
4.6	Dynamics of the valve in healthy configuration	48
4.7	Pressure difference computed between the two control volumes (left) and flow rate through the valve (right).	49
4.8	Velocity (a) and pressure (b) distribution at four different time steps: before the opening (0.085 s), during the valve opening phase (0.13 s), when the valve is completely open (0.20 s) and during the closing phase (0.30 s).	50
4.9	Pressure within the leaflets (a) and leaflets velocity \mathbf{u}_Γ (b) at four different time steps: before the opening (0.085 s), during the valve opening phase (0.13 s), when the valve is completely open (0.20 s) and during the closing phase (0.30 s).	51
4.10	Q-criterion isosurfaces with $Q = 1000 \text{ s}^{-2}$ colored with velocity magnitude at four different time steps: during the valve opening phase (0.13 s), when the valve is completely open (0.20 s), during the slow part of the closing phase (0.28 s) and during the faster part of the closing phase (0.33 s).	52
4.11	Velocity distribution (a) and Q-criterion isosurfaces with $Q = 1000 \text{ s}^{-2}$ colored with velocity magnitude (b) at $t=0.42 \text{ s}$	53
4.12	Valve dynamic healthy, regurgitant and stenotic	55
4.13	Comparison between pressure difference computed between the two control volumes in the healthy and stenotic cases.	56
4.14	Comparison between pressure difference computed between the two control volumes in the three pathological cases.	57
4.15	Comparison between flow rate through the valve in the three pathological cases.	58
4.16	Comparison at the time of regurgitation between healthy (top) and regurgitant (bottom) valves. On the left the velocity distribution and on the right Q-criterion isosurfaces with $Q = 1000 \text{ s}^{-2}$ for the two cases respectively at $t=0.33 \text{ s}$ and $t=0.34 \text{ s}$	59
4.17	Velocity distribution in healthy (a) and stenotic (b) cases for three different time steps: during the valve opening phase (0.13 s), at maximum valve opening (0.20 s) and during the closing phase (0.30 s).	60

4.18 Q-criterion isosurfaces with $Q = 1000 \text{ s}^{-2}$ for healthy (a) and stenotic (b) configurations colored with velocity magnitude at three different time steps: during the opening phase (0.085 s), when the valve is completely open (0.20 s) and during the slow part of the closing phase (0.28 s).	61
4.19 Valve dynamic Newtonian vs non-Newtonian comparison	63
4.20 Pressure jump and flow rate through the valve Newtonian vs non-Newtonian comparison	64
4.21 Comparison with Newtonian (left) and non-Newtonian (right) magnitude of the wall shear stress on the aortic root for regurgitant configuration on four different time steps: before the opening (0.085 s), during the valve opening phase (0.13 s), when the valve is completely open (0.24 s) and during the closing phase (0.34 s).	66
4.22 Comparison with Newtonian (left) and non-Newtonian (right) magnitude of the wall shear stress for stenotic configuration on four different time steps: before the opening (0.0085 s), during valve opening phase (0.12 s), when the valve is completely open (0.20 s) and during the closing phase (0.29 s).	67
4.23 Time-Averaged Wall Shear Stress comparison between Newtonian (left) and non-Newtonian (right) model in regurgitant and stenotic configurations.	68
4.24 Percentage difference between Time-Averaged Wall Shear Stress (see Equation (4.4)) in regurgitant (left) and stenotic (right) cases.	69
4.25 Comparison with Newtonian (left) and non-Newtonian (right) magnitude of the wall shear stress on the aortic valve for regurgitant configuration on four different time steps: during the first stage of the valve opening (0.1 s), in the middle of the opening phase (0.13 s), when the valve is completely open (0.24 s) and during the closing phase (0.34 s).	70
4.26 Comparison with Newtonian (left) and non-Newtonian (right) magnitude of the wall shear stress on the aortic valve for stenotic configurations on four different time steps: during the first stage of the valve opening (0.1 s), in the middle of the opening phase (0.13 s), when the valve is completely open (0.20 s) and closing phase (0.29 s).	71
A.1 Comparison between the opening coefficient of the healthy configuration (obtained using the parameters of Table 4.3) and the ones imposing the same exact parameters except for $\gamma = 0.19 \text{ N/m}$ in one case, and $\rho_\Gamma = 0.11$ in the other case.	93

List of Tables

2.1	Carreau's model parameters.	21
3.1	Comparison with the reference results [128] for $R = 0.0031\text{ m}$.	36
3.2	Comparison with the reference results [128] for $R = 0.0045\text{ m}$.	36
3.3	Comparison of the max flow rate with the reference results [128] for $R = 0.0031\text{ m}$.	38
3.4	Comparison of the max flow rate with the reference results [128] for $R = 0.0045\text{ m}$.	38
4.1	Mesh size and number of degrees of freedom.	45
4.2	Baseline parameters for the aortic valve simulations.	47
4.3	Parameters for the healthy configuration.	48

List of Symbols

Variable	Description	SI unit
\mathbf{u}	fluid velocity	m/s
p	fluid pressure	Pa
σ	stress tensor	N/m ²
\mathbf{I}	identity tensor	-
ρ	fluid density	Kg/m ³
Ω	domain of the simulation	-
μ	dynamic viscosity	Pa · s
$\varepsilon(\mathbf{u})$	strain rate tensor	s ⁻¹
II_ε	second invariant of the strain rate tensor	s ⁻²
$\dot{\gamma}$	shear rate	s ⁻¹
μ_∞	Carreau dynamic viscosity at ∞ shear rate	Pa · s
μ_0	Carreau dynamic viscosity at 0 shear rate	Pa · s
n	Carreau exponent coefficient	-
λ	Carreau scaling factor	-
$\mu_{newtonian}$	constant dynamic viscosity Newtonian case	Pa · s
Γ	immersed surface	-
δ_Γ	Dirac distribution	-
$\mathbf{R}_{\Gamma,\varepsilon}$	II order tensor resistance	kg · m ⁻¹ · s ⁻¹
\mathbf{u}_Γ	velocity of the surface	m/s
R	scalar resistance	kg · m ⁻¹ · s ⁻¹
$\hat{\Gamma}$	reference configuration of the immersed surface	-
Γ_t	immersed surface at time t	-
φ_t	signed distance function at time t	-

Variable	Description	SI unit
$\delta_{t,\varepsilon}$	a smooth Dirac function to approximate δ_{Γ_t}	-
ε	half-thickness of the immersed surface	m
\mathbf{d}_Γ	displacement of the leaflet	m
\mathbf{n}_Γ	normal to the surface Γ	m
$H(\mathbf{x})$	leaflet curvature w.r.t. reference configuration	m^{-1}
ρ_Γ	surface density	Kg/m^3
β	damping coefficient	s^{-1}
γ	elasticity coefficient	s^{-2}
$\hat{H}(\hat{\mathbf{x}})$	total leaflet curvature in $\hat{\mathbf{x}}$	m^{-1}
$\mathbf{g}(\hat{\mathbf{x}})$	spatial dependence on displacement	m
$c(t)$	opening coefficient	-
$\tilde{\mathbf{n}}_\Gamma$	extension of \mathbf{n}_Γ on $\Omega \setminus \Gamma$	m
$\tilde{H}(\mathbf{x})$	extension of $H(\mathbf{x})$ on Ω	m^{-1}
$\tilde{\mathbf{g}}(\mathbf{x})$	closest-point extension of $\mathbf{g}(\hat{\mathbf{x}})$ on Ω	m
\hat{H}	pulled-back curvature	m^{-1}
R	radius of the cylinder	m
WSS	wall shear stress	Pa
f	frequency of the pulsation	Hz
OA	orifice area	m^2
h	mesh size	m
t_0	initial time of the simulation	s
T	final time of the simulation	s
Δt	time step	s
Q	value for the isosurfaces in Q-criterion	s^{-2}
AS	aortic stenosis ratio	-
TAWSS	Time-Averaged Wall Shear Stress	Pa

Acknowledgements

I would like to express my deepest gratitude to Dr. Ivan Fumagalli and Michele Bucelli for being amazing supervisors. Thank you for being always available for support and suggestions: I will try to carry on all your precious advice for the rest of my professional life.

A sincere thanks to Prof. Luca Dedè for his time and effort supervising this thesis: your knowledge and love for mathematics were of considerable inspiration to me.

Dedicated gratitude goes to my friend and project partner Michele: your help and support were fundamental for the first part of this work, and you helped me to grow as a person.

I could not have undertaken this journey without all my friends from Domodossola: hanging out with all of you was always delightful, you have definitively helped me to distract my mind from the stressful academic life. Thank you for all the years of faithful friendship and for the love you always have shown to me, even in times when I probably didn't deserve it. I would like to mention a lot of you, you are a very important part of my life. However, there are too many of you I would risk forgetting someone: I hope that every one of you knows how important he is to me.

Many thanks to my roommate Alessandro: thank you for the laughs, support, and fun that you donated to me throughout the three amazing years spent in Milan together.

Special thanks go to one of my dearest friends, Manfred. We shared all the moments of our academic life and we both know that without you I would never be able to arrive at this point. Thank you for all the hours that you dedicated to listening to my problems and to be such an amazing friend. I sincerely consider our friendship one of the greatest gifts that the university gave to me.

Thanks from the bottom of my heart to my best friend Filippo. We have lived every moment of our life together, in addition to being roommates for five years. You were always there for me when I really needed it. Even the distance is not able to change our incredible friendship, and, we both know, that this will be the case for the rest of our life. I expressed my gratitude to you in many letters, but I know I will not be able to match

the commotion that you gave to me with your own Acknowledgment: you won this round.

Finally, I would like to thank my family. Particular thanks go to my cousin Andrea for being the best possible person with whom I share my childhood. I can definitively say that you look more like a brother than a cousin to me. An infinite "thank you" goes to Nonna Uetta, whenever you are now (and sorry for the English, you would be very disappointed by me), and to Nonno Tio: you raised me and I would definitely not be the same person without your guidance. To my sister and "More": you are, and you will always be the person that I would like to protect the most in the whole world. I hope I could be for you half of the inspiration that you are to me: you are a really strong person, even if maybe you often don't realize it. I'm really proud to be your brother, and remember that your only limit is the sky. Mamma and Papà, I owe you everything. You supported and believed in me throughout my whole life. Papà, even if probably often I'm not fully able to show you this, I love you so much. Your way of living your life is amazing and of great inspiration to me: I hope that one day I will be able to be similar to the man that you are. And, finally, Mami, you are the only person in the world capable of fully understanding me. You are the person to which I would like to express my deepest gratitude, but the only one for whom I cannot really find the right words. I can only tell you that I don't know what I could do without you.

Thank you.

Ringraziamenti

Vorrei esprimere estrema gratitudine a Ivan Fumagalli e Michele Bucelli per essere stati dei fantastici supervisori. Vi ringrazio per essere sempre stati disponibili per aiuti e suggerimenti: cercherò di fare tesoro di tutti i vostri preziosi consigli per il resto della mia carriera professionale.

Un ringraziamento sincero al Professor Luca Dedè per il suo tempo e gli sforzi dedicati a supervisionare questa tesi: la sua conoscenza e amore per la matematica sono state di grande ispirazione per me.

Una dedica va al mio amico e compagno di (vari) progetti Michele: il tuo aiuto è stato di fondamentale importanza per la prima parte di questo lavoro e mi hai aiutato a crescere come persona.

Non avrei potuto affrontare questo viaggio senza tutti i miei amici di Domodossola: passare il tempo con voi è sempre stato fantastico e mi avete aiutato molto a distrarmi dalla stressante vita accademica. Grazie per tutti questi anni di amicizia fedele e per tutto l'affetto che mi avete mostrato anche in momenti in cui probabilmente non me lo meritavo. Vorrei menzionare molti di voi, siete una parte fondamentale della mia vita, ma siete veramente tanti e temo rischierei di dimenticare qualcuno: spero che ognuno di voi sappia con precisione quanto è importante per me.

Non posso non ringraziare il mio coinquilino Alessandro: grazie per tutte le risate, il supporto e il divertimento che mi hai donato nei tre stupendi anni che abbiamo passato a Milano insieme.

Un ringraziamento speciale va a uno dei miei amici più cari, Manfred. Abbiamo condiviso ogni momento della nostra carriera accademica e sappiamo entrambi che senza di te non ce l'avrei mai fatta ad arrivare a questo punto. Grazie per tutte le ore che hai dedicato all'ascoltare i miei problemi e per essere un amico stupefacente. Ritengo seriamente che la nostra amicizia sia uno dei regali più grossi che l'università mi abbia fatto.

Grazie dal profondo del cuore al mio migliore amico Filippo. Oltre ad essere stati coinvilini per ben 5 anni, abbiamo vissuto ogni momento della nostra vita insieme. Sei

sempre stato presente per me quando ne avevo veramente bisogno. Neanche la distanza è stata in grado di cambiare la nostra incredibile amicizia e, sappiamo entrambi, che questo non cambierà per tutto il resto della nostra vita. Ti ho espresso la mia gratitudine in molte lettere, ma so che in questo caso non sarò in grado di eguagliare la commozione che mi hai generato con i tuoi Ringraziamenti: hai vinto questo round.

Infine vorrei ringraziare la mia famiglia. Grazie a mio cugino Andrea per essere stato la miglior persona possibile con cui condividere la mia infanzia. Posso dire senza remore che ti considero più un fratello che un cugino. Un infinito "grazie" va alla mia Nonna Uetta, ovunque tu sia ora (e scusa per l'inglese, saresti molto delusa da me) e a mio Nonno Tio: mi avete cresciuto e senza la vostra guida non sarei sicuramente diventato la persona che sono. A mia sorella e "More": sei e sarai sempre la persona che vorrei proteggere di più in tutto il mondo. Spero che io possa essere un'ispirazione per te anche solo la metà di quanto lo sei tu per me: sei veramente una persona forte, anche se spesso non te ne rendi conto. Sono veramente orgoglioso di essere tuo fratello, e ricordati che il tuo solo limite è il cielo. Mamma e Papà, vi devo tutto. Mi avete supportato e avete creduto in me durante tutta la mia vita. Papà, anche se forse spesso non te lo mostro come dovrei, ti voglio tanto bene. Il tuo modo di vivere la vita è fantastico e di grande ispirazione per me: spero che un giorno riuscirò ad essere un uomo simile a quello che tu sei. E, infine, Mami, sei l'unica persona al mondo capace di capirmi fino in fondo. Sei la persona alla quale vorrei esprimere la più grossa gratitudine ma l'unica per la quale non riesco a trovare le giuste parole. Posso solo dirti che non so cosa farei senza di te.

Grazie davvero a tutti.

*Luca Caivano
Milano, 6 Ottobre 2022*